MASS MEASUREMENT OF PROTON HALO CANDIDATE ALUMINUM-22 AND RECENT UPGRADES TO THE PHASE IMAGING ION CYCLOTRON RESONANCE TECHNIQUE

By

Scott E. Campbell

A DISSERTATION

Submitted to
Michigan State University
in partial fulfillment of the requirements
for the degree of

Physics—Doctor of Philosophy

2026

ABSTRACT

Nuclear masses are fundamentally important to understanding the various interactions occurring within the atomic nucleus. In particular, it is known that the mass of an atomic nucleus is lighter than the sums of all constituent proton and neutron masses: some of the mass is converted into a 'binding energy' acting to hold the nucleus together. The extent of this binding energy for a given nucleus can only be revealed through high precision mass measurements. Precise mass information of rare nuclei—who decay after mere fractions of a second—are particularly valuable as they serve as sensitive probes for nuclear theory and inform predictive models of nuclear properties.

Near the limits of nuclear existence, where one fewer/additional neutron makes the nucleus proton-/neutron-unbound respectively, radioactive nuclei can exhibit various exotic features. For example, the normally exceptionally small and dense nucleus can have a nucleon which extends far beyond its typical radius. These so-called 'halo structures' provide stringent tests of nuclear structure models, yet experimental information remains sparse as these nuclei are quite rare and often very challenging to produce. Precise knowledge of the binding energy (and consequently mass) is paramount to understanding the role of weak binding in the emergence of the halo structure.

Penning trap mass spectrometry (PTMS) remains the most precise technique to determine nuclear masses, and can access radioactive nuclei with half-lives down to tens of milliseconds. State-of-the-art radioactive beam facilities, such as the Facility for Rare Isotope Beams (FRIB), have made tremendous progress expanding the reach for experiments with the most exotic radioactive nuclei. However, many of the isotopes of highest scientific impact may still only be produced at rates of a few ions per day, making precise measurements challenging if not infeasible. Measurement techniques with higher sensitivity remain critical to access the much-needed masses of these isotopes.

The Low Energy Beam Ion Trap (LEBIT) facility at FRIB has utilized PTMS for the last 18+ years to measure the masses of many rare and exotic isotopes. The work details the experimental facilities as well as developments to the recently implemented phase imaging ion cyclotron resonance (PI-ICR) Penning trap mass measurement technique. Demonstrations of PI-ICR's capa-

bilities show a significant improvement in the achievable mass precision with fewer detected ions than the traditional PTMS technique. Detailed studies of the systematic uncertainties inherent to PI-ICR are also discussed. Lastly, a precise mass measurement of aluminum-22 is presented, which was suggested to exhibit a proton halo structure from recent experimental measurements of nearby nuclei. Predictions from theory constrain and challenge the existence of a proton halo structure, despite the exceptionally small binding of the valence proton determined from the newly measured mass.

Dedicated to the memory of my Gogo and Papa, whose exceptional contributions to science and education were equally matched by their reverence to life—for music, for family, and for the endless curiosity that makes the world special.

ACKNOWLEDGEMENTS

I've had the pleasure of working alongside an incredible group of graduate students during my time at LEBIT. Special thanks are owed to Issac Yandow whose infectious kindness and optimism motivated me to join the group in the first place. I deeply admire both Christian Ireland and Hannah Erington for their incredible persistence, playful banter, and work ethic which continues to inspire me. The experimentalist I've become is in no small way attributed to their support commiserating through the lows and rejoicing in the highs during the many late nights and seemingly endless curveballs thrown our way. I also appreciate the career advice and continued support from Franziska Maier during the last few years.

I hold my deepest appreciation for my advisor Ryan Ringle, especially his willingness to provide a continual supply of artisanal coffee. I am grateful for the many uniquely challenging and rewarding projects over the course of my studies, and for the many discussions when a wrench was inevitably thrown into our plans. I especially appreciate all the heartfelt advice and guidance while I navigated the different stages of my PhD. Similarly, I am very grateful to my committee: Kei Minamisono, Scott Pratt, Reinhard Schwienhorst, and Hui-Chia Yu. Their encouragement and extensive knowledge was invaluable over the course of this program.

The entire team of scientists and staff at FRIB are truly inspiring. The willingness and openness of everyone to pitch in and make every experiment possible was instrumental to the many successful measurements we were able to make. In particular, I'd like to thank the gas stopping group for their continual assistance and expertise especially during the experimental run for my thesis data. I was also incredibly fortunate to collaborate with both Alex Brown and Kevin Fossez whose theoretical expertise was essential to the results.

This work would not have been possible without the Department of Energy National Nuclear Security Administration and the Stewardship Science Graduate Fellowship (DOE NNSA SSGF) and their generous support of both me and the research I have been fortunate to participate in. The practicum at Lawrence Livermore National Laboratory supported by the fellowship program was incredibly insightful. Special thanks are due to the BEARTrap collaboration who I was fortunate

to join during the experience. I'd also like to extend thanks to the superheavy elements group at the GSI Helmholtzzentrum and the Deutscher Akademischer Austauschdienst RISE Professional Internship program. My time studying and exploring in Germany was especially fruitful to this work. My time there was only made better by the many friends and colleagues who welcomed me so warmly.

To my friends: the generous and kind presence you have brought to my life has meant more to me than you can know. You remind me to step back and appreciate the world and the beautiful things within. I could never have expected the incredible generosity and selflessness that each of you have extended towards me. You inspire, motivate, and challenge me in immeasurable ways and I am a better person for it.

I can hardly express how important my family has been to me during my studies. Each and every one of you continuously inspires me with your incredible love, support, and all our amazingly unique talents. You sparked my first love for science and nurtured my (often chaotic) experimentation at every turn. To Susan, Mary, and Kyle: you have always been my closest confidants and it means the world that I can always turn to you for a sympathetic ear. To my mom and dad: your endless encouragement coupled with an adventurous spirit has seen us through so many wonderful experiences forming the foundations of who I am. I love you all from the bottom of my heart, and can't wait to see what our next adventures hold.

PREFACE

During the last year of my PhD, I have spent a significant amount of time reflecting on my research. Perhaps one of the most challenging aspects has been stepping back and contemplating how the broader public perceives and engages with such niche science. As someone funded by government grants, I feel it's necessary to open that discussion and share the importance of fundamental science even when the results often feel intangible. It is my sincere hope that both the depth of this work and the care with which it has been carried out reflect my commitment to upholding the public trust.

I wrote the following essay over the course of my studies and while processing what that science has meant to me. The original drive to start this project was never really clear, though maybe now I hope you can find a quiet connection with one of the people carrying out science.

Working in Circles

Stillness has never been in my nature. From custom book binding to technical scuba diving, the ebb and flow of my focus across time is powered by a deep desire to understand how something works. Immersing myself into a new obsession is thrilling, but also bittersweet once my narrowed focus leaves other interests on the back-burner. Though, thinking back to the many complex problems I've tackled—like troubleshooting a faulty scuba tank 150 feet below Lake Michigan—I'm constantly returning to the skills I've built across my many hobbies. Once I saw that this blend of intellectual curiosity and critical thinking thrived in science, I was instantly hooked. Trusting my instinct to explore broadly has guided me through my first nervous steps in nuclear physics through the scientist I've now become.

I'm delighted when connections appear across interests, especially so in science where they tend to surface in unanticipated ways. This is certainly the case in experimental physics, where finding creative solutions often means rolling up your sleeves and getting your hands a bit dirty—and I love that. It takes an incredibly diverse set of skills and people to make even the simplest experiments possible. I take part in everything from designing the electrodes and electronics which precisely

guide ions towards a detector, down to the software that records and analyzes the results. I'm consistently amazed when I step back and can see my fingerprints on every part of the nuclear mass measurements I perform.

Just as gratifying is seeing the broader impact of something I took part in. In the case of atomic nuclei, precisely determining their masses provides invaluable insight into the forces responsible for their existence in the first place. Questioning why a nucleus exists hadn't really crossed my mind before, and I was quite amazed once I started looking a bit closer. The nucleus is a pretty surprising entity: except for hydrogen, every element has several protons and neutrons packed extremely close to one another. And much like two magnets try to repel each other when brought too close, each proton is actively working to push away all the others. So why doesn't everything just instantly fly apart?

Astonishingly, the nucleus overcomes this repulsion by converting some of its mass into energy that binds itself together. This is a perfect example of Einstein's most famous equation $E = mc^2$. When we measure the mass of an atom, we see this relationship in action: the mass of the nucleus is less than the sum of all protons and neutrons. The difference turns out to be a unique fingerprint for each atom, and encodes just how strongly it will resist decaying to a more stable form among other features defined by its configuration. With this knowledge, the seemingly humble mass informs theoretical models across a vast scale: from the structure of matter up to the processes actively creating the elements inside stars.

Adequately probing the forces responsible for keeping the nucleus bound requires mass precisions better than one part in ten million—that's equivalent to weighing a quarter relative to a 737 jet! To study these masses in the laboratory, we suspend atomic ions in space through a precisely-tuned electric field within a powerful magnetic field around 2000 times stronger than your average fridge magnet. While trapped, each ion traces a circular path where its mass reveals itself through a characteristic rotation speed. With slow and careful measurements we gradually focus into this unique frequency to better than part-per-billion resolution in some cases.

Many of the nuclei critical to furthering science are so rare that only a few may be produced

per day, even at world-class facilities. Atoms must be accelerated extremely fast and smashed into a target, where one might happen to break apart as an interesting new nucleus. When only a handful of particles are available to study, every measurement becomes a valuable part of the collective record. It takes a village—almost literally—from operating the accelerator, separating the few particles from quintillions of others (imagine differentiating one grain from all the sand on Earth!), and finally preparing them for experiments. The ultimate measurement reflects the many specialized hands at work as much as the nucleus itself.

Participating in collaborative science has changed me in quiet ways too. For someone never quite comfortable with stillness, committing to one path often felt like I was leaving behind parts of myself I wasn't yet ready to let go. Working with these fleeting particles has shifted my mindset, leading me to embrace all the wonderfully unconventional parts of myself and the unexpected ways they've complemented me as a scientist. The way I view my research today is as much an exploration of myself as the tiny particles I study: a continuous exchange of energies between curiosity and reflection.

The use of generative artificial intelligence (GenAI) in this document followed the guidelines developed by the European Commission for use in research [1]. GenAI was not used in the interpretation, analysis, or writing of any results.

TABLE OF CONTENTS

LIST OF FIGURES

CHAPTER 1

INTRODUCTION

The atomic nucleus is a rather surprising entity, where a large number of positively charged protons are held together in incredibly close proximity. Classical understandings of electromagnetic forces would prohibit anything beyond hydrogen from existing as the protons would immediately be forced apart by Coulomb repulsion. We now understand that there are additional fundamental forces of nature which also act upon the protons and neutrons in a nucleus forming a 'stable' structure.

The strong nuclear force provides an exceptionally strong attraction between the nucleons at short ranges, overcoming the Coulomb potential at ranges $\sim 0.8 \times 10^{-15}$ meters (about the radius of a proton), but dwindling around 2.5×10^{-15} meters. The weak nuclear force governs the interaction between subatomic particles and is responsible for the majority of radioactive decay processes in nuclei. Certain combinations of protons and neutrons are very stable against decay and constitute all the elements we observe on Earth. As the imbalance of protons and neutrons grow, the nuclei are more prone to decay and are considered 'unstable'. Studies of these unstable nuclei, especially at and near the limits of stability, provide invaluable insights into the interplays of the nuclear forces.

This chapter introduces key concepts in our current understanding of the nuclear forces through nuclear structure models, followed by experimental mass measurement techniques which can directly probe the strong force.

1.1 Foundations of Nuclear Structure

A brief introduction to theoretical and experimental concepts underpinning nuclear structure is provided to contextualize complicated discussions later in this work. For a comprehensive review, the reader is directed to [2, 3].

The nucleus is a fascinating and deeply complex quantum system which is governed by several fundamental forces and restrictions:

- The strong interaction acts to bind the protons and neutrons together over very short distances
- The electromagnetic force acts repulsively between all protons

- The weak force governs decay processes in the nucleus (e.g. beta decay)
- The Pauli exclusion principle dictates key quantum properties for each nucleon

Despite the fact that most nuclear systems are composed of a relatively small number of constituents, there exists no exact analytical solution for understanding the nuclear structure of even the simplest systems. As such, nuclear structure requires the use of phenomenological models and approximations to describe these fundamentally important systems. Thankfully, there are a number of key observables and experimental probes which are used to characterize and infer nuclear structure, including:

- Nuclear masses and binding energies
- Nuclear radii and density distributions
- Electromagnetic moments and transition rates
- Excitation spectra

Each of these observables provide valuable insight into the role of nuclear structure across a range of nuclear systems.

Of particular relevance to the work presented in this document is the nuclear mass. Figure 1.1 illustrates how the nuclear mass (via the nuclear binding energy) can highlight important nuclear structure features, and was one of the earliest indicators of a nuclear shell-structure. Nuclear binding energy is defined as

$$B\left({}^{A}_{Z}X_{N}\right) = \left[Z \cdot m_p + N \cdot m_n - m\left({}^{A}_{Z}X_{N}\right)\right] c^2 \tag{1.1}$$

where the notation ${}^{A}_{Z}X_{N}$ defines the isotope with mass number A equal to Z protons plus N neutrons; m_p, m_n are the proton and neutron masses. As shown in the plot, certain numbers of protons/neutrons have abnormally strong binding energy, and additional experiments have found that nuclei with either N or Z equal to 2, 8, 20, 28, 50, 82, and $N = 126$ are particularly stable. These special numbers are referred to as *magic*, and nuclei with that number of protons/neutrons are called *magic nuclei*.

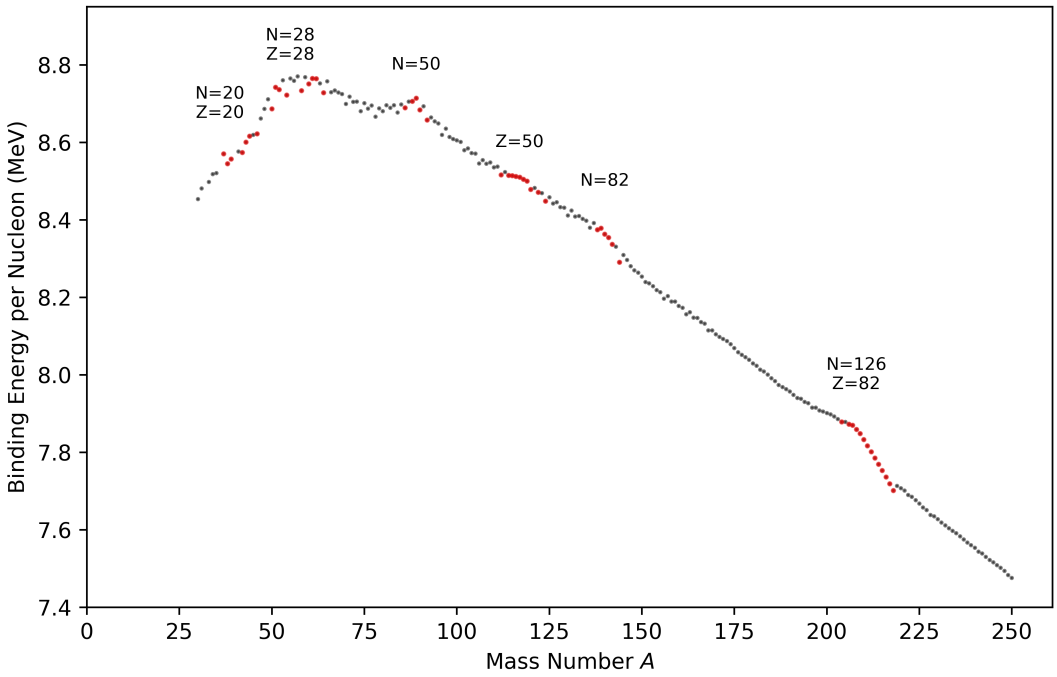

Figure 1.1 Experimental binding energies normalized by the nuclear mass number $A = Z + N$. Only odd-even nuclei (or an average of neighboring nuclei for even masses) are shown such that there is no impact from nuclear pairing. Distinct kinks towards higher binding energies at certain 'magic' numbers (shown in red) can be observed, indicating the nucleus has a shell-like structure. Adapted from [2].

A number of theoretical nuclear models have been developed to describe nuclear properties, starting with the liquid-drop model in the 1930's. A more advanced and robust description of the nucleus is through a 'shell structure' where an ordered hierarchy exists inside the nucleus where protons and neutrons are arranged in stable quantum states within their own potential wells. To gain insight into the specifics of the nuclear shell model, consider first the analogous atomic shell model: electrons bound to an atom are arranged in hierarchical energy shells. The Pauli exclusion principle determines the number of electrons which exist at the same energy based on other available unique quantum states, labeled by the principle quantum number n, orbital angular momentum ℓ, magnetic quantum number m_ℓ, and spin quantum number m_s. The shell an electron occupies have labels such as $1s$, $2s$, $2p$, etc. to note the quantum numbers n and ℓ respectively. Filled electron shells result in particularly stable atomic configurations. Electrons in the atom can be excited to higher

energy levels, and de-excite accordingly. Electrons which only partially fill a shell are referred to as 'valence electrons.'

Shifting back to the nuclear shell model, a number of similarities exist. Since protons and neutrons are distinguishable particles, they arrange into independent shell structures while satisfying the Pauli principle. Each level in a shell model is uniquely labeled by a set of quantum numbers. The choice of potential energy function determines the relevant quantum numbers and energies of each bound state. For example, an infinite well potential is fully described by a principle number n and angular momentum number ℓ. A more complex potential which accounts for the spin-orbit coupling of the nucleons requires an additional 'total angular momentum' quantum number j. Figure 1.2 provides a comparison of the levels for three different potential energy functions (increasing in realism).

Considering the experimental evidence discussed earlier, only the shell model potential with the Woods-Saxon and spin-orbit coupling form adequately replicates the observed magic shell closures of stable nuclei. Of particular interest is the fact that the choice of the nuclear potential function can cause drastic shifts in the ordering of the shell model levels. This becomes particularly relevant when predicting the properties of exotic nuclei existing far from stability. For these nuclei, a more detailed description of the nuclear potential is typically required, and the level ordering becomes sensitive even to minor adjustments. This sensitivity is further amplified by the deformed shapes (i.e. non-spherical) many exotic nuclei exhibit [4]. The success of the shell model in accurately modeling the nuclear potential relies on a continual validation of the predicted properties of these nuclei with new experimental observations. Mass measurements of unmeasured nuclei provide insight into the strength of the strong nuclear force via the binding energy, and serve as an especially useful probe of nuclear models [5, 6]. The next section discusses some of the implications for nuclear structure for some of these exotic nuclei.

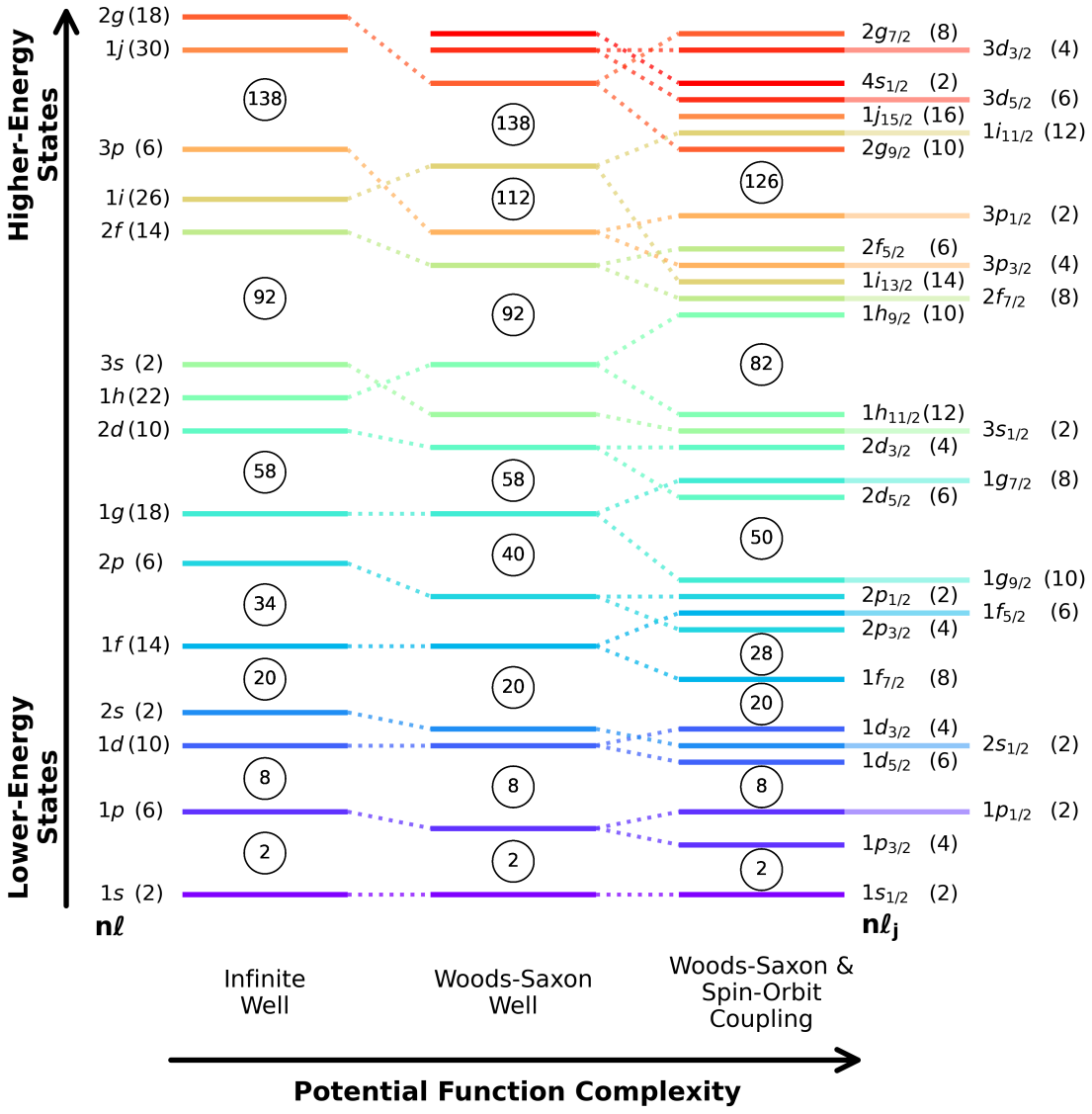

Figure 1.2 Illustration of bound single-particle states, given a spherical nucleus, for three different nuclear potential models. Each state is shown with its quantum numbers, and dashed lines (and color) show energy shifts/splitting between the models. The number of particles that can fill each shell is shown in parenthesis. Magic numbers for the last nuclear potential are shown in circles. Adapted from [2].

1.2 Exotic Nuclear Structures at the Limits of Existence

Because the nuclear strong force acts over such a short distance, there are finite limits for the combinations of protons and neutrons which form a stable nucleus. For simplicity, we often characterize the nucleus by the element (aka proton number) as that characterizes the chemical properties of the atom. Each element can also have different numbers of neutrons, which are referred to as 'isotopes' of that element. From the perspective of the strong force, too few neutrons in the nucleus will provide insufficient buffering between the protons and one (or more) of the protons are quickly ejected. On the other hand, too many neutrons also isn't stable. As the nucleus grows larger, the strong force no longer reaches the protons and the neutrons fill the loosely bound high-energy levels. Eventually, one (or more) of the weakly-bound neutrons is also quickly ejected from the nucleus.

These limits define the proton and neutron 'drip lines' [7] determined by the strong nuclear force. As one might expect, the nuclei on these drip lines can behave in exotic and unexpected ways which are often challenging to accurately predict [8–15]. These short-lived nuclei serve as are critical probes for evaluating the current understanding of nuclear science [5, 16]. Of the many interesting decay modes and exotic nuclear structures which have been observed [17, 18], the 'nuclear halo' presents as especially interesting feature, and will be discussed here in particular given the relevance to later work.

A halo structure is one of the most exotic cases of a deformed nucleus, where one or more of the nucleons exists at a much larger radius than the rest of the compact nucleus. While most nuclei are non-spherical, despite the extreme density of the nucleus [4], the extent is often rather small. These deformation effects are the result of a complex interplay between often unbalanced quantum properties, independently between the protons and neutrons. The extent of the deformation of a nucleus provides insight into the underlying nuclear forces. For example, a nucleus with a valence nucleon in the $s_{1/2}$ shells is characterized by a particularly diffuse spatial distribution of the nucleons, and is more susceptible to deformed shapes such as a halo structure.

Nuclei which exhibit an abnormally large charge/matter radius are characteristic of a halo

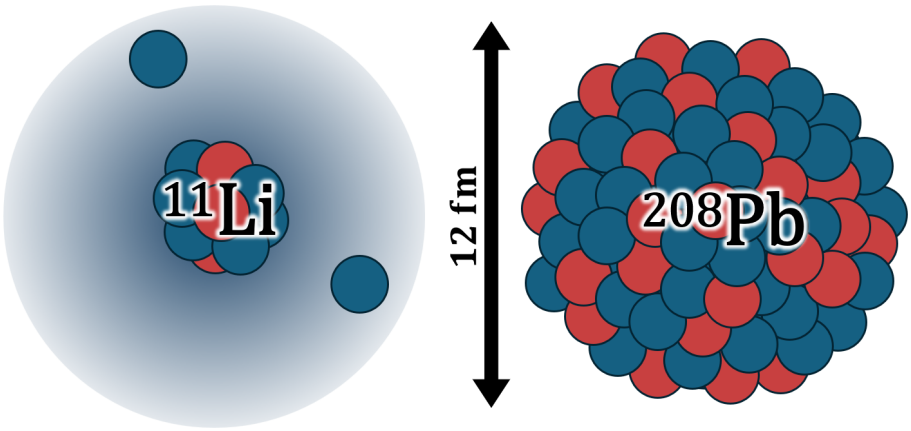

Figure 1.3 Comparison of the size of two-neutron halo nucleus lithium-11 to lead-208. Note that the halo neutrons extend to a radius comparable to that of the compact lead nucleus.

structure. This is the result of one or more valence nucleons experiencing a very weak binding to the rest of the core nucleus. The change in size of the nucleus is dramatic: Fig. 1.3 shows the radius of two-neutron halo ^{11}Li which is comparable to that for ^{208}Pb. Halo nuclei are uniquely positioned to provide critical insights into the evolution of nuclear forces at the limits of nuclear existence, see [15, 19–21] for recent reviews. Proton halos, where valence proton(s) form the halo, exist near the proton-drip line and are relatively uncommon compared to their neutron counterparts. The balance of the Coulomb force and nuclear strong force tend to prevent a proton halo from forming: if the proton is too far from the core nucleus, the Coulomb force will dominate the strong force. Proton-rich nuclei, where proton halos can exist, are also challenging to study experimentally due to low production rates at the majority of rare isotope facilities.

There are a number of unique properties which define a halo structure. As alluded to above, a significant matter radius must exist in addition to a very weak binding of the valence nucleon noted by the separation energy S_p, S_n for protons and neutrons respectively. Both of these can be observed experimentally, such as isotope shift measurements [22] to determine the charge radius (relevant for proton halos), and precision mass measurements to determine the separation energy:

$$S_p\left({}^{A}_{Z}X_N\right) = B\left({}^{A}_{Z}X_N\right) - B\left({}^{A-1}_{Z-1}X_N\right) \tag{1.2}$$

$$= \left[m\left({}^{A-1}_{Z-1}X_N\right) - m\left({}^{A}_{Z}X_N\right) + m_p\right]c^2. \tag{1.3}$$

From a theoretical standpoint, a halo structure is also characterized by valence nucleons is the $s_{1/2}$ shells [21], where the intrinsic weak binding and spatial diffuseness help to support a halo structure. Determining whether or not a given nucleus exhibits a halo structure comes down to understanding these three features. For a detailed investigation of a potential halo candidate, Chapter 6 discusses the recent experimental measurements for ^{22}Al which is thought to exhibit a proton halo.

1.3 Precise Mass Measurements for Nuclear Science

Nuclear masses are one of the most fundamental nuclear observables, and are critical to understanding nuclear shell closures, pairing effects between even-even and odd-odd/odd-even nuclei, as well as deformations and collectivity. Precise mass information across the full range of elements/isotopes remains vital to many fields of nuclear science, such as nuclear astrophysics, fundamental symmetries, and nuclear structure.

As discussed earlier, the strong force binds a nucleus together by converting some amount of the nucleons' mass into potential energy. This is a consequence of Einstein's famous mass-energy equivalence theorem [23], $E = mc^2$ which shows the interchangeability of mass and energy. The energy difference between the bound nucleus and the mass of the constituent nucleons is called the *nuclear binding energy*. Tightly bound nuclei, such as iron-56, have large binding energies. Despite knowing the masses of the protons and neutrons exceptionally well, ~0.03 ppb for the proton [24] and ~0.4 ppb for the neutron [25], the binding energy is unique to a given nucleus and can only be determined experimentally. The Atomic Mass Evaluation (AME) [26] publishes a least-squares fit to all experimental masses for known nuclei, which includes extrapolations for nuclei with no current experimental information.

Highly radioactive and exotic nuclei remain challenging to produce at rare isotope facilities, often resulting in limited experimental data for these isotopes, and no measurements for many more. For mass measurements in particular, many of the known nuclei have yet to reach the precisions needed to inform the relevant sub-fields of nuclear science, as summarized in Fig. 1.4.

Modern experimental mass measurement techniques [27] are principally limited in achievable

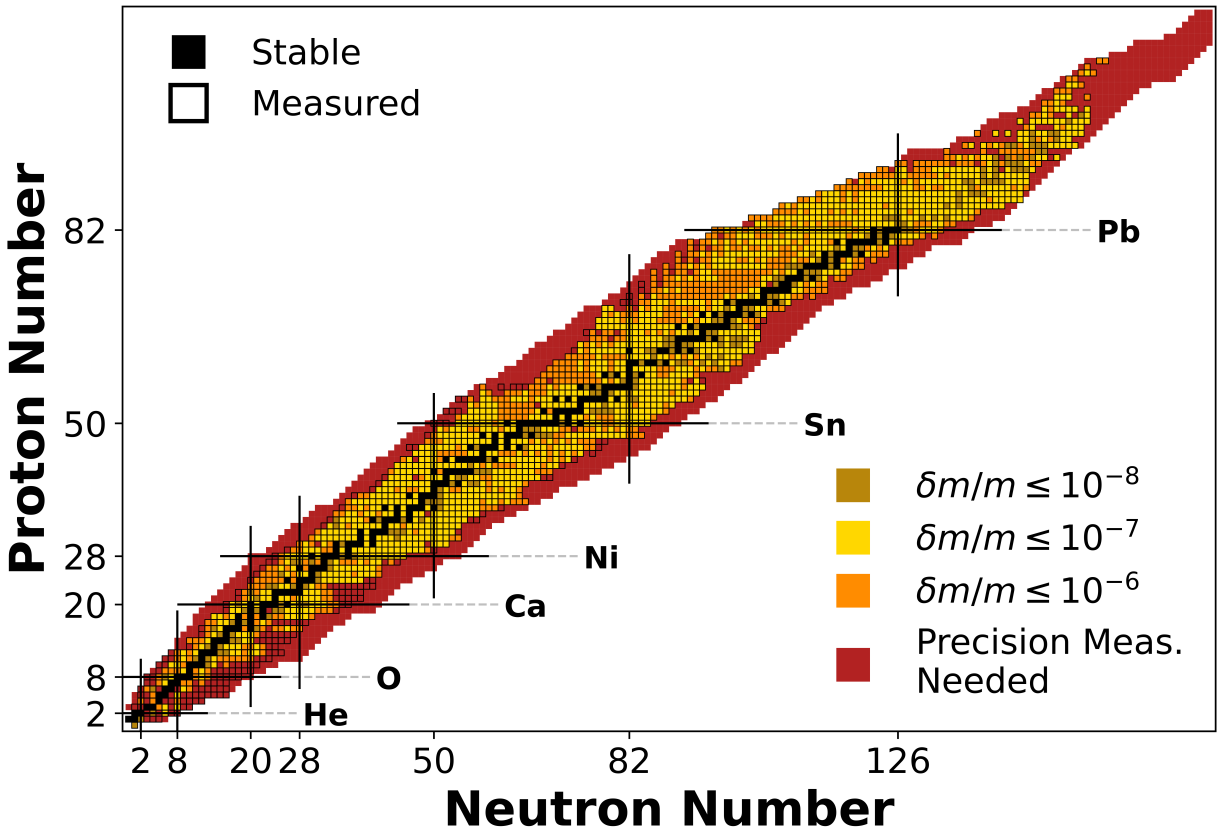

Figure 1.4 Current mass precisions as presented in the 2020 Atomic Mass Evaluation [26] for the known isotopes. Isotopes with experimental measurements have a black border, while extrapolated values do not. The current trends highlight the need for continued measurements of rare isotopes far from stability. Precisions of $\delta m/m \sim 10^{-6}$, 10^{-7}, and 10^{-8} are needed to make meaningful insights to nuclear structure, nuclear astrophysics, and fundamental symmetries studies respectively.

precision by the duration the measurement can be performed. More often than not, this is determined by the half-life of the rare isotope and the rate at which it can be produced. The mass measurement technique employed for a given isotope of interest is then chosen with this restriction in mind. A comparison of some common techniques given these restrictions is shown in Fig. 1.5.

Direct mass measurement techniques make use of time-of-flight, magnetic rigidity, as well as frequency measurements. Rare isotopes produced far from stability with very short half-lives are likely only accessible with the time-of-flight and magnetic rigidity method [29]. There are multiple facilities world-wide which utilize this technique, such as the S800 spectrograph at FRIB [30] and the SPEG at GANIL [31], which have achieved precisions of $\delta m/m \sim 10^{-6}$ in some cases. The limiting

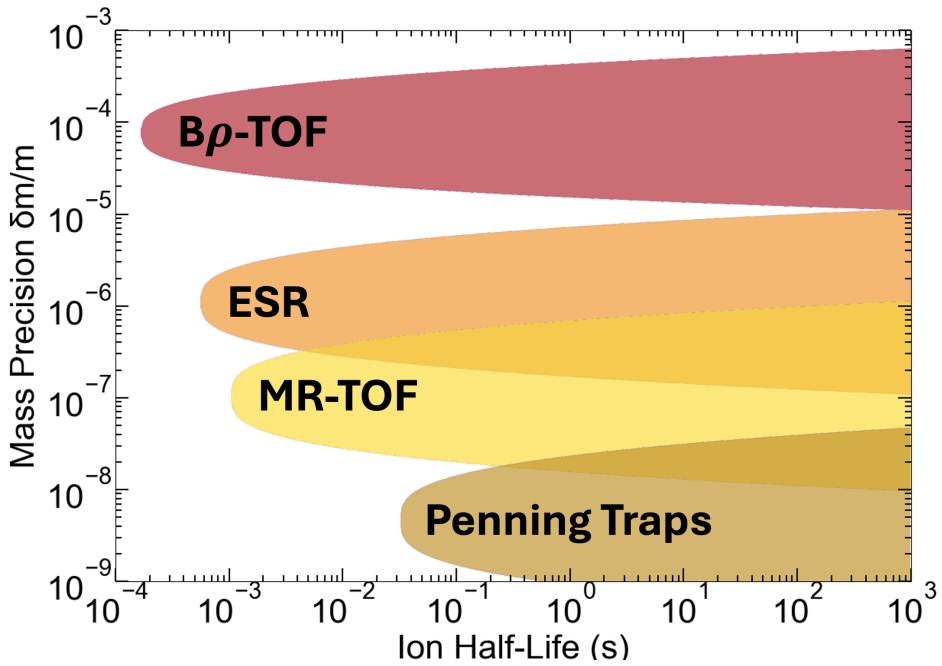

Figure 1.5 Comparison of the achievable mass precision as a function of isotope half-life for common nuclear mass measurement techniques which are available at Facility for Rare Isotope Beams (or will be shortly in the case of the MR-TOF). Nuclear structure and super-heavy element studies typically require precisions $\sim 10^{-6}$, nuclear astrophysics calculations $\sim 10^{-7}$, and tests of fundamental interactions $\sim 10^{-8}$. Of the available methods, MR-TOF and Penning traps are best-suited to provide the necessary precisions for these studies. Adapted from [28].

factor for these measurements is typically the finite distance the time-of-flight can be determined over. One approach to increasing the mass resolution through extended flight length is with experimental storage rings; ions are confined to a circular flight path and can make many revolutions. The Experimental Storage Ring (ESR) [32] at GSI and the Heavy Ion Cooler-Storage Ring at Lanzhou [33] have been successful in achieving precisions of $\delta m/m \sim 10^7$ [34]. More recent Multi-Reflection Time-of-Flight (MR-TOF) spectrometers are a compact device capable of extending the time-of-flight length by bouncing ions between electrostatic mirror pairs [35, 36]. MR-TOFs are used in many facilities as both beam purifiers [37,38], and precision mass spectrometers [36,39–41].

Of the available mass measurement techniques, Penning trap mass spectrometry (PTMS) is the most accurate and precise method [42]. Rather than time-of-flight measurements, Penning traps utilize cyclotron frequency measurements which are characteristic of a charged mass rotating in a strong magnetic field. A detailed description of Penning traps and their principles will be discussed

in Chapter 2. Penning traps have achieved exceptional mass precisions of $\delta m/m \sim 10^{-11}$ for stable ions [43, 44], and $\delta m/m < 10^{-8}$ for unstable ions are well within reach [45]. While PTMS is limited in the accessible isotope half-lives due to beam processing/preparation, very short-lived isotopes with $t_{1/2} \gtrsim 10$ ms have been successfully measured to $\delta m/m \sim 10^{-7}$ [46]. There are many rare isotope beam facilities with active PTMS programs: ISOLTRAP at CERN [47], JYFLTRAP at Jyväskylä [48], SHIPTRAP at GSI [49], CPT at Argonne National Lab [50], TITAN at TRIUMF [51], and LEBIT at FRIB [52].

The Low Energy Beam Ion Trap (LEBIT) group at the Facility for Rare Isotope Beams is uniquely situated as the only Penning trap mass spectrometry program where rare isotopes are produced by projectile fragmentation. Projectile fragmentation provides rare isotope beams of all elements and isotopes, even those with very short half-lives. Additionally, the rare isotope beam is purified in flight which provides very fast development time for new beams. As a whole, LEBIT has access to many exotic beams only available with the latest FRIB capabilities. The mass measurement program at LEBIT has been active for well over 20 years, and achieved mass precisions of 2 ppb [53], as well precise mass measurements with half-lives < 100 ms [45, 54, 55]. Chapter 3 provides further details of the experimental facilities.

1.4 Extending the Experimental Reach of Mass Spectrometry

Once operating at its full potential, FRIB will provide access to many new isotopes and dramatically increase the production rates for many of critical scienfific interest. Figure 1.6 highlights the expected nuclei which will be produced at FRIB. Despite this breakthrough advancement, many exotic nuclei far from stability will be produced at very low rates which challenge experimental capabilities. For instance, both ^{78}Ni and ^{100}Sn are of the highest scientific impact, but may only be produced and delivered to experimental areas with rates ~1 ion/hr or lower until FRIB reaches full power. Furthermore, nuclei far from stability naturally have significantly shorter half-lives which limits measurement time and consequently the achievable precision. Together, these pose difficult challenges for high precision mass measurements which often require both high statistics and long

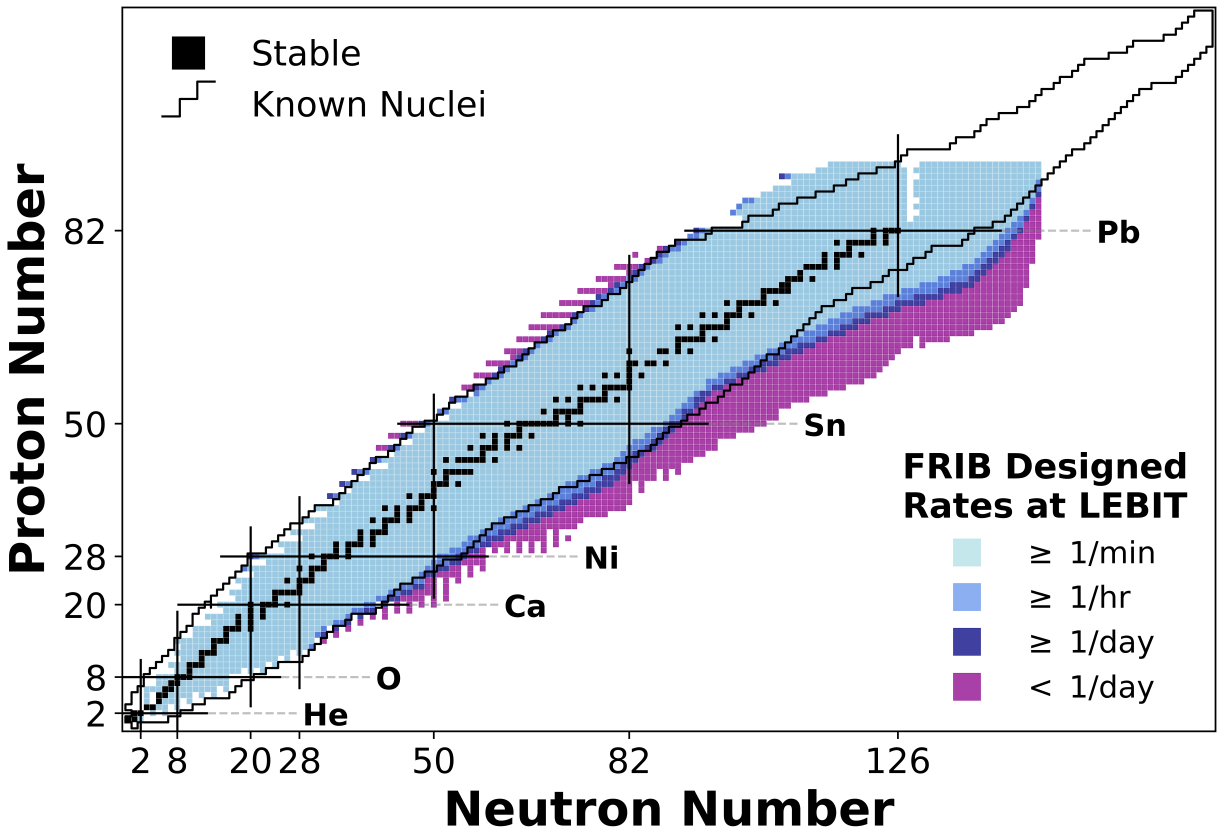

Figure 1.6 Designed FRIB rates expected to be delivered to the Low Energy Beam Ion Trap (LEBIT) mass measurement area. FRIB is expected to produce many exotic rare isotopes that have yet to be observed. However, many of these nuclei with high scientific impact may only be produced and delivered to low-energy experimental areas at extremely low rates, some on the order of 1 ion per day.

measurement times.

There have been a number of recent advances at FRIB and LEBIT which tackle both of these challenges. MR-TOF mass spectrometers are able to access high-precisions for isotopes with half-lives down to a few milliseconds, more than a order-of-magnitude improvement to other trapping methods. A high-voltage MR-TOF device is currently under development at FRIB to push further from stability, and to supply highly-purified beams for the low-energy program including LEBIT [56]. Penning traps remain the highest-precision method, and new PTMS schemes have dramatically reduced the number of ions required to complete a measurement. The Fourier transform ion cyclotron resonance (FT-ICR) technique offers a path to ultimate sensitivity [57].

LEBIT continues to develop the Single Ion Penning Trap (SIPT) project [58] which utilizes FT-ICR, and a recent analysis has validated that a mass measurement from a single one ion can be completed [59].

The introduction of the phase imaging ion cyclotron resonance (PI-ICR) [60] PTMS technique has significantly improved the achievable precisions especially for shorter-lived nuclei. LEBIT recently implemented PI-ICR [61] and commissioned with a rare-isotope measurement of ^{22}Al [45] which is detailed in Chapter 6. With a half-life $\approx$ 90 ms, PI-ICR was able to achieve a factor of four greater precision with $\approx$ 85% fewer detected ions compared to the traditional PTMS approach. PI-ICR has also been successfully used in low-rate experiments such as the measurement of ^{101}Sn where $\approx$ 1 ion was detected every five minutes [62]. Such experiments would simply not be feasible within available experimental times with the traditional PTMS techniques. Already, LEBIT is well suited to make optimal use of the new FRIB beams and provide mass measurements well beyond current limitations.

CHAPTER 2

PENNING TRAP MASS SPECTROMETRY

Penning traps remain the most precise method for measuring nuclear masses, even for radioactive nuclei with half-lives $\gtrsim$50 ms. The theoretical and experimental advances which enable these measurements remain an active field of research. This chapter provides an overview of Penning traps with a particular focus on topics relevant to their use in mass measurements. The theory and design are presented first, followed by the general mechanism which allows one to determine masses. Lastly, an overview of two specific mass measurement techniques, TOF-ICR and PI-ICR, are introduced. Both techniques are actively used at LEBIT, and provide important context for the results discussed later in this document.

2.1 Penning Trap Design and Principles

Detailed descriptions of Penning trap designs are well established, such as those in [42, 63, 64]. Key design features are noted here to provide sufficient context for considerations throughout this document. LEBIT utilizes a hyperbolic Penning trap geometry, and the following discussion applies to this case though many principles are identical across geometries.

Penning traps are designed to provide long-term 3D confinement of charged particles. The trap is aligned along a magnetic field, such that ions are confined radially (two dimensions) according to the characteristic *cyclotron frequency*:

$$\omega_c = \frac{qeB}{m'}, \tag{2.1}$$

where q is the ion charge state, e is the electron charge, m' is the ion mass, and B is the magnetic field strength. This simple relationship between mass and frequency is the foundation for this mass spectrometry technique.

However, the magnetic field alone is not sufficient to contain the charged particle in the axial dimension (along the magnetic field). To accomplish this, a quadrupolar electrostatic potential is added, where the required electrode structure is referred to as the Penning trap. A hyperbolic

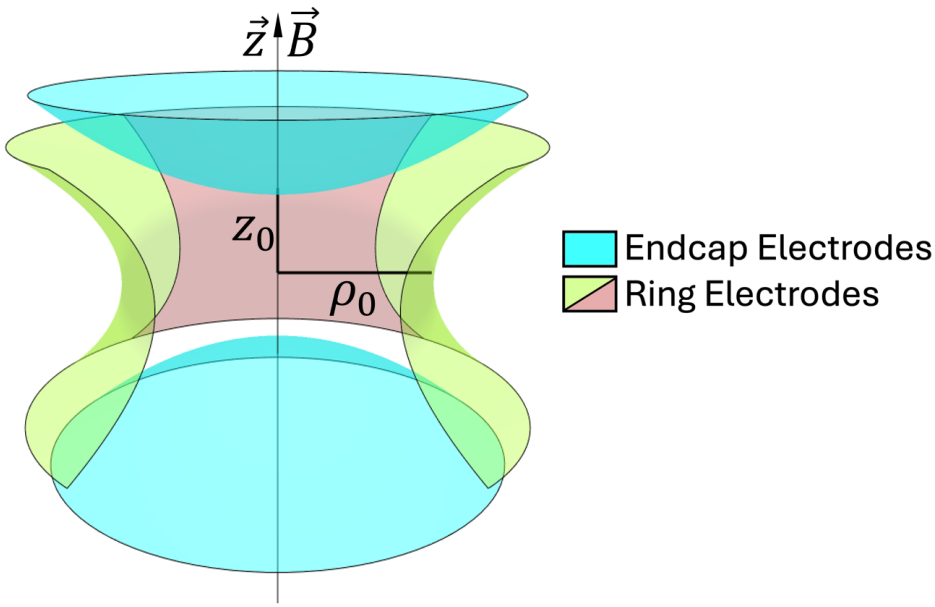

Figure 2.1 Visualization of the electrode structure for a hyperbolic Penning trap design. The trap is aligned in the axial direction, $\hat{z}$, which is parallel to the magnetic field $\vec{B}$. The characteristic axial dimension, z_0, and characteristic radial dimension, ρ_0, are also shown. The ring and endcap electrodes are held at a constant potential V_0, while the segmented ring electrodes can have an additional radio-frequency applied as well. Note the ring electrode segment closest to the reader is not displayed.

Penning trap design creates this potential through a hyperbolic ring electrode and two hyperbolic endcaps, see Fig. 2.1. The shapes of these electrodes are specified in cylindrical coordinates by

$$z^2 - \frac{r^2}{2} = \pm z_0^2, \tag{2.2}$$

where z_0 is half the distance between the two electrodes [42]. The potential field is then given by

$$V(\rho, z) = \frac{V_0}{\rho_0^2 + 2z_0^2}\left(2z^2 - \rho^2\right) \tag{2.3}$$

where V_0 is the potential difference between the ring and endcaps, and ρ_0 is the minimum radius of the ring electrode.

The introduction of this electrostatic field affects the trapped ions in a three key ways:

1. A restoring force from the static field gradient confines the axial motion to oscillations at a fixed frequency ω_z

2. The cyclotron frequency is 'modified'/'reduced', noted ω_+

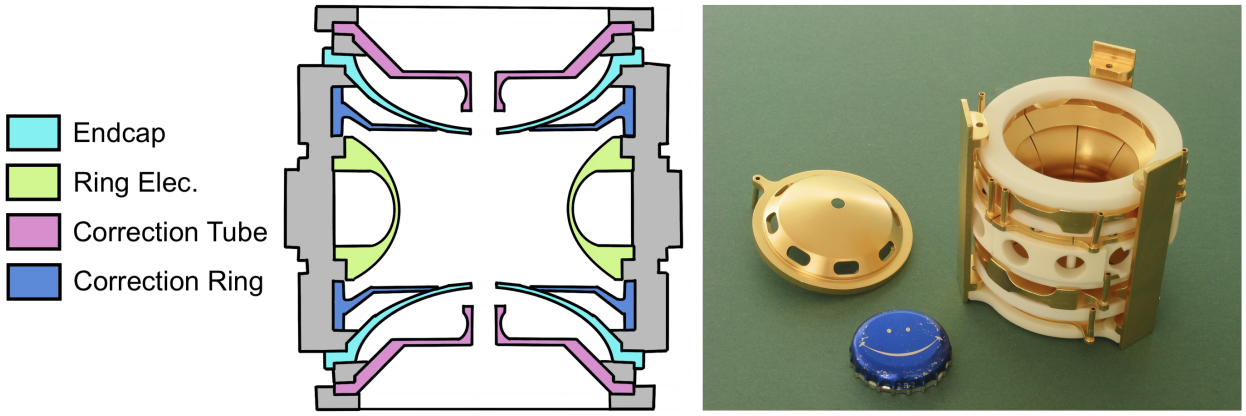

Figure 2.2 (Left) Schematic showing a cross-section view of the LEBIT penning trap, color-coded to show the key electrodes. (Right) The Penning trap installed in the 9.4 T mass spectrometer at LEBIT. Areas colored in gray indicate an insulating material (typically alumina or sapphire).

3. An additional slow magnetron precession is introduced, noted ω_-

A detailed description of these three motions are provided in the following section.

At this stage, the Penning trap is capable of trapping/storing ions with the conditions the ions entered the trap with. It is commonly desired to apply radio-frequency excitations to the stored ions–motivations for which are discussed in the following section. This is achieved by segmenting the ring electrode of the Penning trap into multiple pieces, also shown in Fig. 2.1. Each segment is electrically insulated from the other, such that a dipole or quadrupole excitation scheme can be applied on top of the trapping potential.

In a real Penning trap, two complications arise: (1) the hyperbolic electrodes must be of finite dimension, and (2) holes must be placed in the endcaps to allow ions to enter and exit. The effect of these create a slightly distorted/imperfect quadrupole potential. Of particular concern are the mass-dependent frequency shifts that result from such imperfections. Thankfully, this can be overcome with the addition of correction electrodes which modify the field to very well approximate that of an ideal quadrupolar shape [65]. These are tuned experimentally to minimize systematic frequency shifts which reflect he harmonicity of the net trapping field. Figure 2.2 shows a cross-section view of the Penning trap with the added correction electrodes next to a physical trap in use at LEBIT.

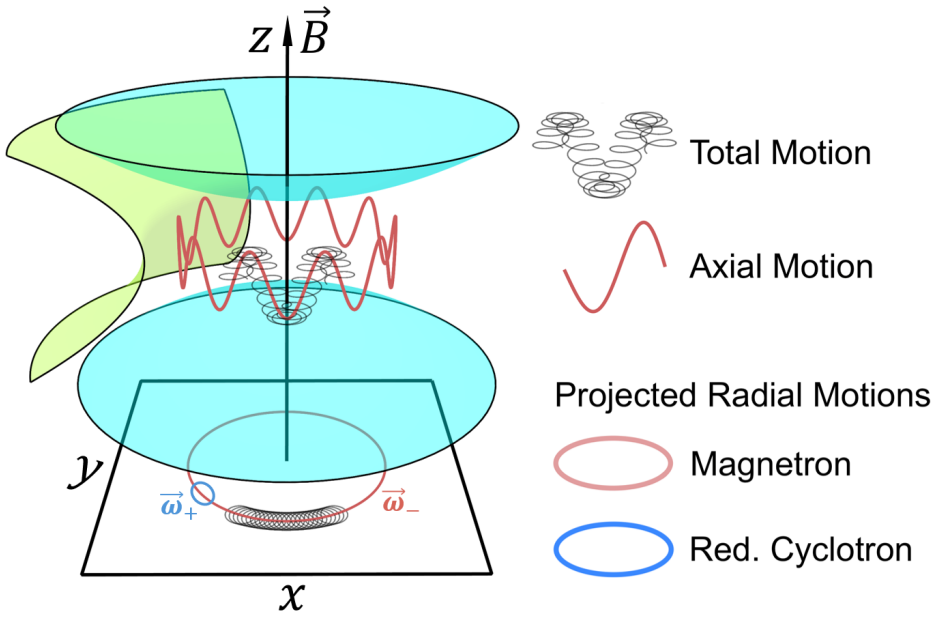

Figure 2.3 The motion of a trapped particle in a Penning trap is a superposition of three eigenmotions: an 'axial' mode, and the radial 'magnetron' and 'reduced cyclotron' modes. The magnetic field is in the z (aka axial) direction. A projection of the ion motion is shown on the xy-plane. The Penning trap endcap electrodes (cyan), and partial ring electrode (green) are also shown. Frequencies and radii are not necessarily to scale.

2.2 Ion Motion and Excitation in a Penning Trap

Ion motion in an ideal Penning trap is known analytically [63], and an abbreviated discussion is presented here to highlight concepts which are important for discussions later in this document. To begin, a trapped particle's motion is a superposition of three eigenmotions: axial (z), magnetron ($-$), and reduced cyclotron ($+$). Figure 2.3 provides a visualization of the relationship between these eigenmotions.

Oscillations in the axial direction are a direct consequence of the electrostatic quadrupole trapping field, which is described by a harmonic oscillator potential when projected on the z axis:

$$\omega_z = \sqrt{\frac{qV_0}{m}\frac{4}{\rho_0^2 + 2z_0^2}} \tag{2.4}$$

The two radial motions are coupled to the magnetic and electrostatic fields, and have frequencies defined by

$$\omega_\pm = \frac{\omega_c}{2} \pm \sqrt{\frac{\omega_c^2 - 2\omega_z^2}{4}}. \tag{2.5}$$

The position of the trapped particle can then be described by the following equations:

$$\begin{aligned} x &= \rho_+ \cos(\omega_+ t + \phi_{+,0}) + \rho_- \cos(\omega_- t + \phi_{-,0}) \\ y &= \rho_+ \sin(\omega_+ t + \phi_{+,0}) + \rho_- \sin(\omega_- t + \phi_{-,0}) \\ z &= \rho_z \cos(\omega_z t + \phi_{z,0}) \end{aligned} \tag{2.6}$$

where $\rho_\pm$, $\phi_{\pm,0}$ and ρ_z, $\phi_{z,0}$ are the radial amplitudes and initial phases of the radial and axial eigenmotions.

The ion cyclotron frequency is now determined from all three eigenfrequencies through

$$\omega_c = \sqrt{\omega_+^2 + \omega_-^2 + \omega_z^2}. \tag{2.7}$$

For a Penning trap perfectly aligned in the magnetic field and with a perfect electrostatic trapping field, it can be shown that summing $\omega_+ + \omega_-$ from Eq. 2.5 result in the axial frequency terms dropping out. Thus we get the following powerful relationship:

$$\omega_c = \omega_+ + \omega_-. \tag{2.8}$$

As discussed in Sec. 2.1, real-world Penning traps can well approximate an ideal quadrupolar electrostatic field, but remain imperfect. The invariance theorem [64] states that even for an imperfect trap, the measured eigenfrequencies still recover the cyclotron frequency through Eq. 2.7. Furthermore, frequency precisions/systematics are often much larger than the frequency shift from an imperfect Penning trap [66], and experimentally, Eq. 2.8 remains a good approximation to these precisions. This is particularly useful as determining the axial frequency to high precision is non-trivial and requires additional considerations.

The eigenfrequencies of each motion in the Penning trap are fixed. The amplitudes of these motions, however, can be damped/excited with the applications of radio-frequency (RF) excitations. For the applications relevant here, only excitations of the radial modes are of interest, which is accomplished by applying the RF excitations to the segmented ring electrodes. The pattern in which the RF is applied determines how the ion motion amplitude and phase is affected [42, 67]. A dipole excitation scheme at $\omega_\pm/2\pi$ directly drives the respective motion amplitude. Notably, for multiple

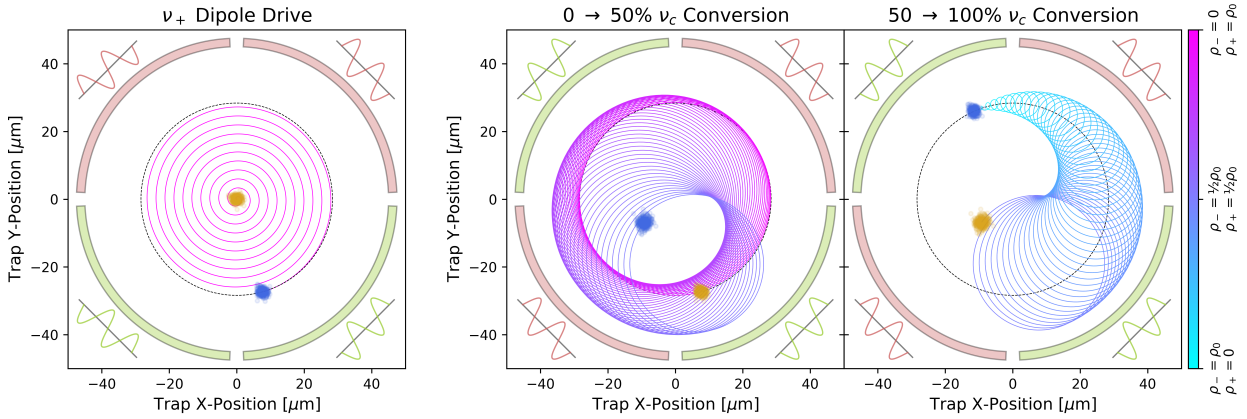

Figure 2.4 (Left) A dipole excitation applied at the ions' ν_+ frequency. (Right) A quadrupole excitation converting initial pure reduced cyclotron motion ($\rho_- = 0$) to pure magnetron motion ($\rho_+ = 0$). For ease of viewing, the conversion pulse is plotted in two halves: the first half results in a 50-50 mix, and the second half completes the conversion. The segmented Penning trap ring electrodes are shown in red and green to indicate the excitation pattern: dimensions are not to scale. Orange and blue points show the ion position at the start and end of each excitation respectively.

ions in the trap, longer RF dipole excitations of $\rho_\pm$ correspond to a tightening of the distribution of $\phi_\pm$ such that the relative ion spatial distribution remains constant regardless of excitation time, see Fig. 2.4(a).

A quadrupolar excitation scheme at ω_c, the $\omega_+ + \omega_-$ sideband, has the effect of coupling the magnetron and reduced cyclotron motions [68]. Over the excitation time, one observes the inter-conversion of the two motions in an oscillatory fashion. For example, consider an ion initially undergoing pure magnetron motion with radius with amplitude a: $a\rho_{-,0}$. After experiencing the above excitation, some of its initial magnetron motion is converted into reduced cyclotron motion: $b\rho_- + c\rho_+$. The characteristic time for one full conversion cycle (e.g. pure magnetron to pure reduced cyclotron and back to pure magnetron motion) is determined by

$$T_{\text{quad, conv}} \approx 0.6\frac{\pi}{V_{\text{rf}}}B\rho_0^2 \tag{2.9}$$

where V_{rf} is the amplitude of the excitation, B is the magnetic field strength, and ρ_0 is again the inner radius of the Penning trap ring electrode. In practice, this conversion relationship is optimized experimentally. Figure 2.4(b) shows the impact of a quadrupole conversion pulse applied to ions

in a Penning trap to convert pure reduced cyclotron motion to pure magnetron motion.

One final consideration for the RF excitations is the frequency bandwidth with which they are applied. Two excitations applied for different times and amplitudes will have the same net effect if the product of time and amplitude is constant. The frequency selectivity, however, will be different due to Fourier series truncations limited by the effective sampling time. In short: longer excitation times will result in a narrower frequency selectivity, with the full width at half maximum of the frequency spectrum determined by

$$\text{FWHM} \propto 1/T_{\text{RF}}. \tag{2.10}$$

This is of particular importance when two different ion species are close in mass, and one desires only to excite one of them.

2.3 Ion Purification in a Penning Trap

Successful Penning trap mass measurements rely on a relatively pure sample of ions inside the trap. Some mass measurement techniques are more resilient to higher levels of contamination (e.g. PI-ICR, FT-ICR) relative to others (e.g. TOF-ICR). Significant contamination also negatively impacts the signal strengths for mass measurements due to additional noise induced by ion-ion interactions inside the trap (see Sec. 5.6). There are several approaches available which limit the amount of contaminant ions in the trap and enable successful measurements. An introduction to the main in-trap methods presented here.

Ion purification in a Penning trap, also known as 'cleaning', takes advantage of the same mass-frequency equivalency used to measure the masses of unknown isotopes. As mentioned in the prior section, a dipole excitation at an ion's reduced cyclotron frequency will excite the motion amplitude to a larger radius. If one knows the contaminant ion mass (and thus its reduced cyclotron frequency), then a dipole excitation can be used to drive the ion's motion to an arbitrarily large radius up to the trap electrodes, effectively removing them from the trap. This procedure is often called 'dipole cleaning' and is a well-established technique [69]. An important consideration when applying the dipole excitation is the power-broadening effects, where a shorter excitation time

results in a wider frequency spread as determined by Eq. 2.10. This becomes particularly relevant when cleaning contaminants near the ion-of-interest where the leaking frequencies may perturb the ion-of-interest.

The challenge of applying the dipole cleaning is the need to know all contaminant species present in the trap. This is non-trivial and often requires significant effort before a measurement begins. Additionally, each cleaning frequency must be mixed together and requires independent arbitrary function generators (AFGs) in practice. Thankfully, there is a broadband cleaning approach which mixes all frequencies within a specified range. The Stored Waveform Inverse Fourier Transform (SWIFT) [70] cleaning technique allows for cleaning of all frequencies outside of a narrow band-gap centered at the ion of interest. In practice, SWIFT is able to clean frequencies within ±1000 Hz outside the center gap due to limited memory storage in most AFGs. This is still sufficient to clean within one mass unit for the majority of cases, where further-off contaminants can be targeted before they enter the trap. The center frequency gap excluded from SWIFT cleaning is usually >200 Hz to avoid perturbations. Targeted dipole cleanings can be used to remove the often few remaining contaminants. Sideband cooling is an additional option for beam purification [71], though this was never intended to be used at LEBIT due to the longer times required which are incompatible for most short-lived radioactive measurements.

2.4 Applying Penning Traps For Mass Measurements

With all the components of a Penning trap in place, applications to mass spectrometry can now be considered. From Eq. 2.1, the mass precision is clearly limited by the precision to which the magnetic field strength and cyclotron frequency are known/determined. The former is of particular consequence, and will be discussed extensively in the sections below. The magnetic field strength is determined through constant calibrations using an atomic/molecular ion which has been previously measured to exceptionally high precision, such as the stable isotopes detailed in the Atomic Mass Evaluation (AME) database [26]. When calibrating the magnetic field in this way, the mass is

determined via a frequency ratio:

$$R = \frac{\omega_{c,\text{calib}}}{\omega_c} = \frac{q_{\text{calib}}\left[m - m_e q + E_b(q)\right]}{q\left[m_{\text{calib}} - m_e q_{\text{calib}} + E_{b,\,\text{calib}}(q_{\text{calib}})\right]}, \tag{2.11}$$

where m_e is the electron mass, q is the charge state, and E_b is the electron binding energy. The subscript 'calib' denotes parameters properties of an ion with very well known mass. Note that Eq. 2.11 presents m as the atomic mass, which is related to the ion mass of Eq. 2.1 by

$$m = m' + q m_e - E_b(q) \tag{2.12}$$

where E_b is the binding energy of the electrons, which is typically orders of magnitude smaller than the nuclear mass precisions of interest and are thus neglected. This change of variable is motivated as it is most convenient to report neutral atomic masses as opposed to one of the many ion masses that might be measured. For the remainder of this document, masses are implicitly for the neutral atom unless otherwise stated.

Equation 2.11 can be easily rearranged to solve for the mass of the atom/molecule being measured:

$$m = \frac{q}{q_{\text{ref}}}\bar{R}\left(m_{\text{calib}} - q_{\text{calib}} m_e\right) + q m_e, \tag{2.13}$$

where $\bar{R}$ indicates the mean ratio over a given number of independent measurements. A key take-away from this relationship is that precise mass measurements are equivalent to precise cyclotron frequency measurements. Two methods for performing these frequency measurements are detailed in Sections 2.5 and 2.6.

2.5 Time-of-Flight Ion Cyclotron Resonance Mass Spectrometry

Time-of-Flight Ion Cyclotron Resonance (TOF-ICR) mass spectrometry measures a resonant frequency/mass by scanning over a range of excitation frequencies and observing the differences in travel time for ions to reach an ion detector, typically a micro-channel plate (MCP). A characteristic resonance curve can then be fit to the frequency and time-of-flight data, which extracts the ion's cyclotron frequency. In this section, the physics principles behind TOF-ICR are first introduced, followed by a discussion of their practical applications for performing mass spectrometry.

First, consider a simple case of a rotating charged particle whose rotational axis is in-line with a magnetic field in the axial direction. This particle has a magnetic dipole moment aligned to the magnetic field with a magnitude of

$$\mu = \frac{E_r}{B_0} \tag{2.14}$$

where E_r is the rotational kinetic energy, and B_0 is the magnetic field strength. If the particle experiences a changing magnetic field in the axial direction, it will experience a net force

$$F_z = -\mu \frac{\delta B}{\delta z}. \tag{2.15}$$

where $\delta B/\delta z$ is the magnetic field gradient. If the ion experiences this gradient and resulting force over a fixed distance, the time for the ion to travel (aka time-of-flight) is inversely proportional to the magnetic dipole moment magnitude, i.e. its rotational kinetic energy.

In essence, if one can modify the rotational energy of an ion, the impact will be seen in the time-of-flight. The cyclotron measurement must then couple the frequency/mass to the rotational energy of the ion. As discussed in Sec. 2.2, the application of a quadrupolar RF excitation at the cyclotron frequency does precisely this: it converts between the radial motions at different frequencies/energies. When trapped, ions initially undergo pure magnetron motion. Note that in a laboratory setting, the strength of the magnetic field and trapping potentials result in the following frequency hierarchy from Eqs. 2.4, 2.5:

$$\omega_- \ll \omega_z \ll \omega_+. \tag{2.16}$$

Applying a full conversion pulse at the ions' cyclotron frequency will transform their motion to the much faster reduced cyclotron frequency, which has significantly higher rotational energy. Ejecting the ions from the trap towards the MCP detector will result in a much shorter time-of-flight in this case.

In practice, the exact cyclotron frequency of the ions is not always well known. As such, a narrow band of frequencies is scanned over. The closer the scanned frequency is to the true ion cyclotron frequency, the more the ion motion will be fully converted to the fast reduced cyclotron

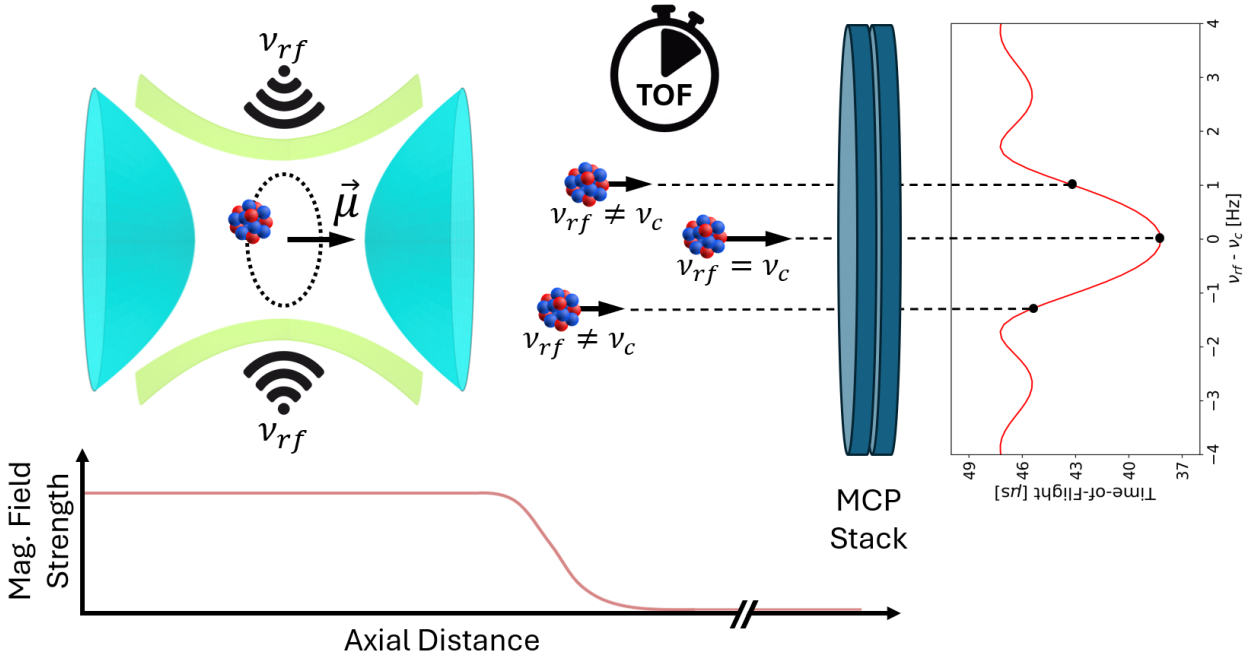

Figure 2.5 Illustration of the time-of-flight ion cyclotron resonance (TOF-ICR) Penning trap mass spectrometry technique (not to scale). Ions are initially captured in the Penning trap undergoing slow magnetron motion, with a small magnetic moment $\vec{\mu}$. A quadrupolar radio-frequency excitation ν_{rf} is applied to the ions: the closer ν_{rf} is the the ion cyclotron frequency ν_c, the more the motion is converted to the faster reduced cyclotron frequency which increases the magnetic moment. Upon ejection from the trap the ions experience the magnetic field gradient and are accelerated relative to their magnetic moment. The time-of-flight is determined once the ions hit a micro-channel plate (MCP) detector, and a characteristic line curve is observed as a function of the applied radio-frequency excitation.

motion. Far away from the true cyclotron frequency, the ions will not be converted and remain in the slow magnetron motion with a long time-of-flight. A theoretical fit to the time-of-flight as a function of the scanned frequency recovers the true cyclotron frequency of the trapped ions [68]. Figure 2.5 provides a conceptual drawing of the TOF-ICR mass measurement process. An example TOF-ICR spectrum and the fitted line curve is shown in Fig. 2.6.

The statistical uncertainty from a TOF-ICR measurement can be described by

$$\frac{\delta m}{m} = \frac{\delta \nu_c}{\nu_c} = \frac{\gamma}{\nu_c T \sqrt{N}} \tag{2.17}$$

where T is the excitation time, N is the number of observed ions, and γ is a constant accounting for system-dependent effects. As such, longer excitation times and more ion counts allow for higher precision with TOF-ICR scan. When applying this technique to radioactive species, the half-life

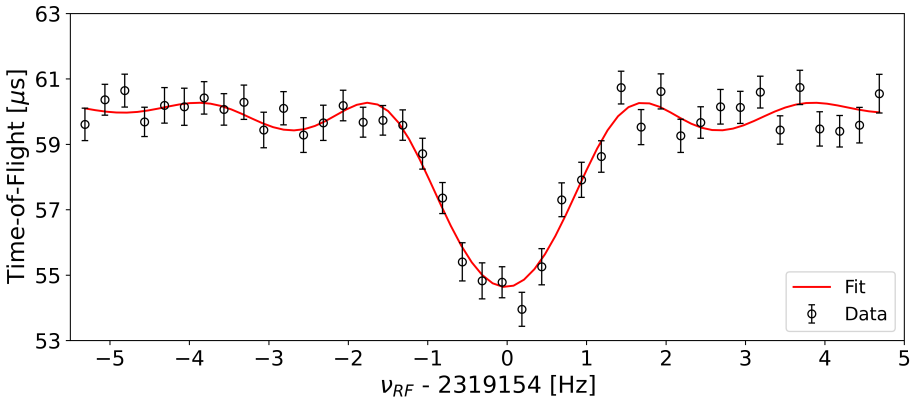

Figure 2.6 Example 500 ms TOF-ICR quadrupole cyclotron frequency resonance for $^{62}Ni^{+}$ with the associated fit. Approximately 1800 ions resolved the frequency to $\delta\nu/\nu \approx 2 \times 10^{-8}$.

determines the possible measurement time and can restrict the achievable precision. Historically, Penning trap mass spectrometry has successfully performed TOF-ICR measurements with ion half-lives down to ~10's of milliseconds [46]. A typical scan often requires > 100 ions in order to meaningfully resolve the fitted ω_c: this can also be challenging for rare isotope mass measurements which may be produced at very low rates, down to only a few per day.

2.6 Phase Imaging Ion Cyclotron Resonance Mass Spectrometry

The Phase Imaging Ion Cyclotron Resonance (PI-ICR) technique is a relatively new method which enables higher mass precisions compared to TOF-ICR, with an order-of-magnitude fewer ions required to complete a measurement [72]. This dramatic improvement is made possible by observing the rotation of the ions with a position sensitive detector: the net angle accumulated by the ions over a set time determines the frequency of rotation. The increased precision comes at the cost of a more complicated measurement procedure, and accounting for systematic effects which become relevant at the higher precisions achieved. This section provides an introduction to the technique with the necessary context. A detailed description to the technique and systematic effects are presented in Chapters 4 & 5. For additional background into PI-ICR, the reader is directed to review Refs. [60].

In the simplest terms, PI-ICR precisely determines a frequency by measuring the angle an ion

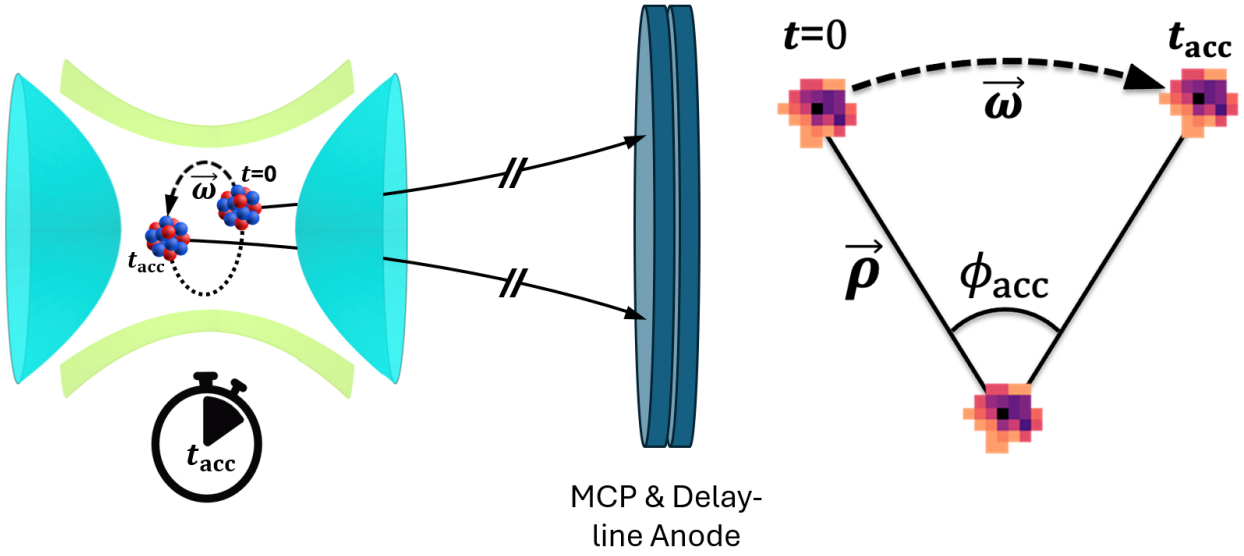

Figure 2.7 Illustration of the phase imaging ion cyclotron resonance (PI-ICR) Penning trap mass spectrometry technique (not to scale). After ions are trapped and excited to achieve the desired frequency of motion ω at a radius ρ, two position measurements are performed. Positions are accurately recorded with a combination micro-channel plate (MCP) detector and delay-line anode. The first at $t = 0$ records the starting angle of the ions. The second allows the ions to accumulate phase for a fixed time t_{acc} and then records the accumulated angle of the ions. The frequency ω is precisely determined by the accumulated phase relative to the starting spot.

traverses (aka *phase*) over a fixed period of time inside a Penning trap. The longer ions spend rotating in the Penning trap, the more precisely we can resolve the frequency. A position-sensitive micro-channel plate (PS-MCP) detector located outside the magnet is used to accurately measure (aka *image*) the angular location of the ions as they rotate in a circle. In practice, PI-ICR uses two position measurements: a start phase (where ions rotate for a net time t_0), and a 'final' phase (where ions rotate for a net time t_{acc}). Then, using the known center-of-motion of the ions, the angular difference between the two phases can be calculated. Figure 2.7 provides a conceptual drawing of the PI-ICR measurement process.

In typical Penning trap setups, like at LEBIT, the frequencies being measured are ~1 MHz with typical trapping times ~100 ms: such ions can complete ~100 000 full rotations. With this in mind, it would seem incompatible with the measurement scheme presented in Fig. 2.7, which can only resolve angles within one full rotation. This is only a concern if one has no prior knowledge about the ions mass; in reality we can use prior low precision measurements and theory predictions

(such as those listed in the Atomic Mass Evaluation [26]) to inform the measurement. Given an initial mass/frequency uncertainty of $\delta\nu$, we can safely allow the ions to rotate for $t_{\text{acc}} = 1/\delta\nu$ while knowing exactly how many full rotations (plus a little extra) the ions will complete in the trap. As such, the presented measurement scheme provides the unknown phase information resulting from the initial limited mass precision.

Finally, the frequency of rotation is calculated from

$$\omega = 2\pi\nu = \frac{\phi_{\text{acc}} + 2\pi N}{t_{\text{acc}}} \tag{2.18}$$

where $N = \text{floor}[\nu_0 t_{\text{acc}}]$ is the number of full rotations the ion completes in the trap, ϕ_{acc} is the net angle the ions rotate over the measurement time t_{acc}. Extracting the cyclotron frequency using this procedure requires a few additional considerations, and discussed in Sec. 4.3. Figure 2.8 shows an example phase measurement completed at LEBIT, reported in [45].

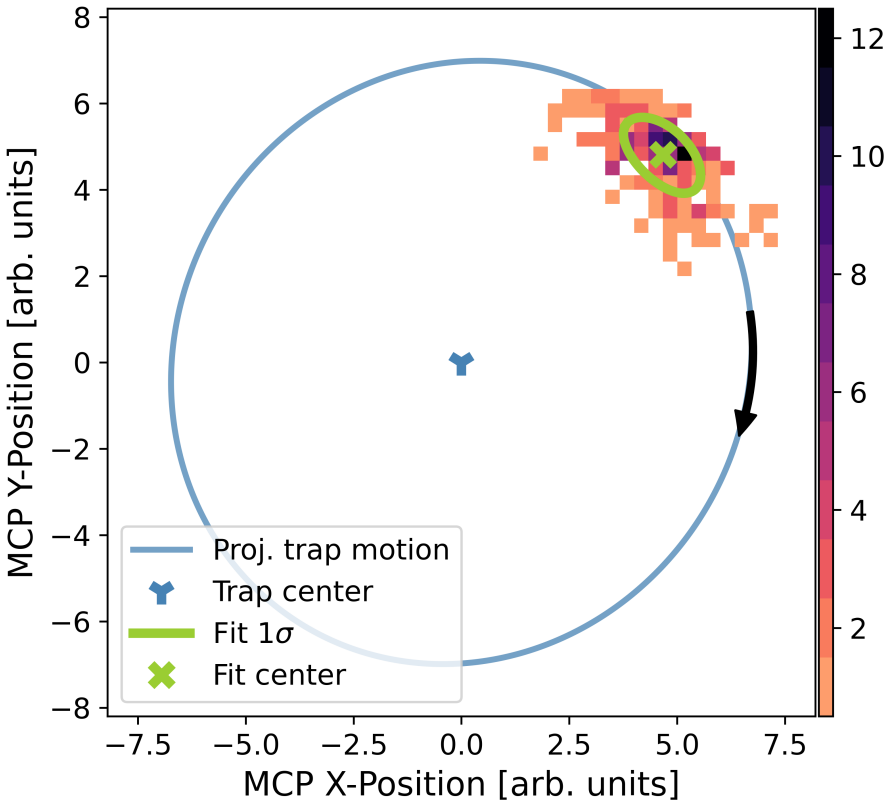

Figure 2.8 An example of a PI-ICR phase measurement for $^{39}K^{+}$, after the ions were allowed to accumulate reduced cyclotron phase for 250 ms. The elliptical projection of the ion motion shows the radius of motion, highlighting also the 'tightness' of the ion spot. Approximately 200 ions resolve the frequency to $\delta\nu/\nu \approx 1 \times 10^{-8}$.

CHAPTER 3

LOW ENERGY BEAM ION TRAP FACILITY AT FRIB

The Low Energy Beam Ion Trap (LEBIT) facility is located at the Facility for Rare Isotope Beams (FRIB) on the Michigan State University campus in East Lansing, MI USA. FRIB is a state-of-the-art rare isotope facility designed to be the most powerful heavy-ion accelerator to provide unprecedented access to exotic isotopes. LEBIT performs high-precision mass spectrometry for these isotopes, shedding critical mass information for a wide range of nuclear science fields. In this chapter, an overview of the experimental facilities is provided, detailing the production of rare isotopes, preparation for measurement, and finally the dedicated precision mass measurement area.

3.1 Rare Isotope Production and Delivery at FRIB

FRIB produces rare isotopes far from nuclear stability using projectile fragmentation [73]. Figure 3.1 provides an overview of the main components of the Facility for Rare Isotope Beams. The primary beam, such as stable ^{36}Ar among many others, is first accelerated from rest with the superconducting FRIB linear accelerator to more than 50% the speed of light. The beam with energy of $\approx$ 200 MeV/u is then impinged on a natural carbon target of about 8 mm thickness, which fragments the primary beam into many different isotopes. The isotope of interest for a given experiment must then be filtered from the cocktail beam with the Advanced Rare Isotope Separator (ARIS) [74].

ARIS is a three-stage magnetic spectrometer for fragment separation with a 10% momentum acceptance and ±40 mrad angular acceptance in both transverse directions. The system utilizes wedge degraders to aid in secondary beam purification. The final focal plane contains detectors for energy loss and total kinetic energy for particle identification. The separated beam can then be delivered to the fast beam experimental area, stopped beam experimental area, or the re-accelerator. LEBIT is located in the stopped beam area, which requires the beam from ARIS to be slowed down from $\approx$ 200 MeV/u energy to just a few eV with gas stoppers.

FRIB's gas stopping area utilizes gas catchers to reduce the beam energy to levels suitable

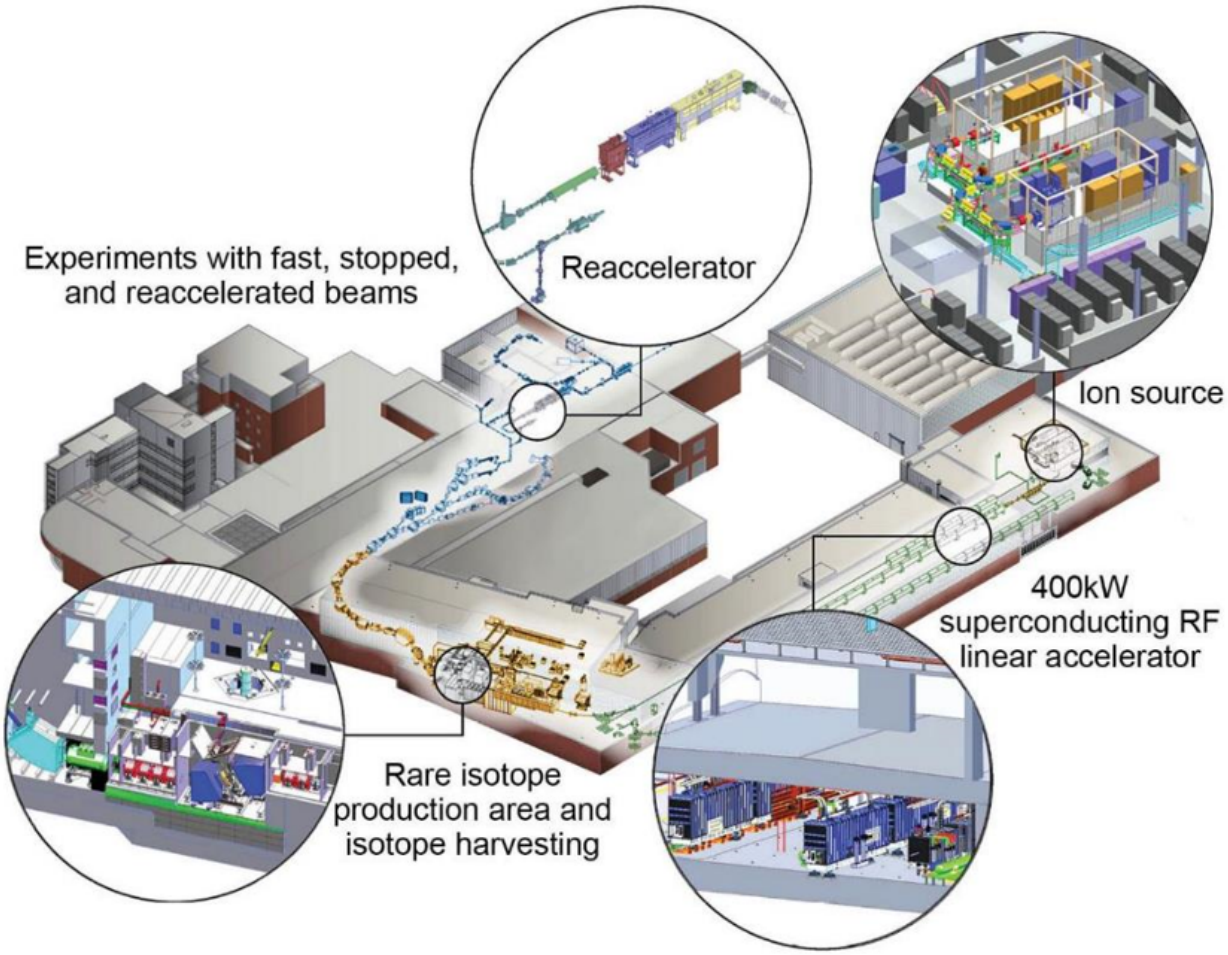

Figure 3.1 Overview of the Facility for Rare Isotope Beams (FRIB). A superconducting radio frequency linear accelerator brings stable ions up to ≈50% the speed of light before they are impinged upon a natural carbon target. The ions undergo projectile fragmentation which produces many different rare isotopes. This 'cocktail' beam is then filtered in-flight to separate the one rare isotope of interest from the rest of the beam, which is then sent to the experimental areas.

for precision measurements. Two different gas catchers are available: the Argonne National Laboratory (ANL) gas cell [75], and the Advanced Cryogenic Gas Stopper (ACGS) [76]. The operating principles of both systems are unique, though only ACGS will be discussed here. Prior to entering ACGS, the fast beam is passed through a series of aluminum degrader plates and an aluminum wedge to coarsely reduce the beam momentum so that it can be fully stopped in the gas cell volume. The beam is then sent into ACGS, where continuous collisions with an ultra-pure helium buffer gas at 40 K reduce the beam energy until it is fully at rest. The cryogenic temperatures help freeze out contamination and minimize molecular recombination of the rare isotopes. During the stopping process, the highly ionized beam will recapture electrons from the helium gas until a 1^+ (and on occasion 2^+ or 3^+) charge state is reached. It is energetically unfavorable for the ions to strip additional electrons from the helium atoms beyond this point.

After the rare isotope beam has been stopped, a combination radio-frequency field and DC field gradient prevent collisions with the chamber walls and direct the beam to a small extraction hole. The beam stopping area is seated on a 30 kV high-voltage platform, providing the necessary energy to transport the beam to downstream experimental areas. After exiting ACGS, a three stage radio-frequency quadrupole ion guide with differential pumping transports the low energy beam to a magnetic dipole mass separator. With a resolving power of $m/\delta m \approx 1500$, this final stage of purification allows for a coarse mass-to-charge filtering and removes a majority of molecular contaminants generated by the stopping process. The beam is then sent to experimental areas, such as the LEBIT facility.

3.2 Overview of the LEBIT Facility

A schematic layout of the LEBIT facility can be seen in Fig. 3.2. Rare isotope beams are delivered from the gas stopping facility with an energy of 30 keV/q. LEBIT is situated on a 30 kV high-voltage (HV) platform, which shares a HV bias power supply with the gas stopping area, restoring the ions to ~eV. A separate high voltage DC power supply connected to the LEBIT HV platform allows for a fine tuning of the incoming beam energy. This section discusses the

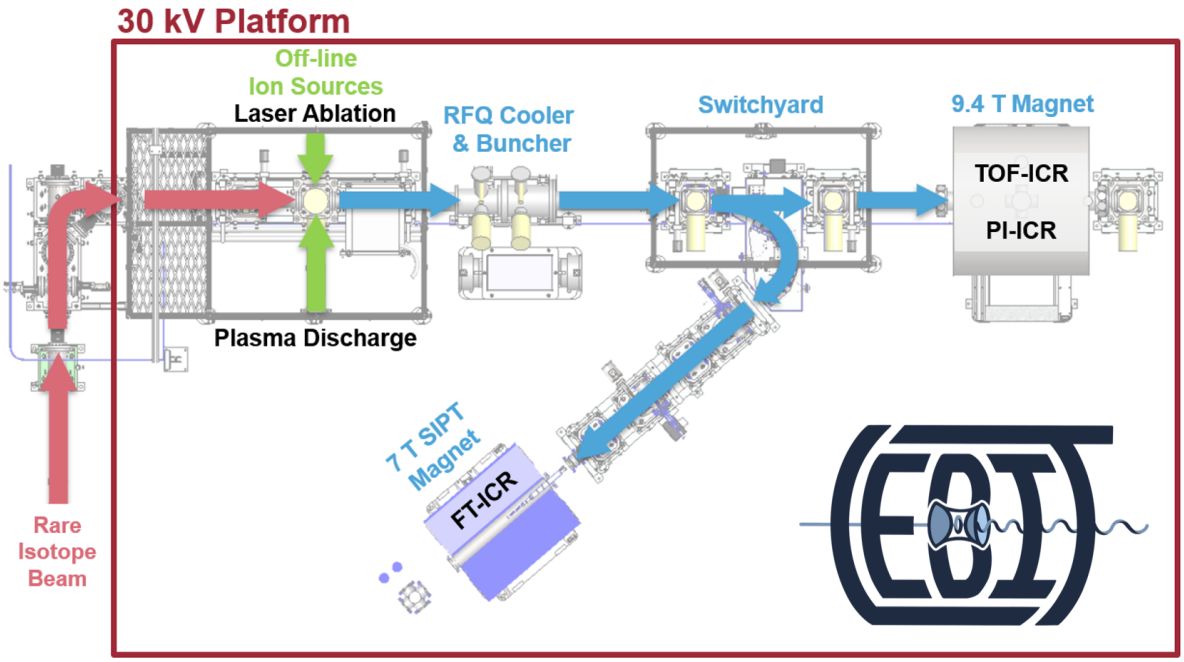

Figure 3.2 Overview of the main components of the Low Energy Beam Ion Trap facility. Rare isotopes enter the experimental area (red arrows) with an energy of 30 keV from the FRIB gas stopping area. A 30 kV high-voltage platform removes nearly all this energy. Ions are then sent to a radio-frequency quadrupole (RFQ) cooler and buncher where the ions are stripped of any remaining energy through interactions with a helium buffer gas. The low energy ions (blue arrows) can then be delivered to the Penning traps for measurement.

components of LEBIT that follow, preparing the beam for precision mass measurements.

3.2.1 Offline Ion Sources

LEBIT utilizes two independent offline ion sources: a Colutron plasma ion source–aka the Thermal Ion Source (TIS)–and a laser ablation source (LAS) [77]. Both provide stable beams over a large range of masses for beam diagnostics, beamline tuning, and during experiments as a source of well known masses for calibration. A 90-degree quadrupole bender mounted in the main beamline allows for selection between the rare isotope beam, or either of the offline ion sources to be delivered downstream.

The TIS source produces ions via a hot tungsten filament in a ceramic oven, with a gas inlet via a leak valve. The filament is heated with a high current supply, and an additional voltage bias across the filament may also be added. A positive bias acts to drive off alkali metal impurities

in the tungsten filament as positively charged ions: $^{23}Na^{+}$, $^{39,41}K^{+}$, $^{85,87}Rb^{+}$, and $^{133}Cs^{+}$ are most easily produced. A negative bias creates a discharge from electrons boiled off the filament, ionizing the gas flowing into the oven (e.g. $^{20-22}Ne$, $^{36,40}Ar$, and $^{78,80,82-84,86}Kr$). The TIS was used to provide both $^{23}Na^{+}$ and $^{22}Ne^{+}$ which were used for calibration and systematic studies of the ^{22}Al measurement discussed in Chapter 6.

The LAS uses a pulsed neodymium-doped yttrium aluminum garnet (Nd:YAG) laser from Quantel Laser to provide 532 nm green light pulses on solid targets. The laser beam is highly focused at the target, heating surface atoms to ionization, creating positively charged ions. The solid target is mounted to a stepper motor to continuously rotate the material, spreading the laser pulses over a large area and increasing the target lifetime. The current setup allows for two semi-circle targets to be mounted at once, and the rotating motor can be remotely switched between them. Many different solid target materials can be used to produce a wide range of stable beams.

3.2.2 Radio Frequency Quadrupole Cooler and Buncher

LEBIT requires a 'cooler buncher' to remove any residual beam energy spread, and to convert the continuous ion beams into short pulses compatible for the Penning trap measurements. Ion pulses are required for the precise timing requirements for the TOF-ICR and PI-ICR measurements discussed in Chapter 2. The design at LEBIT is a three-staged gas filled linear Paul trap [78], each of which uses a RFQ to radially confine the ions, and an axial DC drift field to pull the ions through the device.

The first stage of the cooler buncher is referred to as the 'pre-cooler' and acts to dissipate a majority of the ion energy through collisions with high-purity helium buffer gas. The second stage is the micro-RFQ which connects the first and third sections, providing differential pumping to maintain the high vacuum required downstream. The final section serves to further thermalize and accumulate the ions before ejecting them in a short, low-emittance pulse.

Following the cooler buncher, the ions are sent through a voltage-pulsed drift tube to fine-tune the ions' energy for optimal injection and capture in the Penning trap. The beam can then be sent

directly to the 9.4 T Penning trap, or can be switched to the secondary SIPT delivery beamline. To be directed into SIPT, ions are passed first through a 25° spherical kicker, a series of two electrostatic quadrupoles, a 115° cylindrical bender which is split by another electrostatic quadrupole, and a final series of two electrostatic quadrupoles.

3.2.3 9.4 Tesla Precision Penning Trap

Before entering the 9.4 T Penning trap, as seen in Fig. 3.3, ions pass through a coarse time-of-flight gate allowing for ion filtering to approximately 1 amu/q. The gate is comprised of an electrostatic steering element grounded for ~50 ns centered at the desired time-of-flight, and 1 kV at all other times to steer the ions off of the beamline. A series of three Einzel lenses provide a final focusing before injection into the magnet. Additional injection optics guide the ions into the magnetic field and reduce their energy for optimal capture in the Penning trap. LEBIT utilizes a set of Lorentz steerers [79] in the magnetic field just prior to the trap to precisely control the initial magnetron orbit of the ions in the trap depending on the desired measurement conditions.

LEBIT can remotely switch between two mass measurement configurations: a time-of-flight (TOF-ICR) or a phase imaging (PI-ICR) technique which are discussed in detail in the following chapter. Regardless of the technique, the beamline remains essentially unchanged and both follow the same general procedure. Once ions are ejected from the trap, they leave the magnetic field through a series of electrostatic drift tubes which accelerate the ions towards a micro-channel plate (MCP) detector. For TOF-ICR, the detector is mounted in the Daly configuration [80]. A strong negative potential on the aluminum Daly collector plate guides the positively charged ions to strike its surface and an amplified electron shower is then accelerated to the positively biased MCP detector. This approach produces a reliable signal with an effective 100% detection efficiency. PI-ICR requires a position sensitive detector, which is achieved with a normal MCP detector and a delay-line anode. The development of the PI-ICR technique is the primary focus of Chapter 4, and a detailed description of the detection scheme is provided there.

Figure 3.3 Image of the 9.4 T Penning trap mass spectrometer at the Low Energy Beam Ion Trap (LEBIT) facility.

3.2.4 7 Tesla Single Ion Penning Trap

The Single Ion Penning Trap (SIPT) beamline is an extension of the original LEBIT beamline, with the intent to measure exotic radioactive isotopes with the lowest production rates at FRIB. A 25° spherical kicker diverts the ions from the cooler and buncher into the SIPT beamline. Ions then move through a series of two electrostatic quadrupoles, a two-part 115° cylindrical bender with another electrostatic quadrupole between, and then two additional electrostatic quadrupoles. These elements provide all the necessary steering and focusing for to complete the full bend. Ions are then focused into the SIPT Penning trap with two additional Einzel lenses followed by a series of drift tubes. SIPT is configured such that both the time-of-flight and Fourier-transform

ion cyclotron resonance techniques can be used, but is highly optimized for the Fourier-transform method. Current development efforts for the SIPT project are beyond the scope of this work: interested readers are directed to review Refs. [58, 59, 81] for additional information, which include contributions by the author.

CHAPTER 4

INTEGRATION OF PI-ICR AT LEBIT

LEBIT has successfully used PI-ICR since 2023 for multiple rare isotope experiments [45, 62] where TOF-ICR measurements would not have been able to reach the necessary precision, or be possible in the first place. For additional details regarding the design of PI-ICR at LEBIT, see the dissertation by I.T. Yandow [61]. A brief discussion of the relevant hardware and additional considerations for PI-ICR are presented here.

4.1 Experimental Setup

At LEBIT, the 9.4 T superconducting magnet is utilized for both the TOF-ICR and PI-ICR techniques. Switching between the two techniques is straightforward:

- A 'Lorentz steerer' [79] before the Penning trap is switched to direct ions to the center of the trap (for PI-ICR) or at some radius (for TOF-ICR).
- Arbitrary function generators used to apply trap RF excitations are selected remotely.
- A pneumatic actuator removes the TOF-ICR MCP detector from the beamline and replaces it with a drift tube element directly in front of the position sensitive MCP detector for PI-ICR.

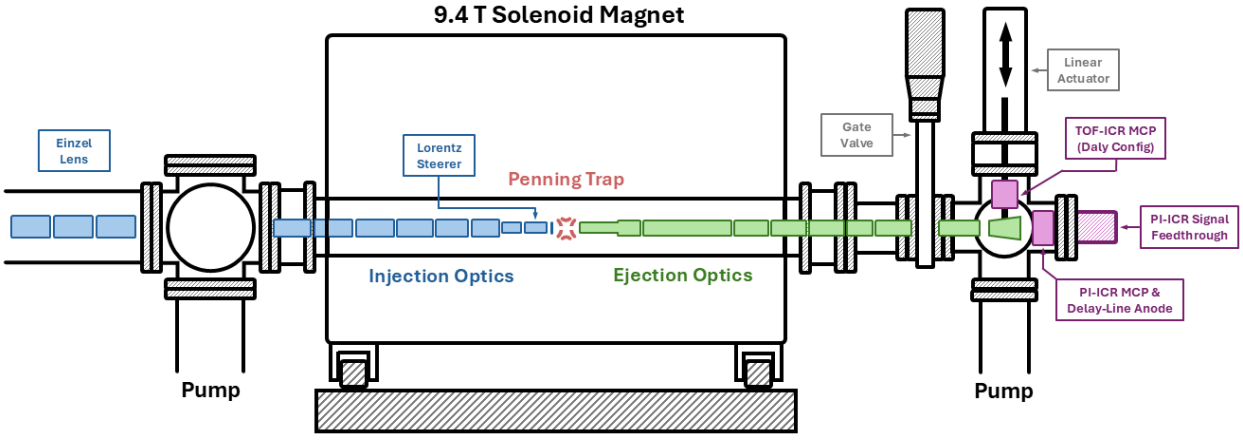

Figure 4.1 Illustration of the key beamline elements for the PI-ICR measurement and detection scheme implemented at LEBIT. Dimensions not necessarily to scale.

- The 'ejection drift tube section' potential gradient is adjusted to either TOF-ICR (slower drift field required) or PI-ICR (faster drift field required).

All these operations are performed remotely with the LEBIT control system. Figure 4.1 provides an overview of these key elements.

Since it is much faster to setup/analyze TOF-ICR measurements, the ability to very quickly cycle between measurement techniques holds several key advantages during an experimental campaign. First, TOF-ICR enables a very fast optimization of the beamline optics for transmission, trapping timing/efficiency, etc. Second, during an experiment TOF-ICR can identify contaminant ions delivered in the rare isotope beam much faster than possible with PI-ICR. Lastly, having two independent measurement techniques provides a good systematics cross-check, and for some experiments TOF-ICR can provide a higher precision frequency guess for PI-ICR.

The use of a Lorentz steerer to precisely inject ions to the center of the Penning trap is currently unique to the LEBIT facility (though other Penning trap facilities are now moving to add them as well). This is particularly beneficial to LEBIT, which does not have a 'preparation Penning trap' [82] capable of achieving the same on-center injection needed for PI-ICR. Without a preparation Penning trap to fully cool the ion motion inside the magnetic field, it is important that LEBIT use the Lorentz steerer to inject ions parallel to the magnetic field and precisely capture ions in the Penning trap to minimize their initial energy.

4.2 Detectors and Data Acquisition

The 'phase-imaging' aspect of PI-ICR requires a position-sensitive detector to accurately measure the location of ions. At LEBIT, this is accomplished with a micro-channel plate (MCP) detector in combination with a two-axis delay-line anode [83] supplied by RoentDek Handels GmbH. The MCP creates an electron shower, whose current signal is picked up on the delay line wires, and the time difference for the current signal to travel to either end of the wire uniquely determines position in one dimension. Using two sets of wires configured perpendicular to one another gives the two-dimensional position.

Signal conditioning and processing is required to reliably extract full position information for each ion hit. The MCP and delay-line anode signals are first sent to the RoentDek FT-12 passive signal decoupler which removes the high voltage bias from the respective detectors in preparation for further processing. Signals are then sent through time-matched cables to the RoentDek ATR-19 amplification module. Each signal is independently amplified and sent through a constant fraction discriminator to isolate ion signals from the noise floor. Lastly, discriminated signals are sent through time-matched cables to a fast time-to-digital converter (TDC) with 25 ps resolution. A custom driver for the TDC card maintained by Dennis Neidherr at GSI Helmholtzzentrum GmbH provides a signal veto between two additional timing signals: (1) ejection of ions from the trap, and (2) a time-of-flight delay for ions to hit the MCP. This veto feature removes significant amounts of background noise and MCP dark-count signals given the time-of-flight window ~10 μs compared to the measurement cycle time of ~500 ms.

Following digitization, additional software is required to process the timestamps and calculate position information for each hit. There are limitations when considering both high-rate and spatially dense operations on the MCP. When two ion hits are near-coincident (within the ~30 ns time-spread of the delay-line anodes), it is not always possible to disentangle the position information for each hit resulting in 'lost data.' This is further exacerbated when the hits are spatially close on the detector such that the delay-line signals overlap. Additional limitations arise from the noise floor and discrimination thresholds which can cause occasional miss-triggers. For the majority of use cases for PI-ICR, these limits are a non-issue. These can become relevant in the extreme cases of very low-rate (where every signal matters) or high-rate experiments (often highly contaminated beams with only a few signals from ions of interest).

4.3 Measurement Cycle

Ions are captured at the center of the Penning trap such that they have an initial radius $\rho \approx 0$. Any small residual motion will be comprised of pure magnetron motion. Similar to SHIPTRAP, LEBIT then scans over one period of the magnetron frequency. This has the effect of averaging out

any phase dependence in the magnetron motion that may occur later in the measurement process. Next, any target dipole cleaning pulses are applied to remove contaminants, along with SWIFT if needed. At this point the ions remaining in the trap are ready for measurement.

There are two principle methods to completing cyclotron frequency (and hence mass) measurements with PI-ICR. Regardless of measurement style, a general scheme is applied:

1. A dipole RF excitation ($t_d \sim 1$ ms) is applied at the ion's reduced cyclotron frequency ν_+, driving the ions to a large reduced cyclotron radius.

2. Ions are allowed to evolve for a fixed time $t_{\text{acc},+}$, where they accumulate reduced cyclotron phase.

3. A quadrupole RF excitation ($t_q \sim 1$ ms) is applied at the ion's cyclotron frequency ν_c, with the amplitude set to fully convert the reduced cyclotron motion to pure magnetron motion.

4. Ions are allowed to evolve again for a fixed time $t_{\text{acc,-}}$, where they accumulate magnetron phase.

5. The trap is opened, and all ions are quickly ejected to the position sensitive MCP detector.

It can be shown from the equations of motion under these different manipulations (see [67] for derivations) that the final phase of the ion is given by

$$\phi = [2\pi\nu_- + \pi(\nu_q - \nu_c)]t_q - \pi(\nu_d + \nu_+)t_d - 2\pi\nu_+ t_{\text{acc},+} + 2\pi\nu_- t_{\text{acc,-}} + \phi_q - \phi_d + 2\pi N \qquad (4.1)$$

where ν_d, ν_q, ϕ_d, and ϕ_q are the frequencies and initial phases of the dipole and quadrupole excitations respectively; ν_c, ν_+, and ν_- are the eigenmotions of the ion; N is the number of full cycles the ion undergoes during it's various phases of motion, given by

$$N = \lfloor \nu_+(t_d + t_{\text{acc},+}) \rfloor - \lfloor \nu_-(t_q + t_{\text{acc,-}}) \rfloor \, . \qquad (4.2)$$

Equation 4.1 holds in the case where all excitations are resonant: the difference between the applied frequency and the true frequency is well within the Fourier width $\approx 1/t_{\text{excit}}$. In such cases, $\nu_q = \nu_c$

and $\nu_d = \nu_+$ resulting in

$$\phi = 2\pi\nu_-(t_q + t_{\text{acc,-}}) - 2\pi\nu_+(t_d + t_{\text{acc,+}}) + \phi_q - \phi_d + 2\pi N \ . \tag{4.3}$$

Measuring the resulting phase for two different timing combinations, ϕ_0 and ϕ_{acc}, and taking the difference for the resulting equations allows one to solve for one the unknown frequencies (or the sum $\nu_+ + \nu_-$ if the timings are carefully selected). The following sections detail a selection of these potential schemes.

4.3.1 Direct Cyclotron Frequency Measurement

The 'direct' approach to measuring the cyclotron frequency ν_c is detailed in [72, 84], and requires two iterations of the measurement cycle: one to generate a 'start'/'reference' phase where $t^0_{\text{acc,-}} \gg t^0_{\text{acc,+}}$, and another to generate a 'final' phase where $t'_{\text{acc,+}} \gg t'_{\text{acc,-}}$. It can be shown from Eq. 4.3 that the cyclotron frequency will be directly recovered when the total trapping time is conserved for both the start and final phases:

$$t^0_d + t^0_{\text{acc,+}} + t^0_q + t^0_{\text{acc,-}} = t'_d + t'_{\text{acc,+}} + t'_q + t'_{\text{acc,-}}. \tag{4.4}$$

Note that the optimal/simplest timing configuration for the highest precision would be the following:

$$t^0_d = t'_d, \quad t^0_q = t'_q, \quad t^0_{\text{acc,-}} = \tau, \quad t^0_{\text{acc,+}} = 0, \quad t'_{\text{acc,-}} = 0, \quad t'_{\text{acc,+}} = \tau.$$

Small adjustments can then be made to align the spots to the desired angular location, while still ensuring the total trapping time is conserved. LEBIT does not currently utilize this measurement approach, as it tends to be too cumbersome for the majority of the measurements we perform. Instead, LEBIT opts for the two-phase approach, which is significantly more flexible as will be discussed in the following sections.

4.3.2 Indirect Cyclotron Frequency Measurement

The 'indirect' approach to measuring the cyclotron frequency determines the cyclotron frequency via Eq. 2.8 by measuring the reduced cyclotron and magnetron frequencies independently. This can be accomplished with three iterations of the measurement cycle:

1. A 'start' phase ϕ^0 with $t^0_{\text{acc,-}} \geq 0,\ t^0_{\text{acc,+}} \geq 0$

2. A 'magnetron phase' $\phi^\dagger_-$ with $t^\dagger_{\text{acc,-}} \gg t^0_{\text{acc,-}},\ t_{\text{acc,+}} = t^0_{\text{acc,+}}$

3. A 'reduced cyclotron phase' $\phi^\dagger_+$ with $t_{\text{acc,-}} = t^0_{\text{acc,-}},\ t^\dagger_{\text{acc,+}} \gg t^0_{\text{acc,+}}$

There are no restrictions on $t^\dagger_{\text{acc,-}}$ or $t^\dagger_{\text{acc,+}}$. The relevant frequency is determined by the relative angle between the start spot and each accumulated phase spot, respectively.

An important consideration for these measurements is the direction of the radial motion of the ions in the trap. Both the magnetron and reduced cyclotron motions are oriented in the same direction within the trap. However, the application of the quadrupole conversion pulse has the effect of inverting the observed phase of the reduced cyclotron motion accumulated by the ions, as detailed in [67]. The following equations assume that the magnetron motion accumulates positive phase, i.e. moves in a counter-clockwise direction, a trivial inversion recovers the equations for the opposite case. The frequency of motion is then determined as

$$\nu_\pm = \frac{\mp\frac{1}{2\pi}\left(\phi^\dagger_\pm - \phi^0\right) \pm \left(N^\dagger_\pm - N^0\right)}{t^\dagger_{\text{acc},\pm} - t^0_{\text{acc},\pm}}\ . \tag{4.5}$$

4.3.3 LEBIT Measurement Cycle

For the applications relevant to LEBIT, the indirect cyclotron frequency measurement is best suited. The flexibility for the measurement expedites the setup time and simplifies an experiment compared to the restrictions for the direct cyclotron measurements of Sec. 4.3.1. Additionally, measuring the magnetron and reduced cyclotron frequencies independently provides a higher precision cyclotron frequency (at the expense of taking an additional spot dataset). During an experiment, it is almost always possible to take calibration measurements with an isobaric contaminant. Given that the magnetron frequency is largely mass independent ($\nu_- \approx 1.8$ kHz with a mass-shift of ≈ 0.02 Hz/amu at LEBIT), the calibrant species magnetron frequency measurements can be used for the rare isotope of interest. Since the calibrant is high-rate, these measurements are very fast, allowing for rare isotope measurements to consist solely of a start spot and reduced cyclotron

phase spot. The end result is a higher precision rare isotope frequency measurement with minimal additional experimental time.

The cycle described in Sec. 4.3.2 works well for a perfect Penning trap. However, as detailed later in Chapter 5, in an imperfect setup where the ions arrive at the MCP detector with a non-circular projection, the angle of each spot type must be kept the same to eliminate additional systematic uncertainties. The above cycle does not necessarily allow for this necessary adjustment. It is straightforward to reposition the spots by adjusting the magnetron accumulation time which has a period of ~550 μs relative to the 25 ns system timing resolution. Note that adjustments to the reduced cyclotron accumulation time are not as straightforward, as they have periods of ~200 ns up to ~1 μs: the granularity isn't always sufficient to finely adjust the spot location. With this in mind, consider that for each spot the magnetron accumulation time can be adjusted such that they all appear at the same angle on the MCP. The indirect frequency measurement cycle in use at LEBIT then looks like:

1. A 'start' phase ϕ^0 with $t^0_{\text{acc,-}} \geq 0,\ t^0_{\text{acc,+}} \geq 0$
2. A 'magnetron phase' $\phi^\dagger_-$ with $t^\dagger_{\text{acc,-}} \gg t^0_{\text{acc,-}},\ t_{\text{acc,+}} = t^0_{\text{acc,+}}$
3. A 'reduced cyclotron phase' $\phi^\ddagger_+$ with $t^\ddagger_{\text{acc,-}} \geq 0,\ t^\ddagger_{\text{acc,+}} \gg t^0_{\text{acc,+}}$

The start and magnetron phase measurements remain unchanged in principle, and Eq. 4.5 still holds for determining ν_-. To determine ν_+, a correction to the phase is required to account for the non-zero magnetron phase accumulation:

$$\nu_+ = \frac{-\frac{1}{2\pi}\left(\phi^\ddagger_+ - \phi^0\right) + \nu_-\left(t^\ddagger_{\text{acc,-}} - t^0_{\text{acc,-}}\right) + \left(N^\ddagger_+ - N^0\right)}{t^\ddagger_{\text{acc,+}} - t^0_{\text{acc,+}}} \tag{4.6}$$

Note that Eq. 4.6 now introduces a dependence on ν_-: this doesn't pose an issue as ν_- is measured independently to high precision with no corresponding ν_+ dependence.

4.3.4 Mixed Measurement Cycle

A novel approach for PI-ICR measurements has been recently developed and demonstrated at LEBIT for the lowest-rate measurements. This is accomplished by using the start phase from a

high-rate calibrant species to determine the reduced cyclotron phase for the ion of interest, reducing the required counts by half. A derivation of the ion phase advance motivating the new approach is presented, and a procedure for a cyclotron frequency measurement is provided in the following discussion.

Traditionally, the same ion species is used to generate both the reference and accumulated phase measurements to account for any small mass dependent effects inherent to the PI-ICR cycle. However, in the case of low rate measurements, it is worth considering a 'mixed' measurement approach where an abundant near-mass calibrant species is used as the start phase for the low-rate rare isotope. Consider a spot generated from a well-known calibrant species with frequencies ν_+, and ν_-:

$$\phi_{\text{start}} = 2\pi\nu_-(t_q + t_{\text{acc,-}}) - 2\pi\nu_+(t_d + t_{\text{acc,+}}) + \phi_q - \phi_d + 2\pi N \tag{4.7}$$

Next, consider the final phase for the second ion species, where the (*) superscript will be used to denote the new timings and frequencies:

$$\phi^*_{\text{acc}} = 2\pi\nu^*_-(t^*_q + t^*_{\text{acc,-}}) - 2\pi\nu^*_+(t^*_d + t^*_{\text{acc,+}}) + \phi^*_q - \phi^*_d + 2\pi N^* \tag{4.8}$$

We assume that $\nu^*_- = \nu_-$ (i.e. the calibrant and ion of interest are close in mass). Additionally, we assume that the initial excitation phases ϕ_q, ϕ_d are the same between the calibrant and ion of interest measurements. In practice, this is easily accomplished with phase-locked function generators (e.g. running in gated burst, N burst, etc.). Re-arranging and combining like terms, the phase can then be written as

$$\phi^*_{\text{acc}} = 2\pi\nu_-(t^*_q + t^*_{\text{acc,-}} - t_q - t_{\text{acc,-}}) + 2\pi\nu_+(t_d + t_{\text{acc,+}}) - 2\pi\nu^*_+(t^*_d + t^*_{\text{acc,+}}) + \phi_{\text{start}} + 2\pi(N^* - N)\ . \tag{4.9}$$

Finally, we can solve this equation to recover the 'unknown' frequency of interest, ν^*_+ in terms of the known timings and calibrant frequencies:

$$\nu^*_+ = \frac{-\frac{1}{2\pi}(\phi^*_{\text{acc}} - \phi_{\text{start}}) + \nu_-(t^*_q + t^*_{\text{acc,-}} - t_q - t_{\text{acc,-}}) + \nu_+(t_d + t_{\text{acc,+}}) + (N^* - N)}{t^*_d + t^*_{\text{acc,+}}}\ , \tag{4.10}$$

which has an uncertainty given by

$$\delta\nu^*_+ = \frac{\sqrt{(t^*_q + t^*_{\text{acc,-}} - t_q - t_{\text{acc,-}})^2\delta\nu^2_- + (t_d + t_{\text{acc,+}})^2\delta\nu^2_+ + \left(\frac{\delta\phi_{\text{start}}}{2\pi}\right)^2 + \left(\frac{\delta\phi^*_{\text{acc}}}{2\pi}\right)^2}}{t^*_d + t^*_{\text{acc,+}}}\ . \tag{4.11}$$

In a typical configuration for the start and reduced cyclotron accumulation phases, $t_q^* \approx t_q$, $t_{\text{acc,-}}^* \approx t_{\text{acc,-}} < 1/\nu_-$, and $t_{\text{acc,+}} \approx 0$. As such, the uncertainties in the calibrant frequencies are largely suppressed.

This equation allows for the determination of an unknown ion cyclotron frequency from just a single ν_+^* phase accumulation spot, with the caveat of reduced precision propagating from the calibrant ion's frequency uncertainties. This is an extremely powerful tool for the lowest rate isotopes of interest, where now half the number of ions are needed to complete the measurement. Furthermore, the calibrant frequencies for these cases will always be known to much higher precision than the ion of interest and contribute negligibly. A final list of assumptions made to arrive at this derivation are as follows:

- All ions start at trap center with net zero magnetron and reduced cyclotron radii
- Excitations for both species are resonant (within the excitation Fourier width)
- The calibrant is close in mass to the ion of interest such that $\nu_-^* = \nu_-$
- A complete quadrupole conversion takes place for both species
- The initial excitation phases are the same for both species

For a more detailed look into the systematic considerations for this mixed species technique, see Sec. 5.1. In general, no systematic shift to the calculated mass value was observed for a high-statistics study down to $\delta m/m \sim 10^{-8}$. For the intended use case of this technique, where only one spot may be generated, this precision is most likely more than sufficient.

4.4 Software and Analysis Toolsets

The final commissioning and development of the phase-imaging ion cyclotron resonance (PI-ICR) at LEBIT required significant software development for data visualization and analysis. Given the unique experimental configuration and requirements for the LEBIT setup, custom implementations of these tools were required. In the following sections, an introduction to the necessary

theory behind delay-line anode detectors is provided, along with an overview of the algorithm to determine an ion position. Additional software and analysis tool sets created to aid in the data acquisition and analysis for PI-ICR measurements are then presented. Significant inspiration for the analysis of PI-ICR data comes from the work of J. Karthein [85]. All software is maintained as open source under an MIT license.

4.4.1 Position Reconstruction from a Delay-line Anode

LEBIT utilizes a PI-ICR position sensitive detector system from RoentDek Handels GmbH which is comprised of an imaging micro-channel plate (MCP) detector in front of a delay-line anode detector [83, 86]. When an ion hits the MCP detector with sufficient energy, an electron avalanche is produced and is collected on the thin wires of a delay-line anode, as illustrated in Fig. 4.2. The difference in time for the electrical signal to propagate to either end of the anode determines the position on the anode where the signal originated. A fast time-to-digital converter (TDC) records these signal timestamps (after amplification and discrimination) for the MCP plate and each end of all delay line anodes. The delay-line setup in use at LEBIT quotes signal pulses shorter than 100 ps RMS (compared to the ~30 ns length of the delay line anode), which produces better than 45 μm RMS position resolution (compared to the 40 mm active diameter of the MCP).

The LEBIT data acquisition setup for PI-ICR records the raw timestamps from the TDC, vetoed by a narrow time-of-flight window following ejection from the trap to remove dark counts and environmental noise. The time window of interest is ~10 μs compared to the measurement cycle time of ~500 ms, eliminating the vast majority of dark counts. The TDC records the following timestamps for each ion hit event: the 'Start' signal when the ions are released from the trap, an 'MCP' signal when an ion hits the detector, and two timing signals for each delay-line anode.

Once the raw signals are digitized, an algorithm is required to sort out correlated signals for an ion hit and calculate the incident position on the detector. There are a number of nuances when determining if two timestamps are correlated, see [83]. The details for making these decisions are beyond the scope of this document, and the reader is directed to review the algorithm in the

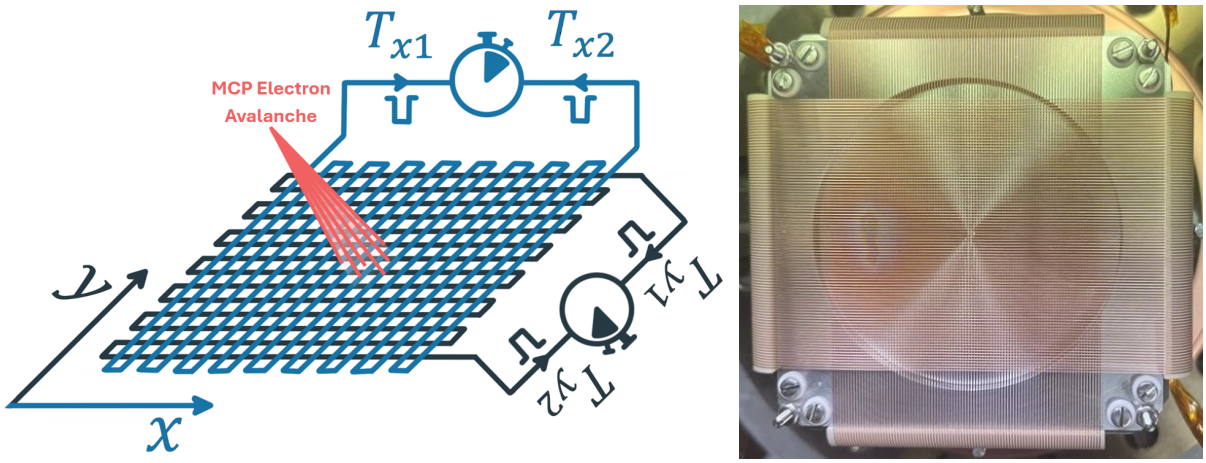

Figure 4.2 (Left) Illustration of a two-axis delay-line anode setup for accurate position determination. Electrons produced by the microchannel plate detector are picked-up on a wire, and the time difference for the signal to propagate to either end determines the position along the wire. Two independent wires allows for a two-dimensional position determination. (Right) The two-axis delay-line anode produced by RoentDek Handels GmbH in use at LEBIT for the phase imaging detector setup.

linked codebase for additional documentation. In essence, position information can only be easily recovered if two (or more) ion hits are separated in time by at least the delay line anode length (~30 ns). In the case of PI-ICR this is nearly always the case given the time-of-flight spread of the ions is ~5 μs.

With sufficiently large numbers of trapped ions (e.g. high contamination rates) the probability of two signals overlapping increases. Even with overlapping ion hits, it may still be possible to dis-entangle the two hits. The sum of each anode's signals falls within a narrow distribution as the delay-line has constant length, allowing for an additional gate to be applied. With this, the position of an ion hit can still be calculated even with missing timing signals. In principle, only three signals are needed: the MCP time, one of the X-anode times, and one of the Y-anode times. Knowing the distribution for the summed X-anode and Y-anode times allows one to determine the full position (with a slightly higher position uncertainty). Such events must be addressed on a case-by-base basis, but remain possible (if not necessary) for ultra-low rate experiments where every ion hit is critical.

4.4.2 Data Visualization

The code and a list of required dependencies to run this software are hosted publicly on the MSU GitLab server: `https://gitlab.msu.edu/camp1135/piicr_visualization_qt`. This software uses Python 3 as well as the PyQt6 library to support the graphical user interface (GUI). The GUI layout presents the most critical information relevant to PI-ICR measurements in addition to providing useful data filters and fits for quick analysis. The main page of the software is shown in Fig. 4.3 which provides a real-time visualization of the most critical information when running a PI-ICR mass measurement.

Of primary concern during an experimental campaign with PI-ICR is confirmation that the desired (molecular) ion is being trapped and measured. This relies on a fast analysis to quickly extract the frequencies of the trapped ions which can be compared to known values relative to a known calibration frequency. The GUI was developed to provide fast application of different gatings/filters to isolate the ions of interest. The time-of-flight (TOF) gate selects for ions with a specific travel time from the Penning trap to the MCP, and removes the bulk majority of counts resulting from dark counts and/or electronic noise. Spatial gates allow for the isolation of ions in a particular region of the MCP detector. Lastly, a filter can be applied to reject any measurements with too many ions concurrently trapped where space charge effects can distort the beam spot and induce frequency shifts [ref]. Once all desired gates are applied to the collected data, a separate datafile can be saved with the isolated ion positions for angle determination and analysis.

Preliminary data fitting to standard distributions is also provided, but is primarily used to align spots to a specific region of the detector. Additional tools are also provided to simplify the experiment setup. For example, a 'spot locator' window allows for the user to use the spot location and known frequencies for a calibrant ion to determine the expected angular locations for a given ion of interest allowing for an initial confirmation of whether or not an ion is present in the delivered beam. Furthermore, the user can also select expected contaminant species and adjust the trapping times to best separate the ion of interest from all other trapped ions. Direct timing information from the TDC can also be viewed to help identify problems with the detector electronics and data

acquisition during an experiment.

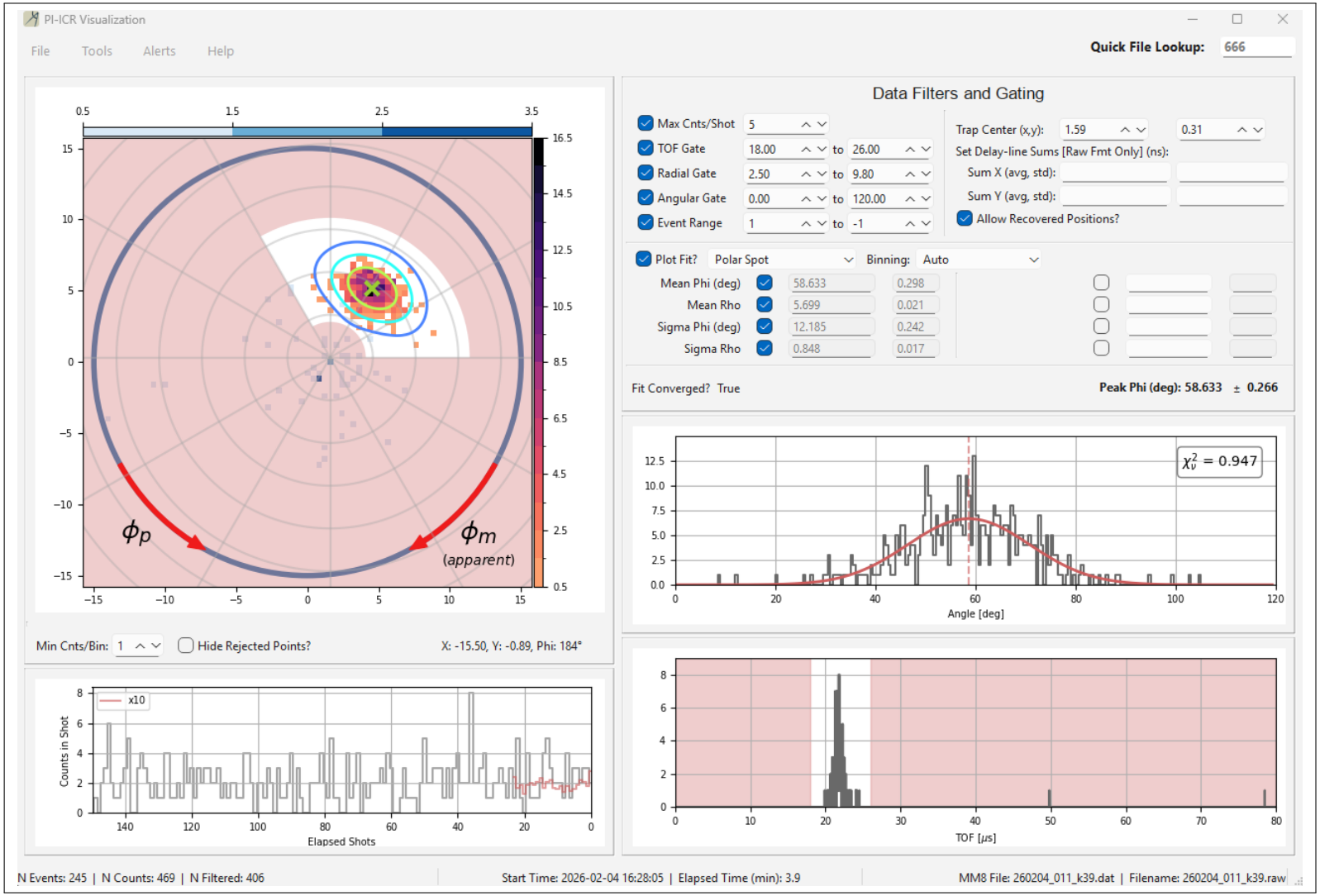

Figure 4.3 Custom software for Phase Imaging Ion Cyclotron Resonance (PI-ICR) Penning trap mass measurements. The main window shown here provides an overview of all important data, filtering of valid data from noise, and performing preliminary analysis. Real-time visualization during an experimental campaign provides necessary feedback to ensure proper configuration and progress.

4.4.3 Analysis Codes

A robust and quick analysis code is critical to the streamlined operation of PI-ICR during an experimental campaign. Thankfully, the data collected during a PI-ICR measurement can be extracted very fast and a preliminary analysis typically requires only a few fits to standard distributions. However, great care must be taken by the user when setting up the measurements to ensure a proper accounting of all relevant parameters. PI-ICR requires significant flexibility to manipulate ions and the measurement timings; the onus is placed on the experimenter to correctly configure the experiment around the present constraints. Herein lies the challenge of creating a 'universal' analysis code: each experiment often requires a unique approach. A framework which is easily portable to other experimental facilities is highly desirable, especially when aiming for reproducible results. The following discussion outlines the design principles at play towards these ends, as well as an overview of the codes capabilities.

When running an experiment, the timestamps for each MCP and delay-line anode are saved independently, and must be 'reconstructed' to determine the position of an ion hit. The raw timestamps provide the most fundamental data without bias or errors introduced from the reconstruction algorithm. However, the timestamp data is not human-readable and does not lend itself well to interpretation. Furthermore, when analyzing PI-ICR data often requires implementing various gates on the data (position, time-of-flight, coincident counts, etc.) which are themselves reliant on the reconstruction algorithm. Considering that the timestamp data is also saved independently from the system settings used to generate the datafile, the lack of coherence is not conducive to a repeatable and replicable analysis. Our proposed solution is to generate an 'analysis datafile' with two plain text sections: (1) a parse-able header containing all relevant system settings used to generate the datafile including all gatings/filters that have been applied, (2) all reconstructed data from the TDC.

The analysis software developed by the author for LEBIT reads in the saved reconstructed datafiles, fits the data to a standard distribution, and runs calculations to extract the ion frequencies using the equations presented in Sec. 4.3. The datafiles are each grouped into aggregate datasets.

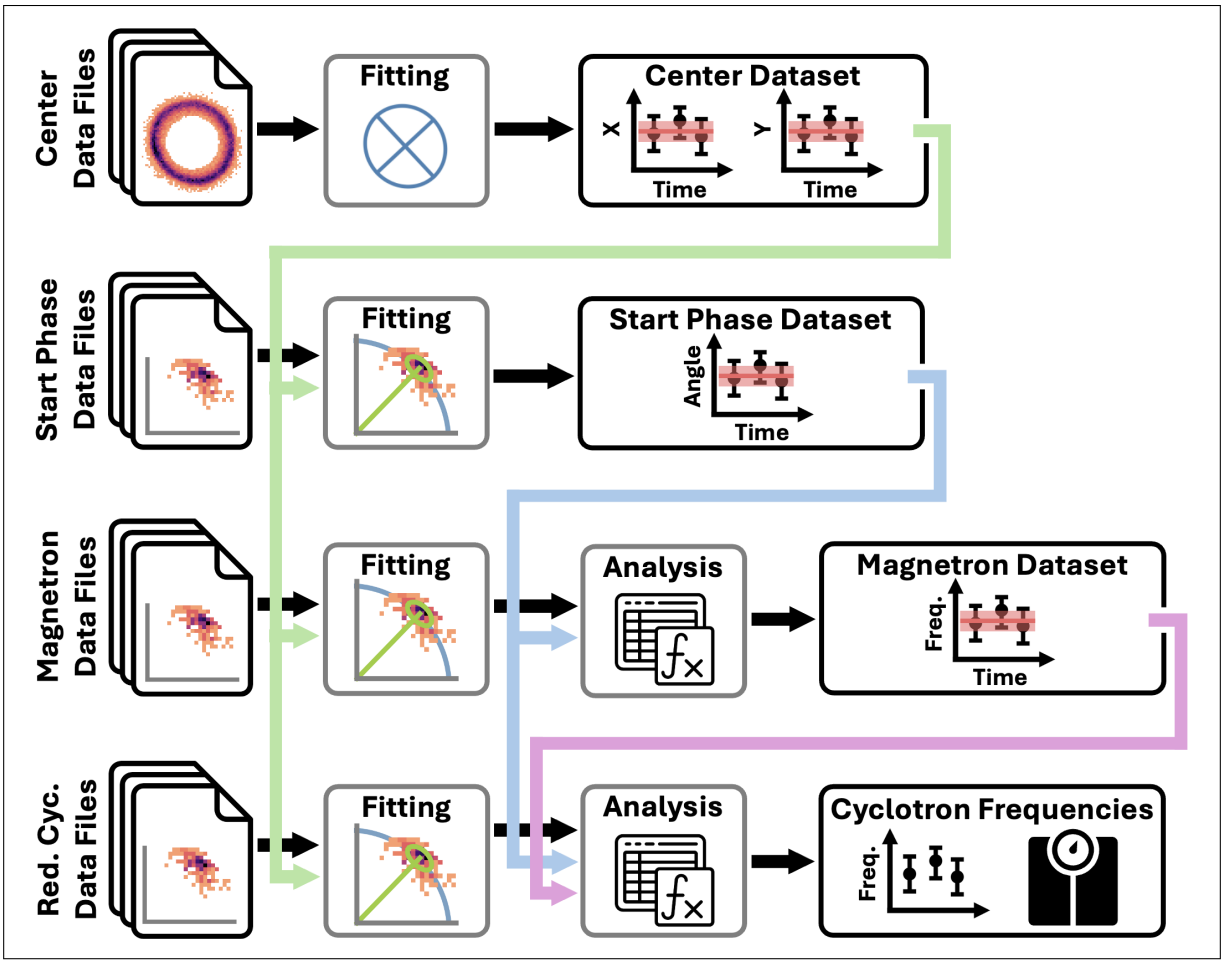

Figure 4.4 Workflow for the PI-ICR analysis code implemented at LEBIT. Steps are implemented from left-to-right, top-to-bottom. The modular analysis process can be easily modified and adapted to different configurations and measurement cycles.

For example, all datafiles used to determine the trap center are combined such that the extracted center can be interpolated in some fashion over the entire experiment time. This 'center dataset' can then be supplied to the 'start phase dataset' to determine the start phase angle and interpolate over time. The center and start phase datasets are then provided to the 'magnetron phase dataset' and 'reduced cyclotron phase dataset' to calculate the respective frequencies. The reduced cyclotron dataset also uses an interpolated magnetron frequency from the magnetron phase dataset for the phase correction in Eq. 4.6. A visual flowchart illustrating the connections is shown in Fig. 4.4

This workflow provides a straightforward procedure, and can be completed in quick fashion. The code is currently contained in a jupyter notebook for ease-of-use and provides a simple structure

for adaptation. Additional options can be imposed to correct for the non-circular projection of the ion motion, provide a custom angular uncertainty function (i.e. if the spot distribution is well known beforehand for low statistics measurements), among others. The software outputs a final calculated cyclotron frequency in a datafile format compatible for mass analysis with the SOMA (Simple Online Mass Analysis) software maintained by the LEBIT group.

4.5 Fitting Spot Distributions

Under ideal conditions, both the angular and radial distributions for an ion cloud following a PI-ICR measurement cycle are Gaussian. However, in some cases the angular distribution strays from a Gaussian–Chapter 5 provides additional details on some of these conditions. Accurately modeling the ion cloud distribution also provides a useful metric for evaluating and tuning the trapping fields. The following discussion provides an overview of of current techniques and applications to both simulated and experimental data.

4.5.1 Models for Spots in Polar Coordinates

When considering how to fit the ion distribution, the key consideration should be how one extracts the 'center' of the distribution and what exactly is meant by the center. In the presence of trapping field anharmonicities, the the phase evolution for the radial motions now includes a dependence on the radii of all eigenmotions. The consequence is a distorted angular/phase distribution of the ion spot, even under 'ideal' experimental conditions. This distortion is further exacerbated by the long trapping times and large radii critical to successful measurements which result in asymmetric angular shapes with a 'tailing' feature.

It can be shown that an ion cloud that starts at the trap center will retain its modal point. In other words, the mode of the distribution (point of highest density) preserves the unshifted frequency during while ions undergo free evolution. A number of statistical distributions exist which describe asymmetric distributions. Modeling the underlying distributions in polar coordinates is highly preferable, especially in the presence of strong tailing features. Figure 4.5 provides an overview of

five common asymmetric distributions applied to a simulated PI-ICR measurement in the presence of an anharmonic electric field, along with a standard Gaussian for comparison. It should be noted that the performance of each model depends on the extent of the tail distribution which is included for parameter optimization, subject to user discretion.

The Gaussian, Moyal and Crystal Ball distributions directly extract the distribution mode as a fitted parameter. The Exponentially Modified Gaussian and Skewed Student's-t distributions extract the mode by evaluating the maximum of the fitted distribution (e.g. with a trivial root finding algorithm). Note that by extracting it in this manner, the uncertainty in the mode is undefined. However, the uncertainty in the underlying Gaussian/t-distribution (which is directly fit) can be used as an estimate of the mode uncertainty to good approximation.

Applying these fits to experimental PI-ICR data in the presence of a poorly tuned trap (e.g. while in the process of trap tuning) suggests minimal preference to models where tailing is incorporated. Figure 4.6 provides an overview of the angular fits for one such experimental measurement.

4.5.2 Methods for Fitting Spot Distributions

An ideal approach to optimizing the distribution parameters describing a spot is with the negative log-likelihood (NLL) function in 2D Cartesian space:

$$\mathrm{NLL}(\theta) = -\sum_{i=1}^{N} \log P(y_i, x_i; \theta) \tag{4.12}$$

where P and θ are the probability distribution and its parameters, respectively. This function is often convex–meaning a unique global minima exists–and is beneficial for many gradient-based optimization techniques. When moving to polar coordinates, one must account for the fact that the area of a wedge is $r\Delta r\Delta\phi$, and the probability distribution must be normalized by the wedge area. Hence, the generalized NLL function for a polar distribution is

$$\mathrm{NLL}(\theta) = -\sum_{i=1}^{N} \log \left[\frac{P(r_i, \phi_i; \theta)}{r_i} \right]. \tag{4.13}$$

This function can be further simplified if the angular and radial distributions are independent, which is to be expected as only the angular spectrum is subject to distortion from trap anharmonic-

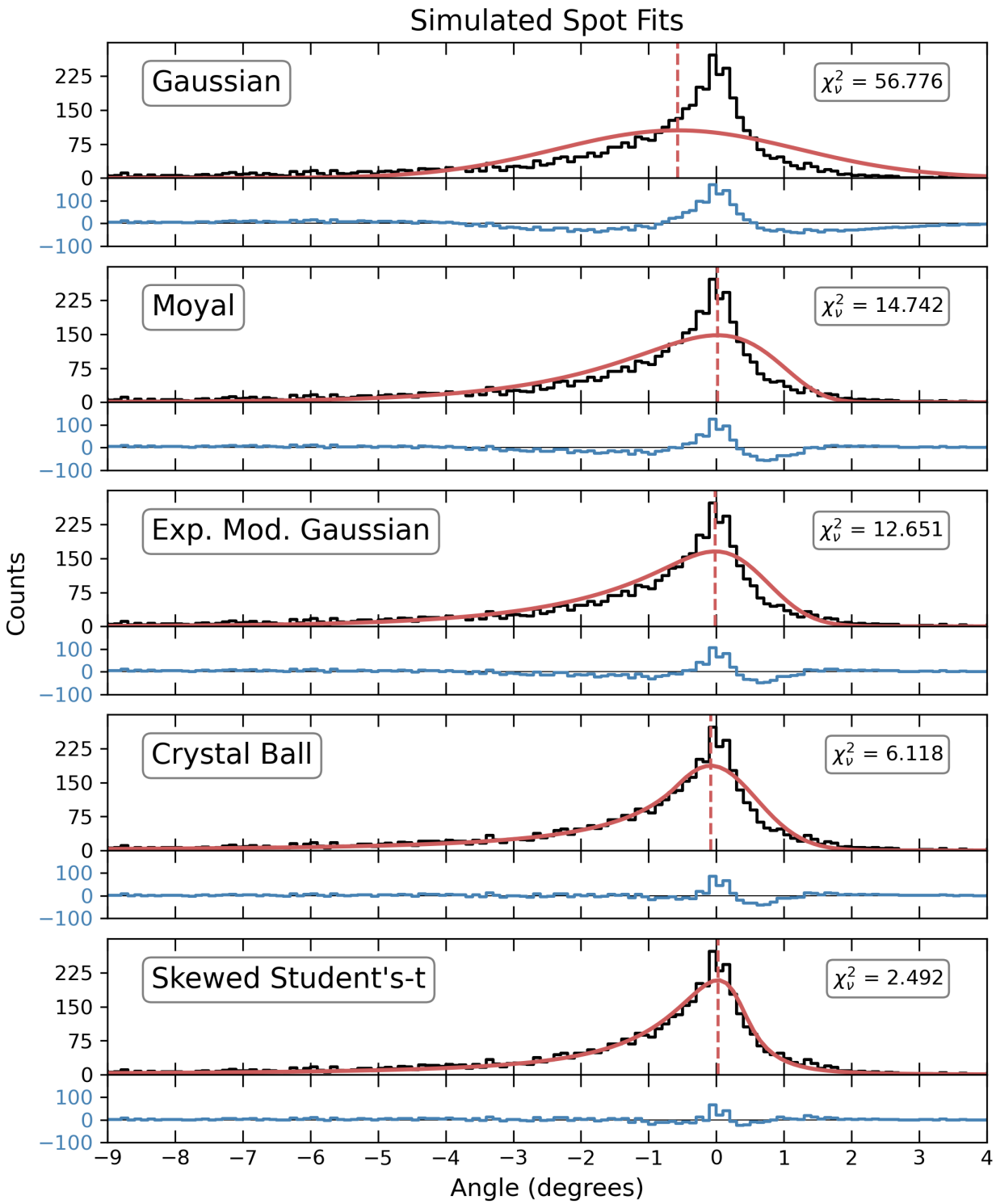

Figure 4.5 Comparison of statistical distributions for modeling an asymmetric angular distribution for a simulated PI-ICR measurement in the presence of an electric field anharmonicity. The mode of each fitted distribution is shown by a vertical dashed line. Reduced-χ^2 values for each fit are also shown. Residuals for each fit are shown underneath as the blue histogram.

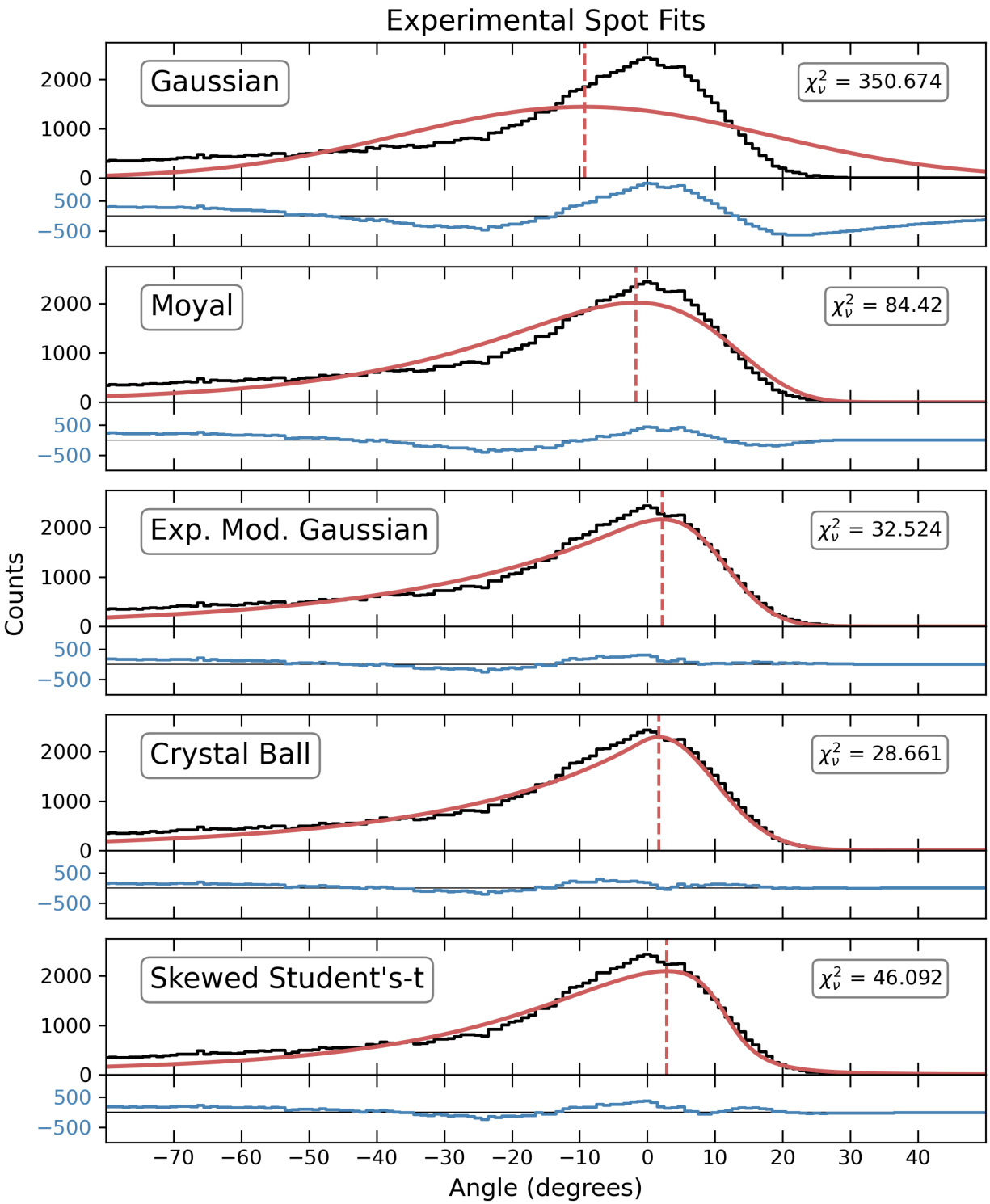

Figure 4.6 Comparison of statistical distributions for modeling an experimental PI-ICR measurement of $^{39}K^{+}$ where an asymmetric angular distribution is observed. The mode of each fitted distribution is shown by a vertical dashed line. Reduced-χ^2 values for each fit are also shown. Residuals for each fit are shown underneath as the blue histogram.

ities. The radial distribution is unaffected by the dipole excitation, and preserved for a complete quadrupole conversion. In this case, the probability can be written as $P(r_i, \phi_i) = P(r_i)P(\phi_i)$ and the NLL function is given by

$$\mathrm{NLL}(\theta_r, \theta_\phi) = -\sum_{i=1}^{N} \log P(r_i; \theta_r) + \log P(\phi_i; \theta_\phi) - \log r_i \tag{4.14}$$

where θ_r, θ_ϕ are the parameters describing the radial and angular distributions respectively.

Optimizing the fit parameters under this formalism is straightforward, and perhaps the most rigorous option. However, an implicit assumption is that every point included in the dataset is meaningful to describe the underlying distribution. It is well known that PI-ICR measurements are susceptible to noise from contaminant species, dark counts, etc. which have the potential to greatly skew the optimized parameters. The impact of noise counts can be mitigated by binning the data over a characteristic width and assigning an uncertainty/'importance' factor related to the bin density. This approach requires a sufficiently large dataset (often $\gtrsim$200 counts) to adequately capture the relevant features of the distribution. While not directly applicable to low-statistics measurements in the case of many rare isotopes, it proves a useful tool for calibration and tuning measurements.

When considering the binned optimization problem, additional considerations are required. Accurate fitting relies on a dense sampling of bins, each with a large number of counts. Determining an 'optimal' bin width to capture relevant features of the distribution can be determined with the Freeman-Diaconis rule [87]. This approximately minimizes the integral of the squared difference between the histogram and the density of the theoretical probability distribution. The interquartile range (IQR) is straight-forward to calculate, and is used to determine the optimal bin width:

$$h = 2\frac{\mathrm{IQR}(x)}{\sqrt[3]{n}} \tag{4.15}$$

where n is the number of observations in the sample x.

The negative log-likelihood function must be adjusted to account both for the binning and any desired weighting function for a given bin. Specifically, Poisson statistics can be used to evaluate

the probability of observing k counts in a bin when λ are expected from the distribution:

$$\mathcal{P}(k|\lambda) = \frac{\lambda^k e^{-\lambda}}{k!}. \tag{4.16}$$

The negative log-likelihood function can then be written as

$$\mathrm{NLL}(\theta) = -\sum_{j=1}^{n} \log \mathcal{P}(k_j|\lambda_j;\theta) \approx \sum_{j=1}^{n} \lambda_j - k_j \log \lambda_j \tag{4.17}$$

where j, n denote bin index and number of bins. Note that the $k!$ term is neglected as it does not depend on the model parameters. Since the data is known to contain (often sparse) noise, a weighted NLL function can be utilized to prioritize the optimal parameters for bins with higher statistics. A simple weighting function is $\sqrt{k}$, which approximates the 'counting' uncertainty for large k. A final weighted version of the binned NLL is then given as

$$\mathrm{NLL}(\theta) \approx \sum_{j=1}^{n} \sqrt{k_j}\left[\lambda_j - k_j \log \lambda_j\right] \tag{4.18}$$

where λ_j can be expressed in terms of the probability distribution by

$$\lambda_j = N \cdot h \cdot P(r_j, \phi_j; \theta) \tag{4.19}$$

where N is the total number of counts and P is the model probability distribution.

4.6 Clustering Techniques

Clustering algorithms provide a structured approach to including/excluding points within a 'spot'. While their use in PI-ICR measurements has largely fallen to the wayside, they are still useful for quick analysis, especially in the presence of noise. One current downside to most modern clustering algorithms are finicky hyperparameters which may need to be tuned for a given dataset, see [88, 89] for reviews. The need for continual intervention takes away the usefulness as an unbiased discriminator. The following section discusses a novel clustering approach uniquely tailored to PI-ICR datasets to provide a consistent clustering approach.

A few standard clustering algorithms of relevance to PI-ICR data include k-means [90], DBSCAN [91], and OPTICS [92] (among many others). While broadly useful, we can take advantage

of the structured nature of PI-ICR data to dramatically improve the predictive power. In particular, the data of interest is spatially contained within the radius of the MCP/delay-line detector. Furthermore, the location and size of the clusters relative to the detector dimension is relatively constant. These constraints allow for a spatial discretization of the position data into finite bins, scaled by the detector size. Data which can be discretized in this manner is particularly suited for machine learning techniques, which offer powerful and tailored approaches to classify and/or perform regressions.

There are a plethora of machine learning algorithms available such as k-nearest neighbors [93], naive Bayes [94], among many others. More recently, neural networks allow for fast prediction of datasets with a large number of inputs with high complexity. In the case of the discretized PI-ICR data, the domain is segmented into 2500 pixels, which would pose a significant challenge to the former machine learning techniques. Neural networks are well suited to large-domain datasets, and also have the benefit of natively prescribing a probabilistic value to the model output. The general idea for clustering PI-ICR data with a neutral network is the following:

1. Discretize the MCP position data to a finite grid
2. Determine a normalized density for each grid point
3. Feed the resulting 'density map' into a neural network
4. Output the probability of each grid point existing in a spot cluster
5. Apply smoothing/thresholds to the 'cluster probability map'
6. Collect all MCP hits that exist within the cluster map

The clustering neural network was implemented in python with the Tensorflow [95] and Keras [96] libraries. For simpler implementation, the 2D discretized density map is unwrapped to an array of size (50×50). The model input is of size 2500 with a rectified linear unit (ReLU) activation function. A shallow network structure was found to provide suitable predictive power, and only a single internal dropout layer is used to prevent overfitting. The model output is of size 2500 with a

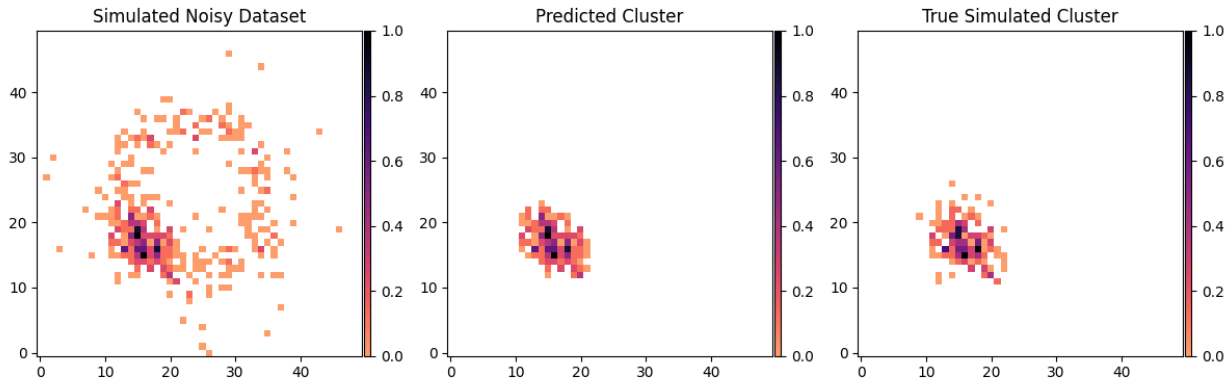

Figure 4.7 (Left) Simulated PI-ICR spot with characteristic noise at the excited radius in addition to uniform random noise. (Center) Positions determined to exist in a cluster by a neural network trained on simulated datasets. (Right) Simulated PI-ICR spot without additional noise, i.e. the 'true' cluster. Both axes represent the discretized bin number, and the colorbar represents the normalized bin density.

sigmoid activation function, which is ideal for the binary classification problem of a pixel existing in a cluster or not. The model was trained with a binary cross-entropy loss function in combination with the 'Adam' optimizer [97]. The model was then trained over ~50000 training datasets which were produced from simulated clusters with characteristic noise patterns. The model was supplied a validation set of ~10000 datasets during training. After approx. 10 epochs with a batch size of 64, the model achieved sufficient accuracy. Figure 4.7 shows a comparison of the model input, the positions classified as existing in a cluster, and the 'true' cluster from simulated data. Overall, the model performs quite well at excluding noise and recovering the original spot information for simulated datasets.

With the model's success on simulated datasets, it can be applied to experimental datasets with confidence. Figure 4.8 shows an example application of the trained neural network on an experimental dataset. Overall, the model appears to well capture the cluster and reject the noise. However, care also needs to be taken to avoid overfitting where the model rejects counts which result from meaningful ions. In principle this consideration remains relevant regardless of whether clustering is performed on the dataset.

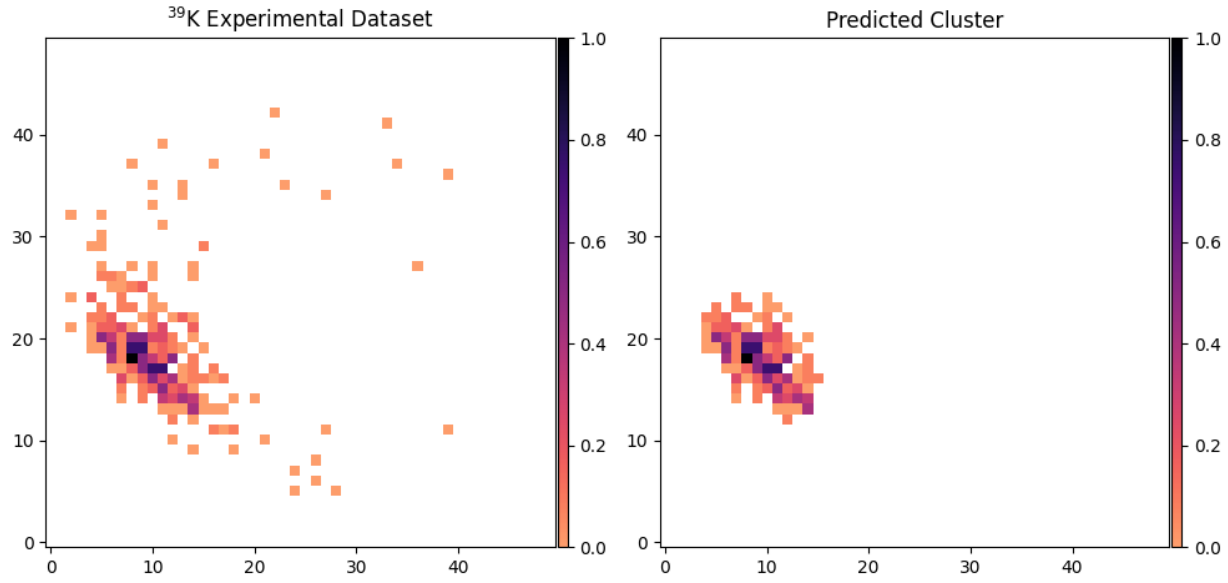

Figure 4.8 (Left) Experimental PI-ICR data of $^{39}K^{+}$ trapped for 200 ms while undergoing reduced cyclotron motion in the LEBIT 9.4 T magnet. (Right) Predicted cluster by the neural network. Both axes represent the discretized bin number, and the colorbar represents the normalized bin density.

CHAPTER 5

SYSTEMATIC STUDIES OF PI-ICR

Systematic studies in $\bar{R}$ have been well studied for Penning trap mass spectrometry, specifically for TOF-ICR. Some of the more prominent systematics arise from magnetic field inhomogeneities, deviations in the axial alignment of the Penning trap with the magnetic field, and distorted electrostatic trapping potentials [42]. A majority of these effects are known to scale linearly with the difference in the mass of the calibrant ion and ion of interest. For example, TOF-ICR measurements are known to add an uncertainty of $\delta\bar{R} \approx 2 \times 10^{-10}$ per mass unit difference between the calibrant and ion of interest species [98]. A common systematic due to space charge effects also becomes prominent when $\gtrapprox$ 5 ions are simultaneously trapped [42] which are typically mitigated through ion cleaning (see Sec. 2.3). Non-linear temporal magnetic field instabilities have also been shown to contribute no more than 1×10^{-9} [99] to $\bar{R}$ over the course of one hour.

With the increased sensitivity of PI-ICR, a number of additional systematic effects are known to exist and remain under continued study. Extensive studies have been completed at other Penning trap facilities [67, 72, 85, 100–102] which highlight key considerations as well as system-dependent effects. LEBIT continues to probe the impact of these known systematics among others, the majority of which are dominated by the electrostatic trapping field harmonicity, alignment of the Penning trap to the magnetic field, and space charge effects [103]. This chapter provides an overview of systematic studies undertaken at LEBIT as well as the expected impact on achievable mass precision.

5.1 Mixed Species Measurement

As discussed in Sec. 4.3.4, there are many rare isotope measurements which are primarily limited by the delivered rate. The 'mixed' species scheme for PI-ICR reduces the required number of ion counts by half as it uses the start phase of the reference species for the accumulated phase of the ion of interest. As this has not been bench-marked before, a careful study of the new technique is required. Specifically, we are interested in quantifying any systematic shift to the measured mass

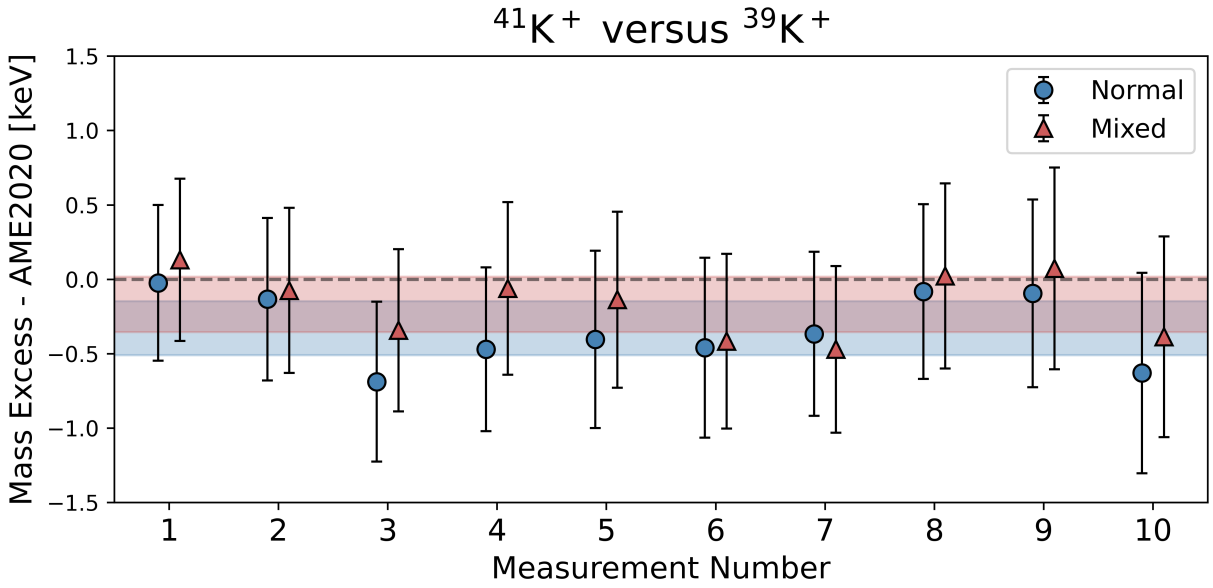

Figure 5.1 Comparison of ^{41}K mass excess values determined with PI-ICR using ^{39}K as the reference species (2 amu away). The measurements indicated by blue circles calculated the ^{41}K frequencies in the usual manner. The red triangles indicate ^{41}K frequencies where the ^{39}K start phase was used for the mixed-species method.

that may result from this particular configuration.

It is well established in Penning trap mass spectrometry that a mass-dependent frequency shift will be observed when the ion of interest and reference species are not isobaric [98]. This effect will persist through the mixed measurement as well, but may also compound as the reference species frequency is used to calculate the ion of interest frequency. In such a case, we would expect any additional systematic effect to become more pronounced with larger mass differences between the two species. From a practical standpoint, it is extremely unlikely that a suitable reference species cannot be found within 2 amu, so we limit our studies there for the time being.

Figure 5.1 shows an example of the mixed phase mass measurement for a 2 amu mass difference compared to the standard PI-ICR measurement cycle. No additional systematic effect was observed down to the $\delta m/m \sim 10^{-8}$ level in this particular test. Additional studies are still needed to determine the true systematic level of this approach. However, as the main use case of the mixed measurement scheme is for the lowest-rate experiments, achieving the highest precision is not the primary goal, and precisions $\sim 10^{-8}$ are more than sufficient for nuclear astrophysics and nuclear

structure studies.

5.2 Non-Uniform Phase Projections

An ideal Penning trap has the electrode axis perfectly aligned with the magnetic field axis. However, it has been previously shown that a slight misalignment exists for the LEBIT 9.4 T spectrometer as presented in [61]. At this time, detailed simulations with SIMION revealed that both translations and/or axis rotations result in two important features: (1) a disagreement in the calculated trap center between ions with a radius $\rho = 0$ and $\rho > 0$, and (2) the projected ion motion does not follow the expected circular path. Figure 5.2 shows the observed ion paths for $\rho = 0$ and $\rho > 0$ at LEBIT, where a disagreement in the fitted centers highlights the presence of a field misalignment.

At the end of the PI-ICR measurement cycle, the ions have pure circular motion at the magnetron frequency. Upon ejection from the trap and acceleration to the MCP detector, the ion motion evolves according to the magnetic field gradient and electrostatic field. With the slow magnetron frequency

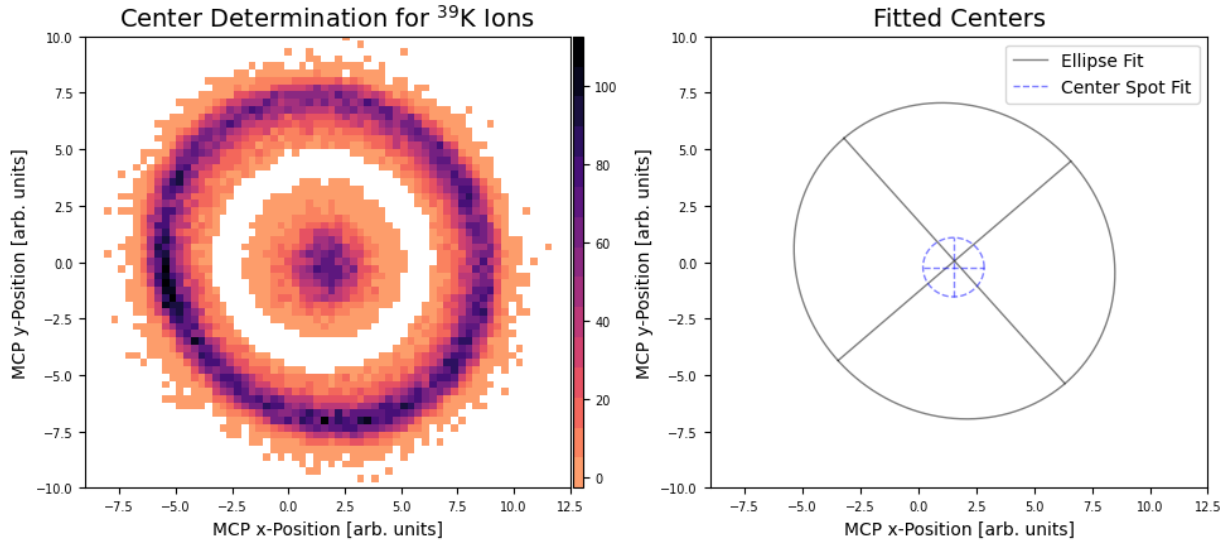

Figure 5.2 (Left) Superimposed datasets showing two methods for determining trap center: projection of the circular motion via scanning over one magnetron period, and a dataset with no excitations applied (aka 'center spot'). (Right) Resulting ellipse fit with a center at x=1.56(1) and y=0.05(1) compared to a 2D Gaussian fit to the center spot with a center at x=1.52(2) and y=-0.23(2). The discrepancy between center measurements far exceeds the fit uncertainty.

(~2 kHz) and the fast time-of-flight (~20 μs), the ions largely follow a straight path to the MCP, with the radius magnified according to the magnetic field gradient. As such, the presence of a field misalignment will reveal itself through non-uniform and non-linear magnification.

This systematic effect can be mitigated through careful alignment of all PI-ICR spots to a narrow angular region of the MCP, using the procedure outlined in Sec. 4.3.3 for example. Over a sufficiently narrow angular window, a circle remains a good approximation and the determined angles are reliable. However, there are several cases where it is not possible or practical to align all spots together. For online rare isotope measurements with very-low rates, often there is not sufficient beam time to iteratively adjust the trap timings. In the case of isotopes with isomers, both will be simultaneously trapped and will appear at different angles relative to their mass separation. In the remaining discussion, a procedure for calibrating the impact of the field misalignment on the detected spot angles is provided, and validations for experimental data is shown. The method described here was developed in parallel to results presented in Ref. [101] and extends it to provide a sensitive calibration.

Calibration can take advantage of the PI-ICR cycle, where ions undergo pure magnetron motion just prior to ejection/detection. This slow motion can be precisely scanned via the magnetron phase accumulation time, allowing for an accurate comparison between the observed detector angle and the expected trap phase $\theta = \nu_- t_{\text{acc,-}}$. As PI-ICR is concerned with the separation between two angles, only a relative trap phase is important: the trap phase can be defined relative to any phase measurement observed at the detector. A natural choice is to select an observed phase $\phi \approx 0^\circ$ with $t_{\text{acc,+}} = 0$ and $t^0_{\text{acc,-}}$. Then, for each scanned magnetron accumulation time $t^i_{\text{acc,-}}$, the discrepancy between the observed phase ϕ^i and the expected trap phase θ^i is given by

$$\Delta^i = \phi^i - \theta^i \tag{5.1}$$

$$= \phi^i - \phi^0 + 2\pi\nu_- \left(t^i_{\text{acc,-}} - t^0_{\text{acc,-}}\right) \tag{5.2}$$

where d_- is the magnetron phase accumulation sign. The magnetron frequency can be determined to high precision through TOF-ICR, or by careful alignment of the spots in PI-ICR. Figure 5.3 shows an example calibration for $^{39}K^+$ ions at LEBIT.

Given the periodic nature of the calibration, a truncated Fourier series is ideal to model the correction:

$$\Delta(\phi) = \phi + a_0 + \sum_{k=1}^{K} \left(a_k \cos(k\phi) + b_k \sin(k\phi)\right) \tag{5.3}$$

where the Fourier coefficients a_k, b_k are optimized with a weighted least-squares approach to account for uncertainties in the observed ϕ. Finally, a calibrated phase measurement can be determined by evaluating the truncated Fourier series at an observed phase:

$$\theta(\phi) = \phi - \Delta(\phi). \tag{5.4}$$

The truncation of the Fourier series can be set to adequately capture the correction function shape, while taking care to avoid overfitting the data.

Naturally, the severity of this systematic shift depends on the experimental setup and the extent of the beam and magnetic field misalignment. As PI-ICR measurements involve the relative phase separation between reference and phase accumulation spots, the correction to the observed frequency will be the difference of the correction at the two observed angles:

$$\|\Delta\nu\| = \frac{\|\Delta(\phi_{\text{acc}}) - \Delta(\phi_0)\|}{2\pi t_{\text{acc}}}. \tag{5.5}$$

Clearly, this shift dominates at low accumulation times. From Fig. 5.3, the worst-case spot alignment could lead to an angular shift of $\approx 10^{\circ}$. For reasonable accumulation times of ~100 ms, this would amount to a systematic mass shift of $\delta\nu/\nu \sim 10^{-7}$ for typical masses at LEBIT. Figure 5.4 shows the impact of the phase calibration for experimental data. The dramatic shifts in the uncorrected frequencies highlight the relevance of this systematic when spots may not be well aligned, as might be expected for low-rate exotic rare isotopes.

For experiments with very-low rates of rare isotopes, a careful alignment of the PI-ICR spots is simply not possible. A careful accounting of the phase correction with the above method becomes critical for a successful measurement. For these measurements, the best practice would be to use an isobaric species as a frequency reference and to generate the phase calibration curve (which requires very high statistics). However, there have been multiple cases at LEBIT where a suitable

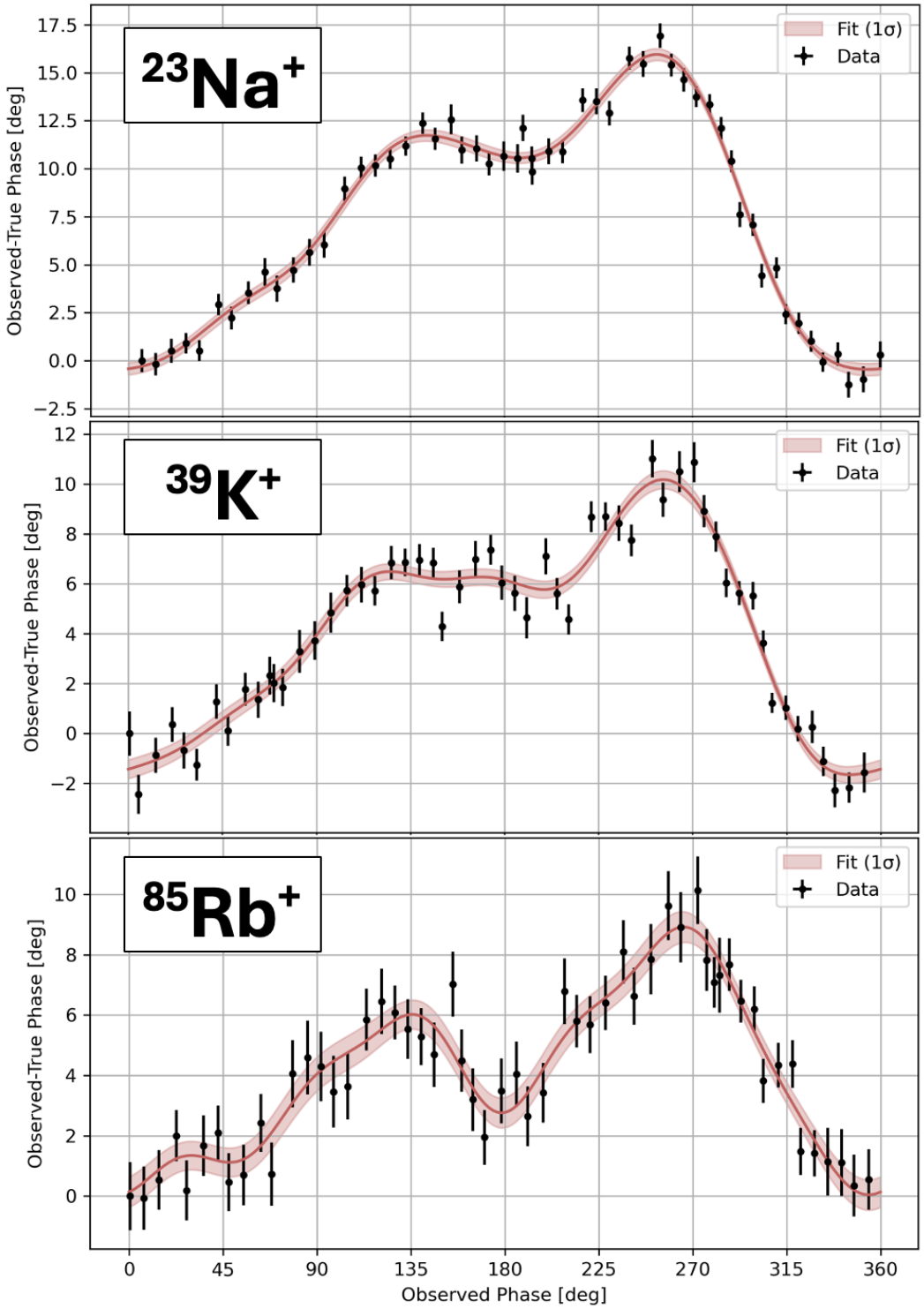

Figure 5.3 Calibrated phase differences between the observed angle on the MCP detector and the 'trap angle' for $^{23}Na^+$, $^{39}K^+$ and $^{85}Rb^+$ ions. A truncated Fourier series (K=6) fit to the phase correction is also shown.

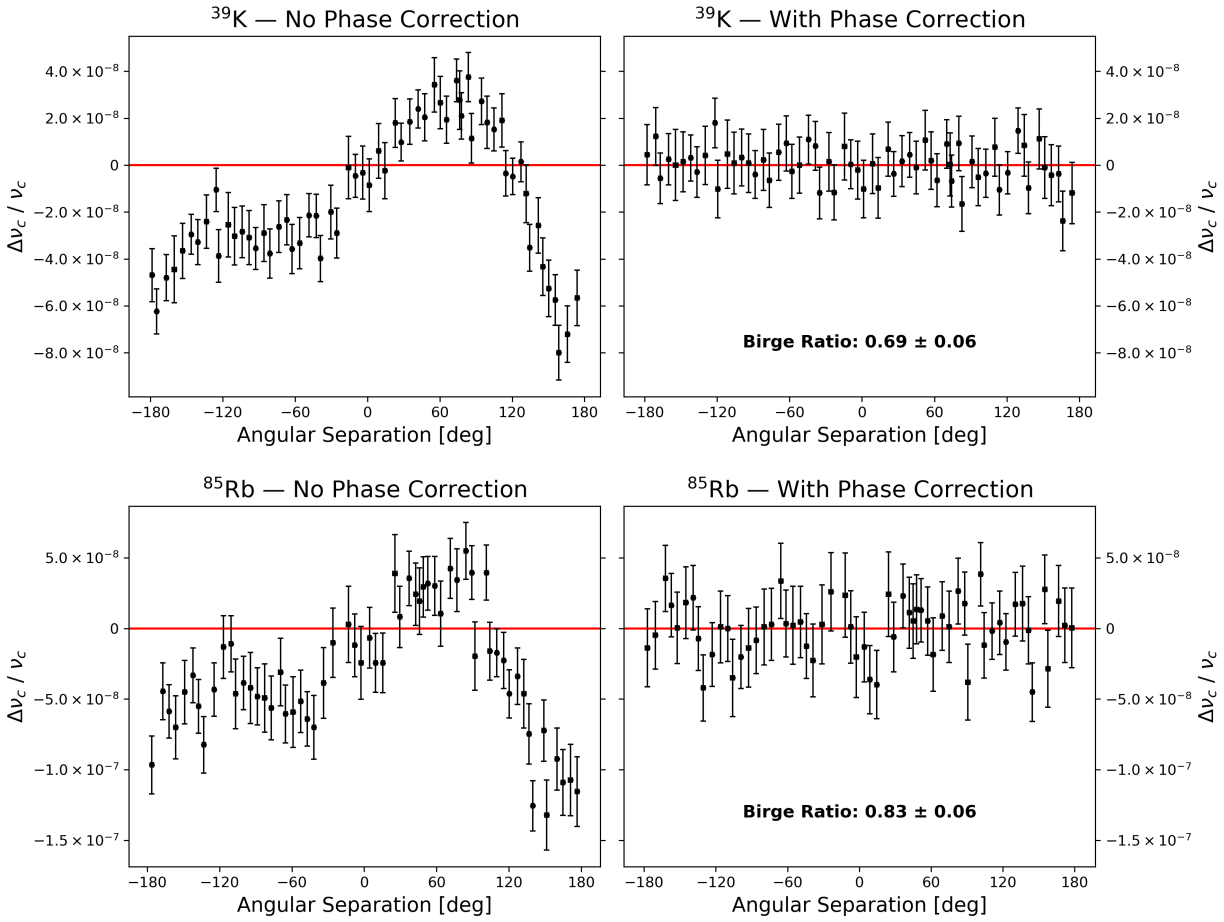

Figure 5.4 Comparison of experimental $^{39}K^+$ and $^{85}Rb^+$ cyclotron frequency measurements with and without the calibrated phase correction applied. The y-axis shows the difference between the measured frequency and a high-precision TOF-ICR measurement, normalized by the TOF-ICR frequency. A 100 ms reduced cyclotron spot was sampled over the full detector space by scanning the magnetron phase accumulation time over one magnetron period. The relative frequency shifts for the uncorrected case far exceed the frequency measurement uncertainty.

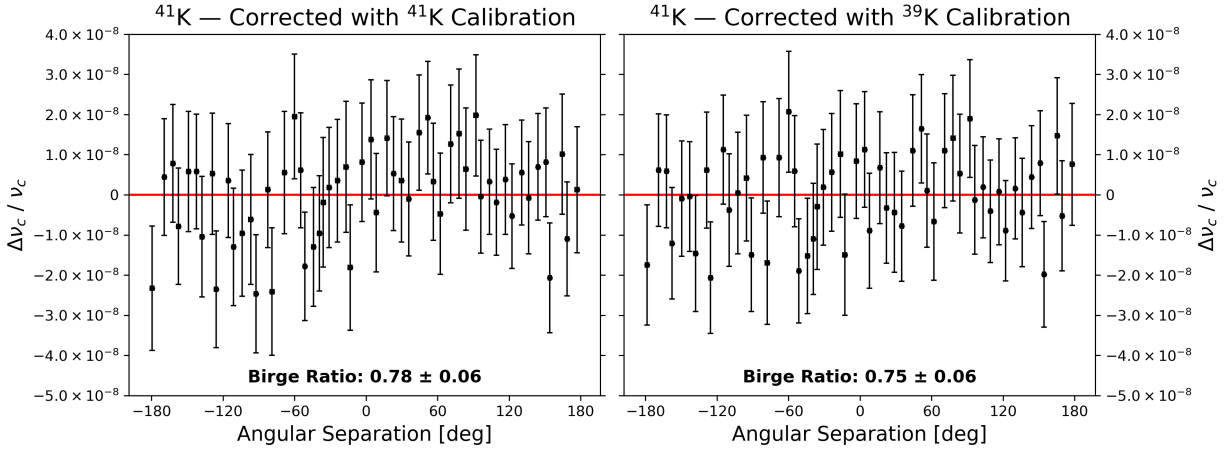

Figure 5.5 Comparison of the $^{41}K^+$ cyclotron frequencies determined with a $^{41}K^+$ phase calibration versus a $^{39}K^+$ calibration.

isobaric reference could not be identified, and a near-by mass was used instead. Simulations of the phase distortion in SIMION suggest that the effect is largely driven by the potential gradient from the trap to the MCP. The mass/charge of the ions can also play a role, where LEBIT has seen that different potential gradients are required for broad mass regions to maintain a reasonable magnification of the ion motion.

To test the sensitivity of the phase calibration to ion mass, a dataset of $^{41}K^+$ ions was collected and the $^{39}K^+$ phase calibration was used to correct the observed angles. The results of this test in Fig. 5.5 shows that the phase calibration dataset is largely mass-independent for a given potential gradient between trap and MCP detector. As such, high-rate near-by masses can be used to generate a calibration dataset for experiments with low-rate rare isotopes.

The phase calibration can also serve as a sensitive probe of the field misalignment. Through small adjustments to the beam axis, minimizing the magnitude of the correction over all angles serves to optimize the alignment. Given the heightened resolution of PI-ICR, the axis alignment becomes significantly more important than for the TOF-ICR technique. For the highest precision measurements this remains a vital correction to minimize systematic effects.

5.3 Trap Tuning Systematics

A precise tuning of the Penning trap correction ring and correction tube electrodes are essential to producing the required quadrupolar trapping field of the Penning trap given the finite electrode geometry. A theoretical description for the trapping potential tuning is provided and its impact on ion motion relevant to PI-ICR is discussed first. Then an experimental procedure for characterizing and then minimizing the trapping potential anharmonicity is outlined.

5.3.1 Theoretical Background for Trap Harmonicity

The trapping potential of Eq. 2.3 is cylindrically symmetric about the $z = 0$ plane and can be expressed as an expansion of the Legendre polynomials P_{2n}:

$$V = \sum_{n=0} C_{2n} \frac{V_0}{2d^{2n}} \rho^{2n} P_{2n}(\cos\theta) \tag{5.6}$$

where C_{2n} is the pole scaling factor and $d^2 = {}^1\!/_4(2z_0^2 + r_0^2)$ is the characteristic dimension parameter for the Penning trap. For the ideal quadrupolar field ($n = 1$), the scaling factor $C_2 = 1$. Imperfections to the field are encoded in the higher order terms such as the octuple moment ($n = 2$), etc.

The Penning trap correction ring and tube electrodes modify the trapping field to approximate a quadrupole, such that $C_{2n} \approx 0$ for $n > 1$. Following the procedure outlined in [104], the eigenfrequencies are shifted according to the strength of the $n = 2$ and $n = 3$ correction under first-order perturbative calculations:

$$\begin{aligned}\Delta\omega_\pm \approx \pm\frac{\omega_+\omega_-}{\omega_+ - \omega_-}\Bigg[&\frac{C_4}{C_2}\frac{3}{d^2}\left(\rho_\mp^2 + \frac{1}{2}\rho_\pm^2 - z^2\right) + \\ &\frac{C_6}{C_2}\frac{45}{2d^4}\left(-\frac{1}{4}z^4 + \frac{1}{2}\rho_\pm^2 z^2 + \rho_\mp^2 z^2 - \frac{1}{12}\rho_\pm^4 - \frac{1}{2}\rho_\mp^2\rho_\pm^2 - \frac{1}{4}\rho_\mp^4\right) + \ldots\Bigg]\end{aligned} \tag{5.7}$$

where $\rho_\pm$, z are the amplitudes of the radial and axial modes respectively. Simulations with the LEBIT Penning trap geometry presented in [105] suggest an optimally tuned trap field will have C_{2n}'s on the order of those shown in Table 5.1.

Parameter	Value
C_2	1.00187
C_4	0.00207
C_6	-0.00442
C_8	0.00294

Table 5.1 Calculated C_{2n} values for the LEBIT 9.4 T Penning trap geometry determined from SIMION studies, originally presented in [105].

5.3.2 Probing Trap Tune Quality with PI-ICR

The expected frequency shifts will be largely mass independent as the 'reduced frequency' prefactor in Eq. 5.7 is determined primarily by the ω_- frequency as $\omega_+ \gg \omega_-$. As such, the radii of motion will determine the extent of the frequency shifts. During a PI-ICR measurement cycle these radii are constantly evolving during both the initial dipole excitation and quadrupole conversion pulses. Understanding the impact of these frequency shifts on the final phase distribution of the ions is non-trivial. A numerical solver for the ion motion was developed to integrate the frequency shift effects over a PI-ICR measurement cycle to evaluate the expected impact. Figure 5.6 provides a comparison of the simulated spots in the presence of an octupole anharmonicity as well as experimental observations showing a similar behavior.

As PI-ICR probes ion motion at large trapping radii, where frequency shifts are more pronounced, a precise tuning of the trapping potential is critical. Procedures for optimizing the correction ring and tube values have been well-studied with the TOF-ICR measurement technique, such as Refs. [106, 107]. However, studies at LEBIT have shown that the heightened sensitivities of PI-ICR require a more precise tuning, though the value determined with TOF-ICR provides a good initial point. Figure 5.7 provides an illustration of the trap tuning with TOF-ICR at LEBIT using the method of Ref. [106]. Clearly there is a wide range of potential solutions and a refined approach is required to suit the precision of PI-ICR. The following discussion outlines a novel approach to leverage the sensitivity of PI-ICR to further optimize the trap tune quality.

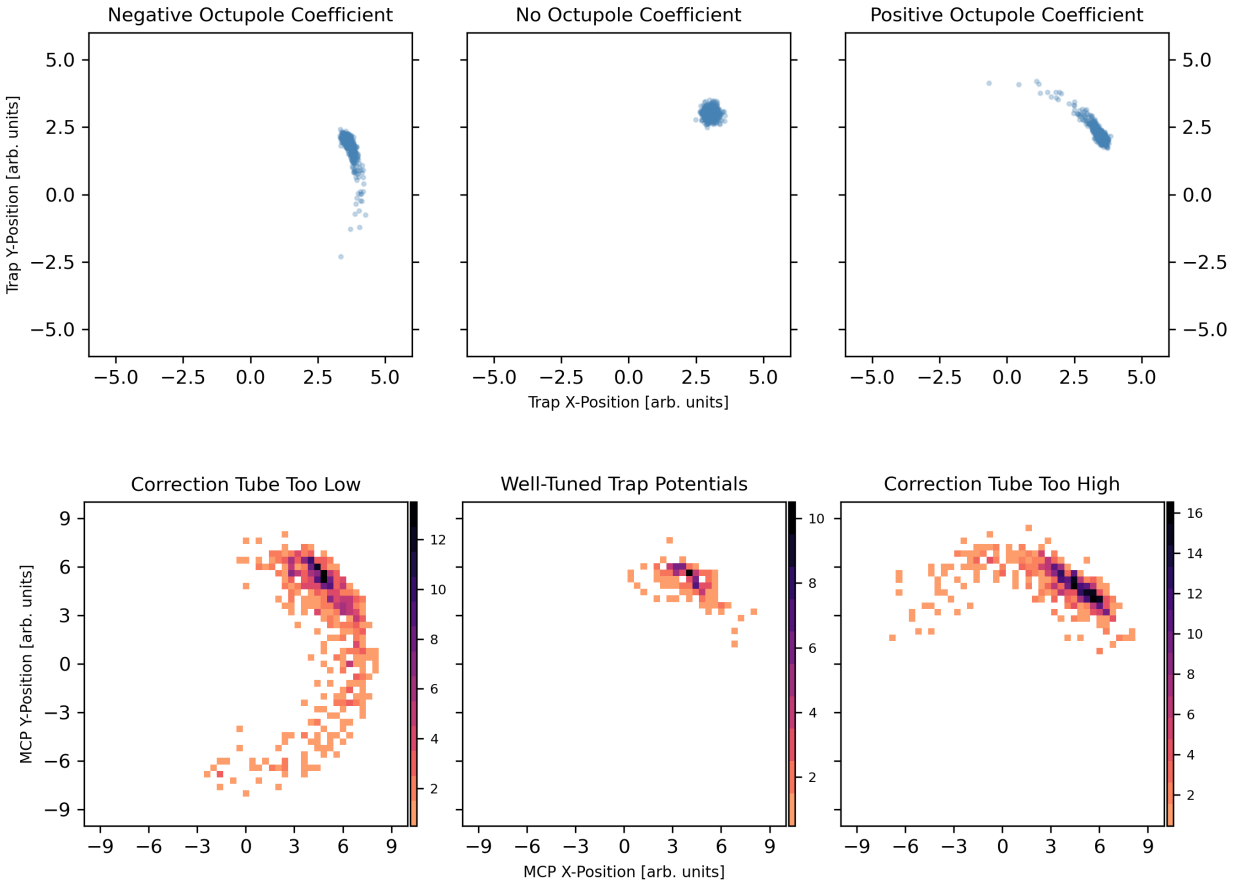

Figure 5.6 (Top Row) Comparison of simulated PI-ICR spots in the presence of a trapping potential with an octupole contribution. Spots exhibit a 'tailing' feature whose direction depends on the sign of the octupole coefficient. (Bottom Row) Comparison of experimental $^{39}K^{+}$ PI-ICR spots where the correction tube voltage was adjusted to induce anharmonicities into the trapping potential. Similar tailing features occur as in the simulated data.

5.3.3 Trap Tuning Procedure with PI-ICR

The complexity of the PI-ICR measurement cycle in Sec. 4.3 coupled with the frequency shifts of Eq. 5.7 make it challenging to evaluate the trap tune independently of contributions from the RF excitations. To best decouple these effects, we alter the PI-ICR measurement cycle to the following:

- Inject ions into the trap at an initial magnetron radius using Lorentz steerer. Larger radii induce a bigger frequency shift for poorly tuned potentials.
- Allow the ions to evolve at the magnetron frequency. Longer trapping times resolve smaller frequency shifts from poorly tuned potentials.

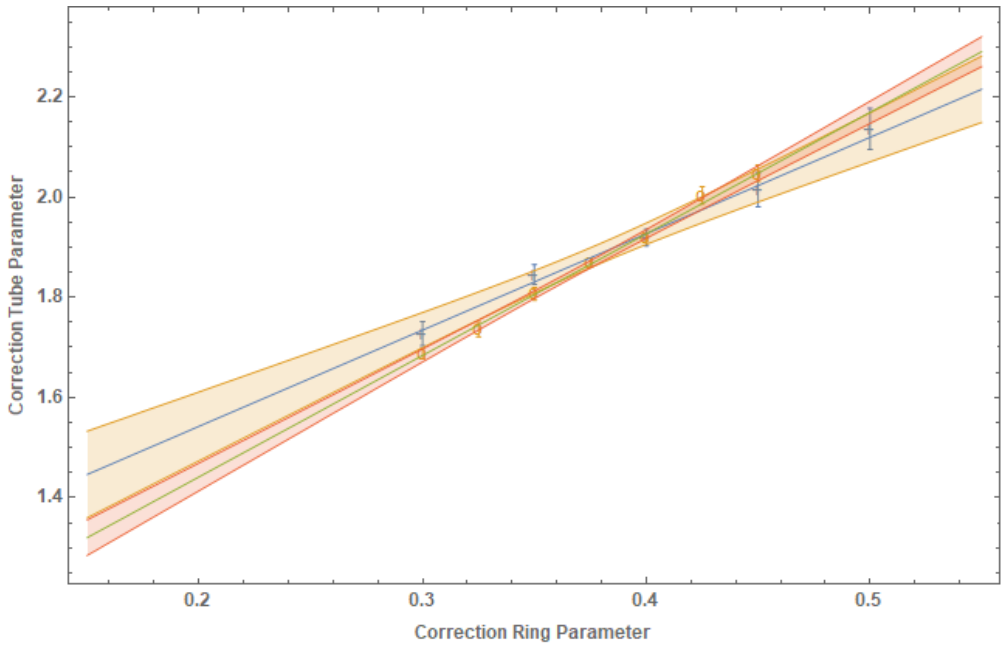

Figure 5.7 Example of the TOF-ICR trap tuning results at LEBIT. The intersection of the two lines indicates the 'optimal' correction ring/tube values to minimize any frequency shifts. Note the large error bands result in a large range of values where the true optimal value may exist. Observations with PI-ICR have revealed sensitivities to these parameters at < 0.01.

- Eject and record the spot distribution at the position-sensitive MCP detector.

Upon trapping, the ions undergo pure magnetron motion: the initial reduced cyclotron radius is effectively zero, and the magnetron radius is constant. As such, the frequency shift to the magnetron frequency from Eq. 5.7 can be probed through the axial amplitude of the ion bunch upon trapping. The initial axial amplitude of the ion bunch can be adjusted experimentally by altering either the energy of the ion bunch as it enters the Penning trap, or the time when the trapping potential is 'switched on'. In either case, the magnitude of the frequency shift for a given trap tune can be evaluated by observing the relative phase advance of the magnetron motion on the position-sensitive MCP detector.

The optimal trap tune will have the smallest relative frequency shift across the range of axial amplitudes as the C_4, C_6, etc. terms approach zero. Figure 5.8 shows a comparison of the relative frequency shifts for both simulated and experimental configurations. In a practical tuning scheme, one would optimize the correction tube electrode for a fixed correction ring parameter, invert the

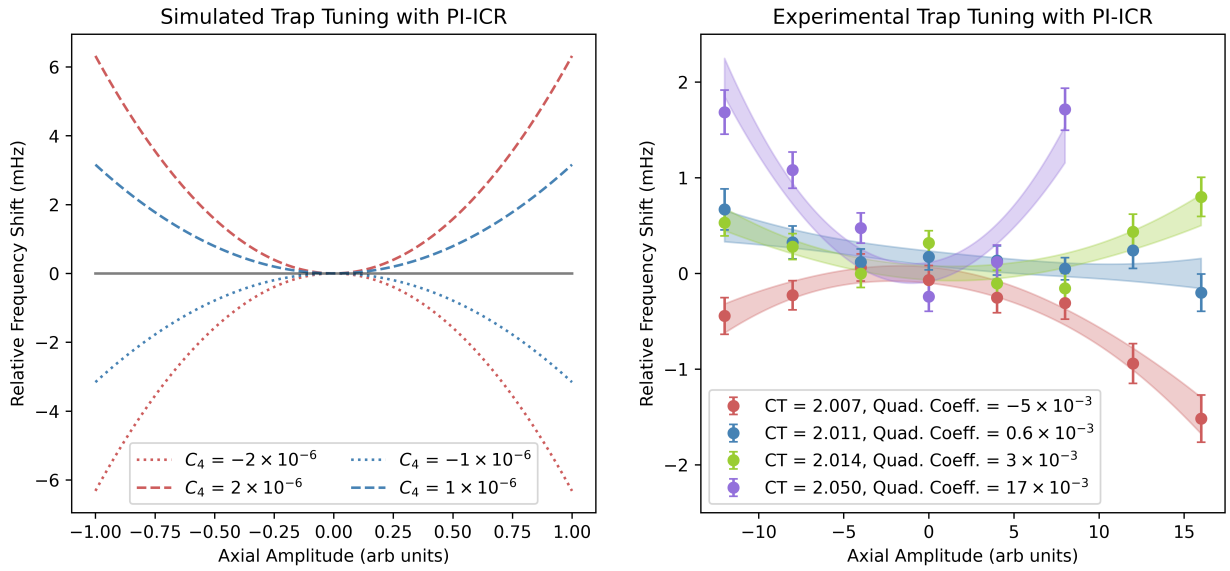

Figure 5.8 Evaluation of the trapping potential tuning for simulated octupole anharmonicities and experimental corrections with the correction ring and tube electrodes. The experimental data was collected with a fixed correction ring parameter of 0.476 for multiple correction tube (CT) parameters. The energy of the trapped bunch was scanned using the pulsed drift tube immediately before the 9.4 T Penning trap to adjust the initial axial amplitude of the ions.

procedure, and continue iterating until a stable result is found. Over the many tuning efforts at LEBIT, a wide-ranging set of correction tube and ring parameters have been found which reasonably minimize the trapping anharmonicity.

5.3.4 Final Validations for a Trap Tune

The procedure outlined above only probes the trap tune at one specific trap radius. However, the frequency shifts from an improperly tuned trap are known to have a radial dependence. This is relevant to PI-ICR as ions start at trap center and are driven to a larger radius. During this time the ions will experience a changing frequency shift and their final phase will reflect this. One can sensitively probe this effect by scanning the rf drive amplitude such that the ions are driven to a range of different radii in the trap. Note that the drive time must stay constant for the final phases of the ions to remain correlated! For a properly tuned trap, the ion should experience no frequency shifts as a function of radius and the ion position as a function of drive radius should remain linear. Conversely, an improperly tuned trap will display a bent shape as the ions experience additional

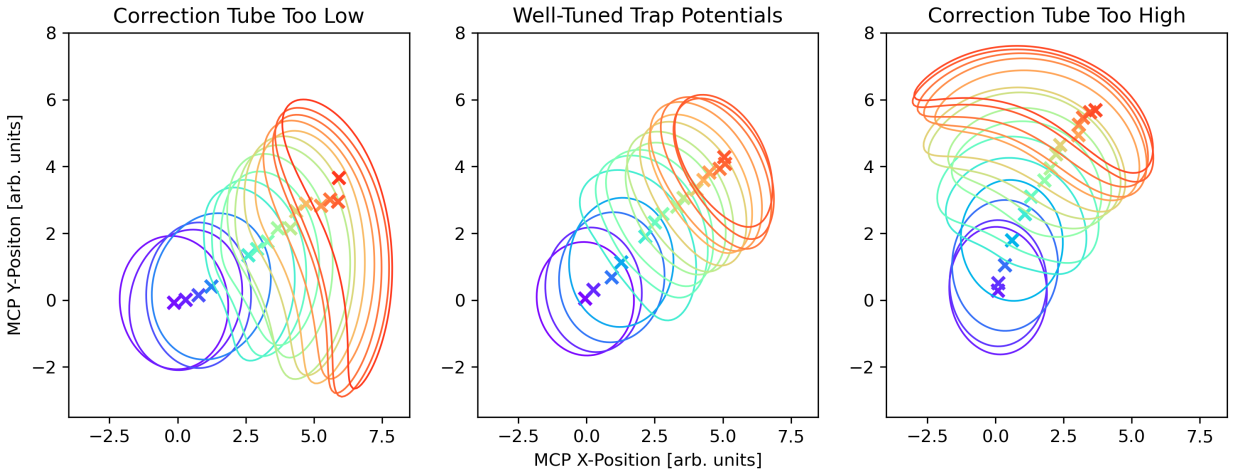

Figure 5.9 Comparison of a well-tuned trap (center) to trap tunes where the correction tube is either too low (left) or too high (right). Each plot was generated by scanning the dipole drive amplitude and recording the spot distribution on the MCP detector after 250 ms of reduced cyclotron phase accumulation time. In a properly tuned trap, the spot should move linearly as a function of the drive amplitude.

frequency shifts at larger radii. Figure 5.9 provides an overview of this effect for experimental data collected at LEBIT.

The extent of the bending for this test is proportional to the total trapping time. The procedure should be conducted with a total trapping time exceeding that of any precision measurement to be conducted. Additionally, this test can be used to sensitively probe the trap tune once the procedure in Sec. 5.3.3 has been completed. However, this method is significantly slower and is likely best used for the final fine tuning.

5.4 Impact of Off-Center Injection into the Penning Trap

The PI-ICR measurement cycle relies on a careful preparation and manipulation of the ions during their time in the trap. In particular, ions must be initially trapped as close to on-center as possible–i.e. the ion distribution should have zero magnetron and zero reduced cyclotron radii, and randomly sampled phases for both as well[1]. Ions which are slightly off-axis will undergo pure magnetron motion at that initial radius. If the PI-ICR measurement cycle starts at this point, the

[1] An alternative approach is to apply an initial ν_- dipole excitation to drive ions to the trap center. This requires careful tuning and is generally cumbersome. Lorentz steers provide a reliable and simple method for precise centering.

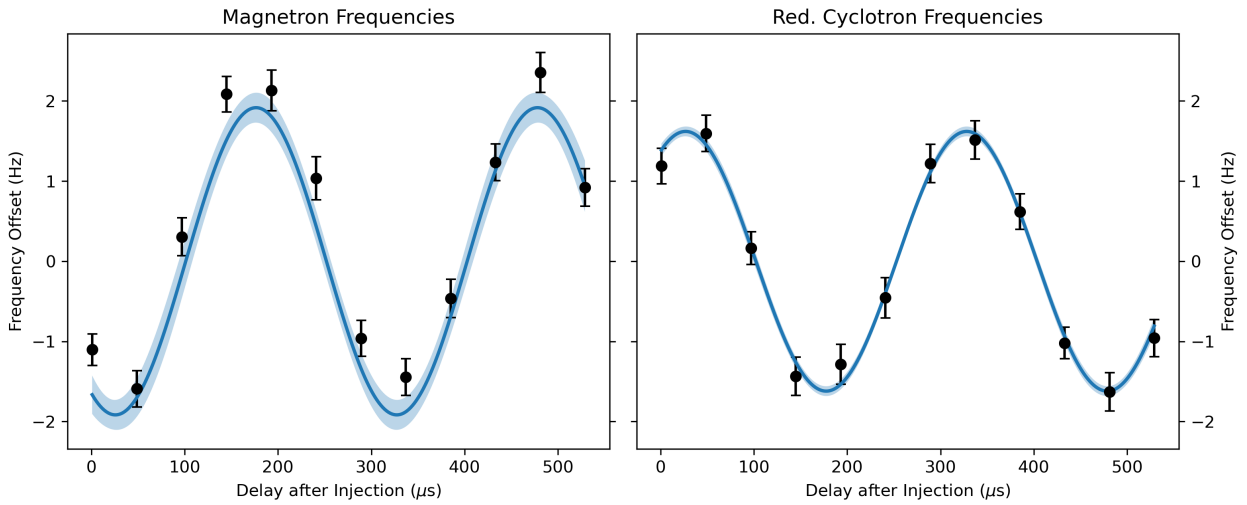

Figure 5.10 Observed frequency shifts in PI-ICR measurements of the magnetron and reduced cyclotron frequencies when ions are injected into the trap with an initial magnetron radius. A short delay time was added before the PI-ICR measurement cycle to allow the ions to accumulate some initial magnetron phase.

initial magnetron phase will propagate through the measurement. This introduces a magnetron phase dependence into the final determined phase based upon the total trapping time.

Figure 5.10 illustrates the impact of the off-center injection on the final determined frequency. In particular, slight differences to the total trapping time of the ions result in a significant frequency shift. If the total trapping time is constant across all spots then the frequency shifts to will cancel. However, this is not practical for the vast majority of experiments. Additionally, the conversion pulse will not necessarily be complete and can result in a broadened spot distribution.

While a Lorentz steerer provides very precise control over the injected ion position, small imperfections remain in the initial ion distribution. In general, these deviations impact spot quality to a much lesser degree than the initial ion energy spread. To ensure the initial magnetron phase distribution does not impact the final PI-ICR spot phase, LEBIT ensures the magnetron phases are uniformly random immediately after injection. In practice, once the ions are trapped and all initial cleaning has been completed, LEBIT adds a small wait time before starting the usual PI-ICR cycle. This wait time is scanned over one full magnetron period, such that the ion ensemble is guaranteed to have random magnetron phases on the average.

5.5 Trapping Field Stability

As discussed in prior sections, a PI-ICR measurement requires a minimum of three datasets: one to evaluate the center of the trap, one for the starting phase of the ions, and one for the accumulated phase of the ions. While some of these can be made redundant across the calibrant and ion-of-interest, the number of datasets remains sizable. Reducing the frequency for which all these measurements need to be taken is of great interest, and understanding their stability against drifting trapping fields is critical.

There are two principle ways in which the trap frequencies can evolve over time. Combining Eqs. 2.4, 2.5 we see the following relationship:

$$\omega_{\pm} = \frac{\omega_c}{2} \pm \sqrt{\frac{\omega_c^2}{2} - \frac{16q^2}{m^2(\rho_0^2 + z_0^2)} V_0^2} \,. \tag{5.8}$$

It is now clear how the magnetron and reduced cyclotron frequencies are related to both the magnetic field strength (via ω_c) and the endcap potential V_0. Importantly, the magnetron frequency is significantly decoupled from the magnetic field strength which results in a largely mass-independent quantity. A linear decay in the magnetic field strength is expected for a superconducting solenoid, and non-linear fluctuations have been shown to be of negligible impact at LEBIT [99]. The linear drift in B can be precisely compensated for through a current applied through a pair of insulated copper wires wound around the beamline within the magnetic field.

Figure 5.11 shows measured magnetron and reduced cyclotron frequencies observed at LEBIT over the course of 60 hours. Of particular note is the drifting cyclotron frequency suggesting an over-compensation of the magnetic field was present at the time. More telling is the linear drifting present in both the magnetron and reduced cyclotron frequencies at the same rate. There are several mechanisms which might individually account for such a drift, and the remaining discussion in this section is dedicated to investigations of these effects at LEBIT.

5.5.1 Stability of Trap Electrode Power Supplies

The drift slope directions for the respective $\omega_{\pm}$ frequencies could be explained by a trap depth which decreases over time (V_0 in Eq. 5.8). The stability of the trap endcap, correction tube,

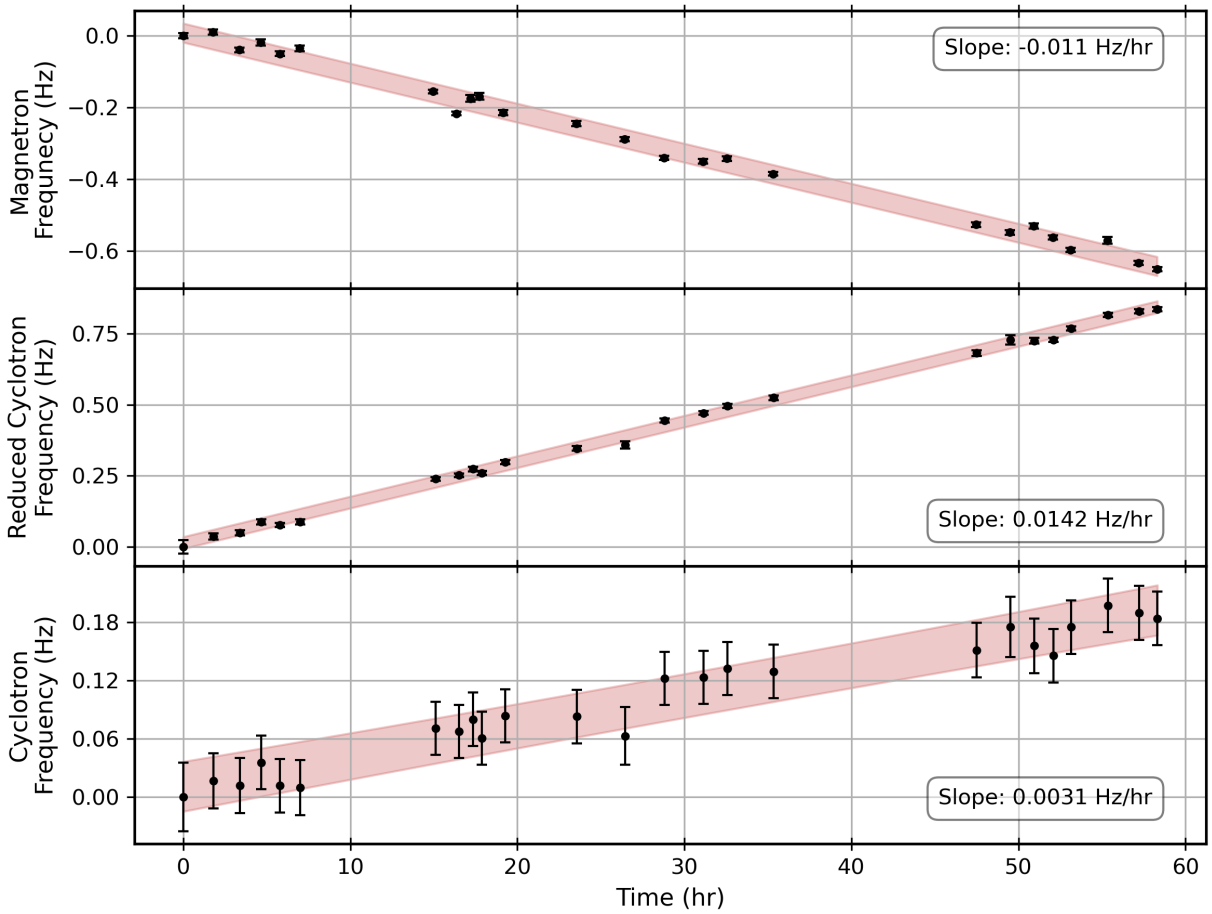

Figure 5.11 Measured magnetron and reduced cyclotron frequency drifts for $^{39}K^{+}$ over the course of an experimental campaign. The cyclotron frequency was determined as the sum of the two eigenfrequencies.

and correction ring voltages can independently or jointly alter the electric field harmonicity and consequently the effective trap depth. Thankfully, the stability of these supplies are straightforward to determine with the aid of a high-precision digital multimeter.

Voltage supplies often have a known temperature coefficient which dictates the sensitivity of the output to changes in environmental temperatures. LEBIT uses a Stahl Electronics 16-channel 50 V bipolar low-noise DC power supply for the trapping electrodes which quotes accuracies of 0.015% and ppm level stability over 24 hours. LEBIT and all electronics are situated in a confined laboratory space with an independent HVAC system. Figure 5.12 shows the output of the Stahl supply for the Penning trap endcap electrode, under load, over the course of an hour. An 8.5 digit

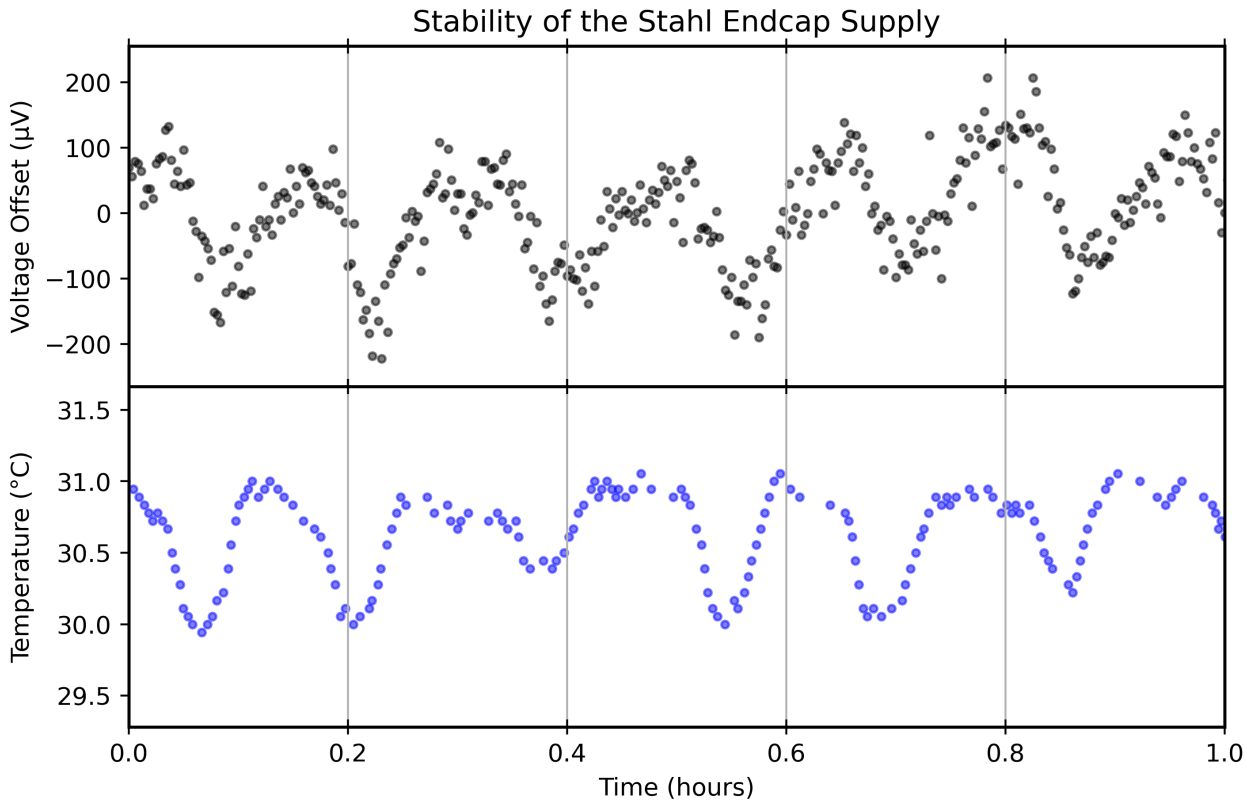

Figure 5.12 Comparison of the Penning trap endcap voltage over time, averaged over ≈1.6 s, along with the ambient room temperature.

Agilent 3458 digital multimeter was used to monitor the supply output. The multimeter calibration is quoted to be accurate across a ≈5°C temperature variation, and verified with a thermally insulated battery. A clear correlation between the endcap voltage and the ambient temperature can be clearly seen.

The observed fluctuations of ∼300 μV to the endcap over the course of ∼10 mins would represent a frequency shift of ≈0.02 Hz ($\delta\nu/\nu_c \approx 5 \times 10^{-9}$) over that time for masses ∼40 u in the LEBIT 9.4 T Penning trap. While certainly not insignificant, these fluctuations alone do not describe the long-term frequency shifts. Figure 5.13 shows the endcap potential across a longer observation period. A net linear drift of ≈150 μV/hr would be required to explain the observed frequency shifts. However, no such drift was observed during the measurement period.

Similar conclusions were also drawn for the power supply channels for the trap correction tube and correction ring electrodes. While a persistent drift in the trap power supplies cannot explain

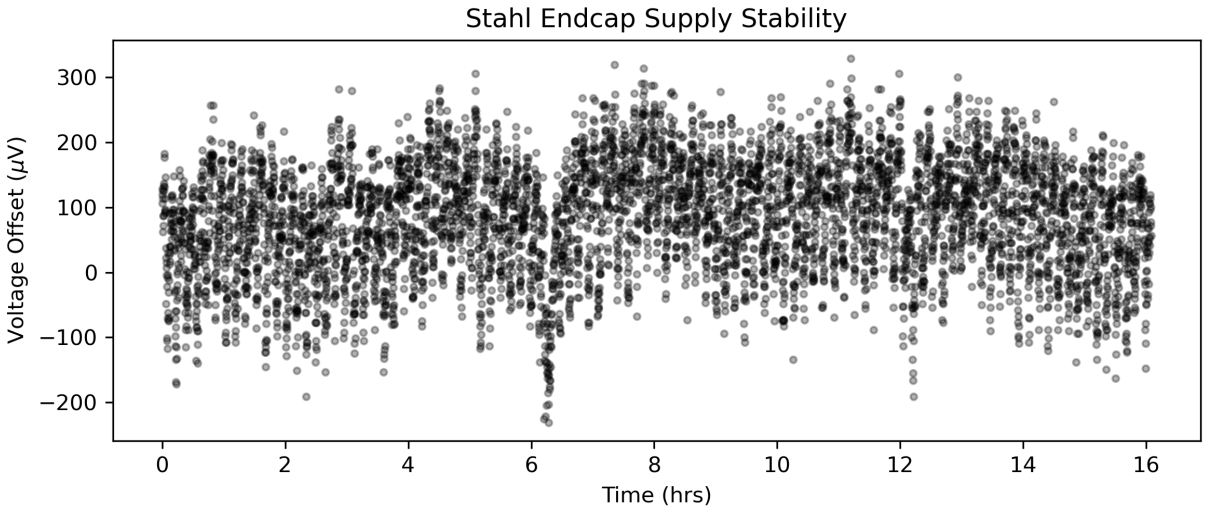

Figure 5.13 Stability of the Stahl power supply channel used for the LEBIT 9.4 T Penning trap endcap over the course of 16 hours. Each point was averaged over ≈1.6 s. Short term oscillations are the result of fluctuating ambient temperature.

the observed frequency shifts, it is clear that care must be taken during an experimental campaign for measurements with timescales similar to the HVAC cooling cycle.

5.5.2 Charge Accumulation at/near Trap Electrodes

The Penning trap electrode structure is mounted in place with alumina insulators which are well shielded from stray/cleaned ions (see Fig. 2.2). A discharge between electrodes in the magnetic field and/or ionization of any residual gas outside the Penning trap could lead to an accumulation/dissipation of charge on the insulating surfaces. The additional electric field induced from this surface charge may contribute to the observed in the trap depth. Given the respective signs of the frequency slopes indicating a decreasing trap depth over time, either a build-up of electrons and/or dissipation of positively charged ions are plausible explanations.

An additional known mechanism for charge build-up in a Penning trap is the 'patch potential' phenomena, where variations in the electrical potential can appear across conducting surfaces. These effects have been previously observed and quantified for Penning trap electrodes, despite the gold-plated surface finish used to minimize the impact [64, 108, 109]. However, patch effects and associated surface inhomogeneities become most relevant for small baseline potentials; all LEBIT

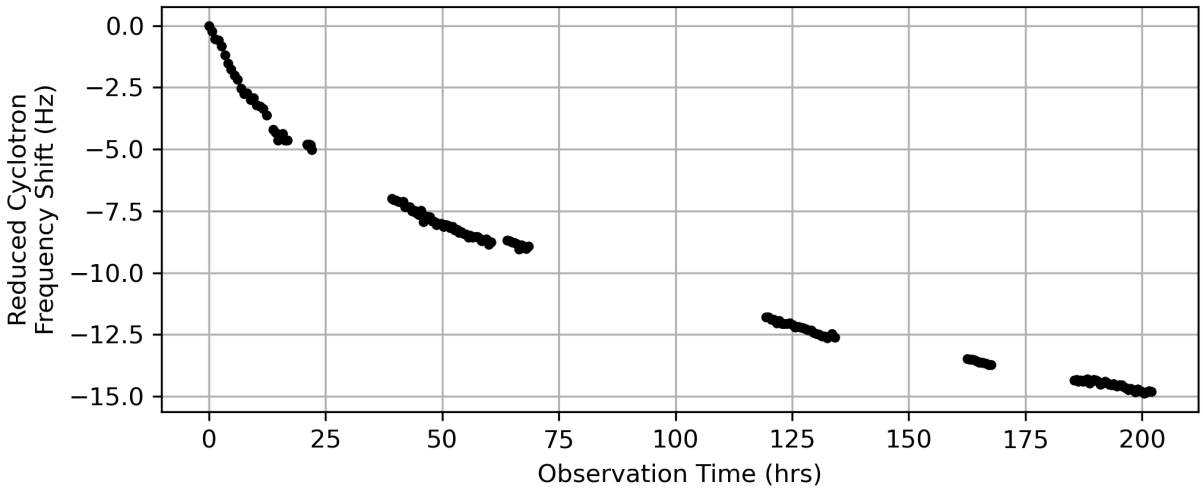

Figure 5.14 Measured reduced cyclotron frequencies after a discharge event between two drift tube electrodes after the Penning trap in the LEBIT 9.4 T mass spectrometer. Error bars are included, but are too small to resolve.

trap electrodes are $\gtrsim$10 V and expected patch fields contributions of $\sim 10^{-2}$ V/cm are unlikely to explain the observed frequency drifts.

Following a period of stable operation, a discharge between two drift tube electrodes in the drift field section after the Penning trap was observed. Afterwards, a significant degradation in the PI-ICR spot quality in addition to a large frequency jump was measured. Figure 5.14 shows the evolution of the reduced cyclotron frequency measured with PI-ICR shortly after the discharge. A near-constant cyclotron frequency confirmed the drifting reduced cyclotron frequency is the result of a changing trapping electric field. We posit that electrons produced from the discharge followed the potential gradient toward the trap electrodes, ultimately depositing onto the exposed correction tube electrode on the ejection side of the Penning trap.

The magnitude and timescale of this effect in this instance provides further evidence to suggest that the observed frequency drifts in prior experiments results from a slow charge buildup on an exposed trap electrode. Regardless, it is clear that great caution must be taken to prevent discharge events during an experiment otherwise the resulting frequency shifts can persist over several days. Thankfully, it is extremely easy to identify and diagnose the effect should it occur during a measurement.

5.5.3 Other Possible Effects

Thermal expansions of the trap electrodes would change the overall geometry and impact the net electric field shape. The LEBIT Penning trap is held at room temperature with no external temperature regulation. While there is relatively small thermal coupling between the trap electrodes and the beamline itself, the large thermal mass of the system could translate into a slow temperature drift for the trap electrodes. Thermal expansion/contraction of the electrodes themselves would change the fundamental trap dimensions ρ_0 and z_0 of Eq. 5.8. The bulk copper electrodes (neglecting the thin gold plating) have a linear coefficient of thermal expansion of $\approx 16.3 \times 10^{-6}$ m/(m $^{\circ}$C). In order to describe the observed 0.01 Hz/hr frequency shift, a corresponding temperature shift of ≈ 8 $^{\circ}$C/hr would be required. Clearly this is far beyond the normal environmental conditions.

The beamline inside the solenoid bore is held in place at either end with mechanical fasteners. External temperature and barometric drifts could also impact the beamline itself and slightly shift the electrode positioning within the magnetic field. Again, considering the temperature stabilized environment, this is not expected to pose any measurable change. The onset of the frequency shift also does not correlate to any known temperature drifts for a large temperature swing over the course of several days.

5.6 Frequency Shifts from Space-Charge Effects

Penning traps rely on precisely tuned voltages and electrode geometries to effectively trap ions. If large enough, the charges from many trapped ions can act to perturb the trapping field which in turn introduce shifts to the measured cyclotron frequencies. The impact of this effect depends both on the magnitude of the charge and the physical dimensions of the Penning trap electrodes. When considering the impact of space charge, two distinct scenarios must be considered. For a trapped ion cloud consisting of a single ion species, the induced space charge does not influence the center-of-mass motion of the cloud [110]. However, if the ion cloud consists of a mixture of different ions, then the center-of-mass motions can interact and result in significant frequency shifts [111]. The following discussion provides an initial assessment of the impact of space charge

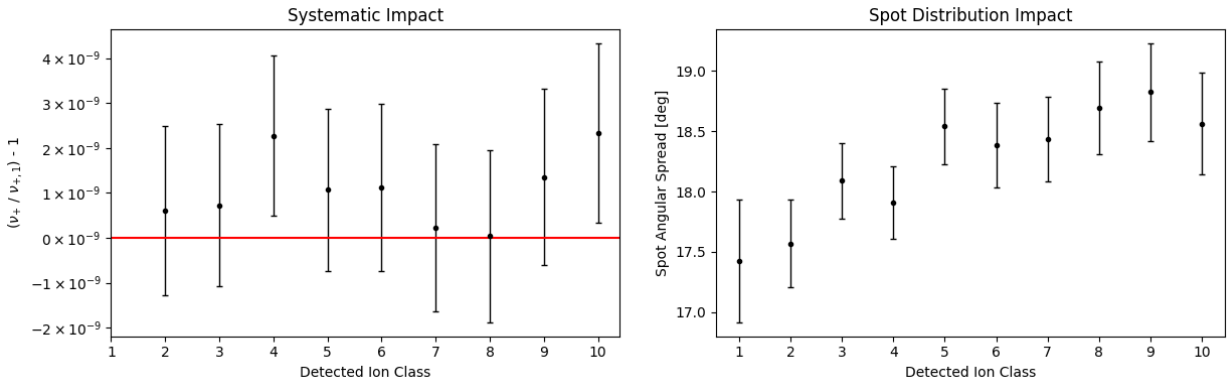

Figure 5.15 (Left) Frequency ratio for a given number of simultaneously detected ions relative to the frequency determined from single detected ions. (Right) Detected spot angular spread, fit from a polar Gaussian distribution, after the reduced cyclotron accumulation time. Each measurement of the reduced cyclotron frequency ν_+ used $\approx$ 500 ms phase accumulation time with a total of $\sim$1000 detected ions. The MCP detector for PI-ICR has an efficiency of $\approx$50%.

for a single ion species within the LEBIT Penning trap geometry.

Consider first the impact of single-species space charge effects in the context of PI-ICR mass measurements. In a perfect Penning trap, the center-of-mass motion of the ion cloud is preserved. However, both dipole and quadrupolar excitations must also be applied to the ions. Thankfully, both will also act upon the center-of-mass (in the on-resonance case) and will not be impacted by a large space charge beyond a broadening of the ion cloud distribution [42]. However, a broadened spot distribution may become subject to more sever trapping field anharmonicities which scale with the overall radius of the ion. While this can be largely mitigated with a proper tuning of the trapping field, it remains imperfect and thus important to quantify directly.

Figure 5.15 shows results for different numbers of simultaneously trapped $^{39}K^+$ ions to determine where this effect becomes relevant. Of particular note is that no statistically significant frequency shift to precisions $\approx 2 \times 10^{-9}$ are observed for up to 10 detected ($\approx$ 20 trapped) ions in the LEBIT Penning trap. However, for the higher numbers of trapped ions, a general broadening of the spot angular distribution is apparent, though the effect is relatively minor compared to the initial magnitude. Many of the rare isotope mass measurements of interest will be delivered at low rates, and for a single ion species in the trap, this systematic is negligible to the precisions of interest.

When the ion cloud in a Penning trap contains multiple ion species, space charge effects become

much more relevant. The center-of-mass motions of the ions can interact, and the trap excitations may not be resonant for all species resulting in potentially dramatic shifts to the observed cyclotron frequencies. This can often be mitigated through careful ion purification (as described in Sec. 2.3). However, in many cases it is not possible to fully isolate the ion of interest where contaminants are very close in mass and/or compose an overwhelming percentage of the mixture. In these scenarios, the extent of the space charge effects depends on many factors (percent composition, frequency separation, etc.) which extends beyond the work of this document. A more detailed systematic study is likely required on a case-by-case basis for measurements which must be conducted under these conditions.

5.7 Spot Sensitivity to Ion Purification Techniques

PI-ICR requires the trapped ions to be well constrained in energy and position in order to retain a minimal beam spot size at the detector for precise frequency measurements. At the same time, it is often necessary to remove contaminant ions from the trap to limit further systematic effects. The act of ion purification can inadvertently perturb the ions of interest and result in shifts to the determined frequencies. A discussion of several considerations for ion purification are discussed below.

Before ions enter into the Penning trap, a coarse time-of-flight filter is used to isolate ions within a narrow mass-to-charge (A/q) ratio. In its current configuration at LEBIT, a switching high-voltage potential is used to block ions outside a specified time-of-flight following ejection from the cooler-buncher. The ramping time of the high-voltage switch and intrinsic time-spread of the ion bunch determine the separability of the ions with this method. In general, ions with higher A/q ratios have overlapping time distributions and become harder to separate effectively.

When the gate is switched low/high before/after the ions of interest, some portion of the ion distribution may experience a small kick, altering the ion bunch energy spread. This effect is naturally prominent when the switching time of the filter is short relative to the ion time-spread, particularly for ions with higher A/q. When this is the case, PI-ICR beam spots increase in size, and

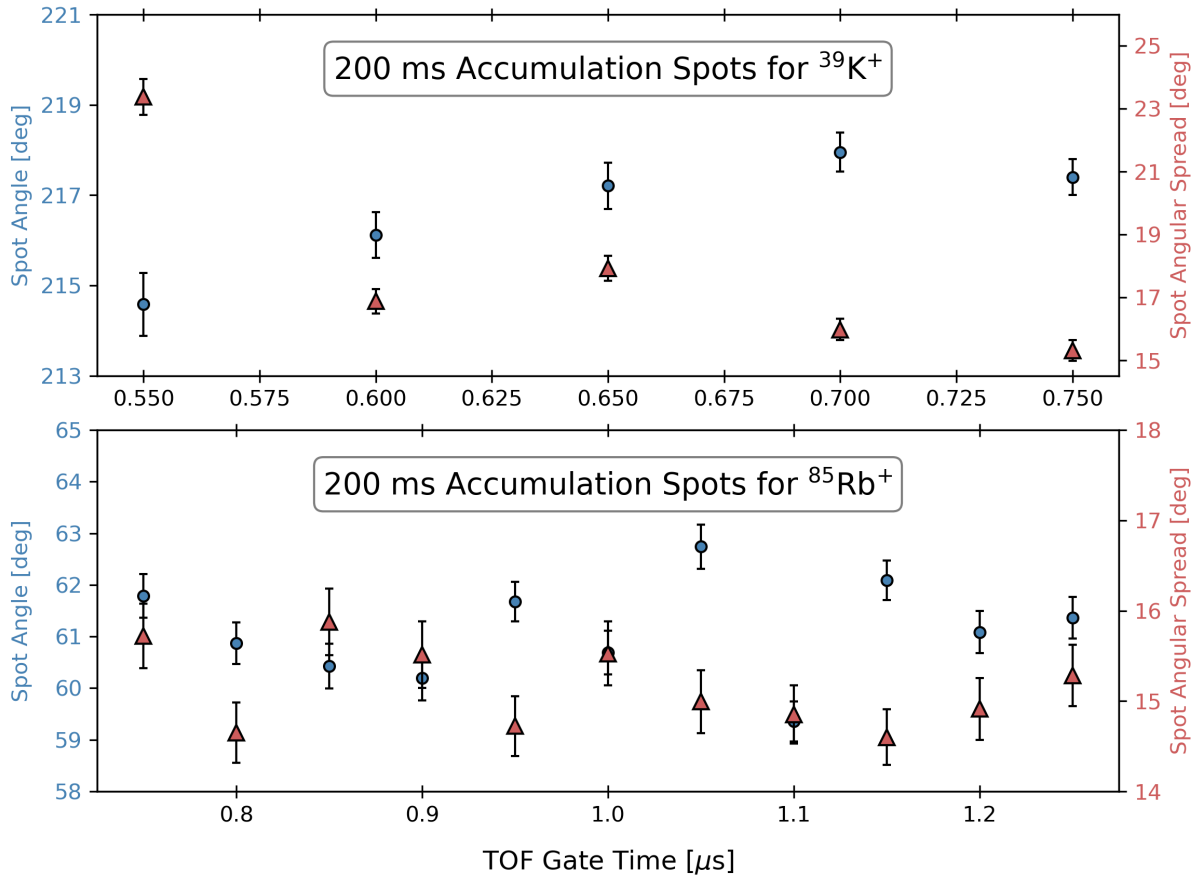

Figure 5.16 Impact of the time-of-flight filter before the Penning trap on the PI-ICR spots. The x-axis shows the duration the filter is opened to allow the ions of interest to enter the Penning trap. Shorter durations may perturb the ions as they pass through the filter and systematically affect the PI-ICR measurements. The impact on lighter masses is more apparent, though caution should be taken in general.

can completely smear over all angles. Figure 5.16 shows the impact of the time-of-flight filter for PI-ICR measurements. Short opening times are desirable to remove nearby contaminants, however, it is clear that there is a lower limit before PI-ICR measurements are affected. In the near future, LEBIT plans on replacing the existing plate setup for a Bradbury-Nielsen ion gate [112] which would provide significantly faster switching with minimal disturbance of the filtered ions.

Once ions are trapped, there are two (related) purification techniques: the SWIFT broadband approach [70], and a targeted dipole excitation in cases where contaminants are known, see Sec. 2.3. In the case of SWIFT, a narrow frequency window around the expected ion frequency is excluded

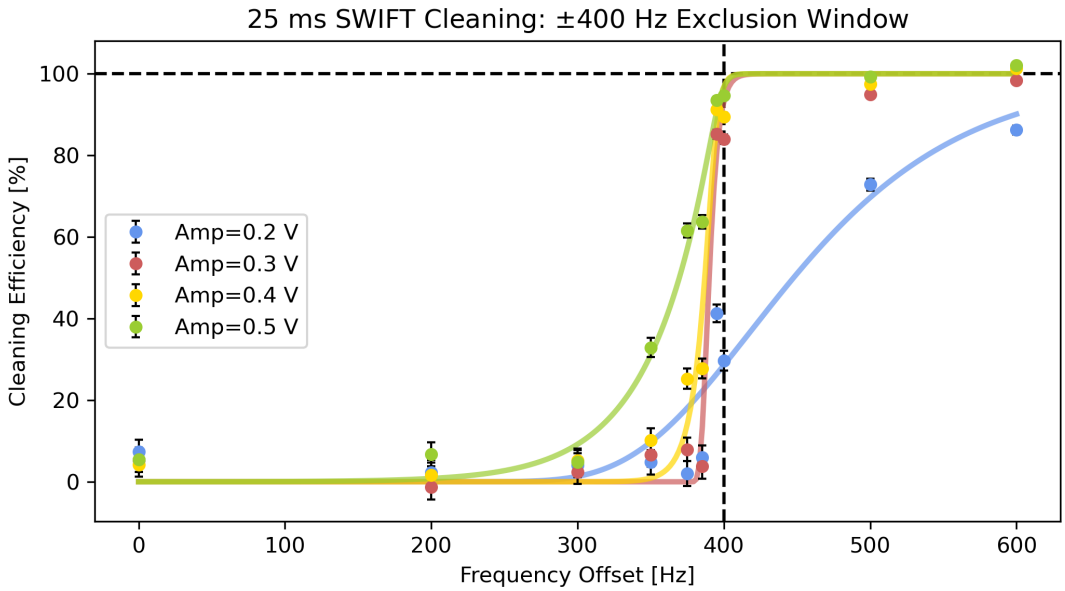

Figure 5.17 Cleaning efficiency of the SWIFT technique for a 25 ms excitation time, where a ±400 Hz exclusion window was set. A logistic-like function was fit to each dataset. The amplitude of the cleaning excitation must be properly set to prevent under-/over-cleaning outside the desired window. An optimal SWIFT cleaning occurs with an amplitude of ≈0.4 in this case.

to avoid disturbing the ions to be measured. However, if the exclusion window is too small then cleaning frequencies may partially excite the ions of interest. The broadening of the cleaning frequencies is inversely proportional to the excitation time (typically ~25 ms), and power broadening may also occur if the excitation amplitude is too strong. Figure 5.17 shows the impact on cleaning efficiency in cases where power broadening sets in (amplitude too high) or under-cleaning from insufficient excitation amplitude.

The SWIFT amplitude and duration also indirectly defines the minimum exclusion window that can be used. As the exclusion gap narrows, the frequency bleed-through naturally becomes closer to the ion of interest. For instance, a 25 ms SWIFT excitation with an amplitude of 0.3 V has a minimum exclusion window of ±200 Hz before the ion of interest (at the center frequency) is perturbed. Also relevant is the impact on PI-ICR spot quality as the ion frequency approaches the edge of the SWIFT exclusion window. This may occur if the ion of interest frequency is not well known beforehand, or if a nearby contaminant species is also within the SWIFT window. Figure 5.18 shows the SWIFT excitation begins to impact PI-ICR spots well before the edge of it's cleaning

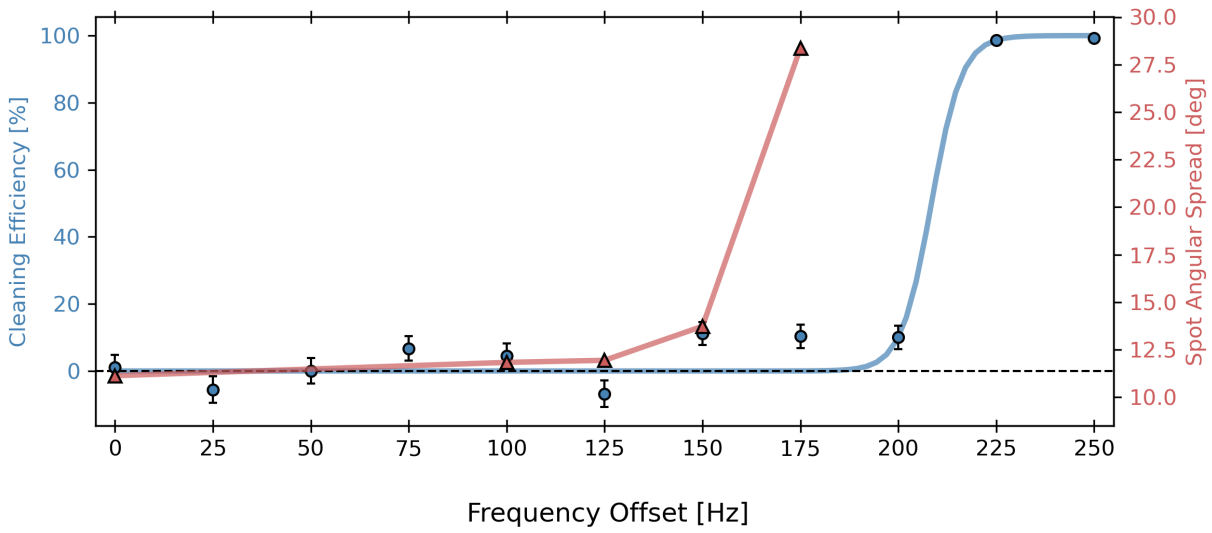

Figure 5.18 Comparison of the impact to the spot angular spectrum for a given frequency offset from the center of the SWIFT exclusion window of ±200 Hz for a 25 ms, 0.3 V excitation. A logistic function fit to the cleaning efficiency of the around this window is also shown.

exclusion window. Additional care must be taken for ions with large frequency uncertainties, or for isomeric/contaminant species.

In addition to SWIFT cleaning, a targeted dipole approach can be used to remove known contaminants that are within the SWIFT exclusion window. The duration of the dipole cleaning pulse determines the minimum frequency separation before the ion of interest is affected. At LEBIT, cleaning times of 25, 50, or 100 ms are commonly used, where isotope half-life is the main limitation. Similar to SWIFT, care must be taken to optimize the dipole excitation amplitude to adequately clean within the intended window. Figure 5.19 shows a comparison between cleaning efficiency and impact on the PI-ICR spot. A minimum frequency separation must be maintained from the cleaning pulse to prevent a partial excitation of the ion of interest. The results suggest a minimum frequency separation of ≈110 Hz for the 25 ms dipole cleaning pulse, while a separation of ≈60 Hz is required for the 50 ms case.

Additional shifts to both the mean angular and radial positions were also observed as a function of frequency offset. However, as these are coupled to the dipole excitation parameters, it becomes challenging to estimate the systematic impact. Deviations in the spot angular distribution highlight where the cleaning excitation perturbs the ions of interest. In general, spots subject to partial exci-

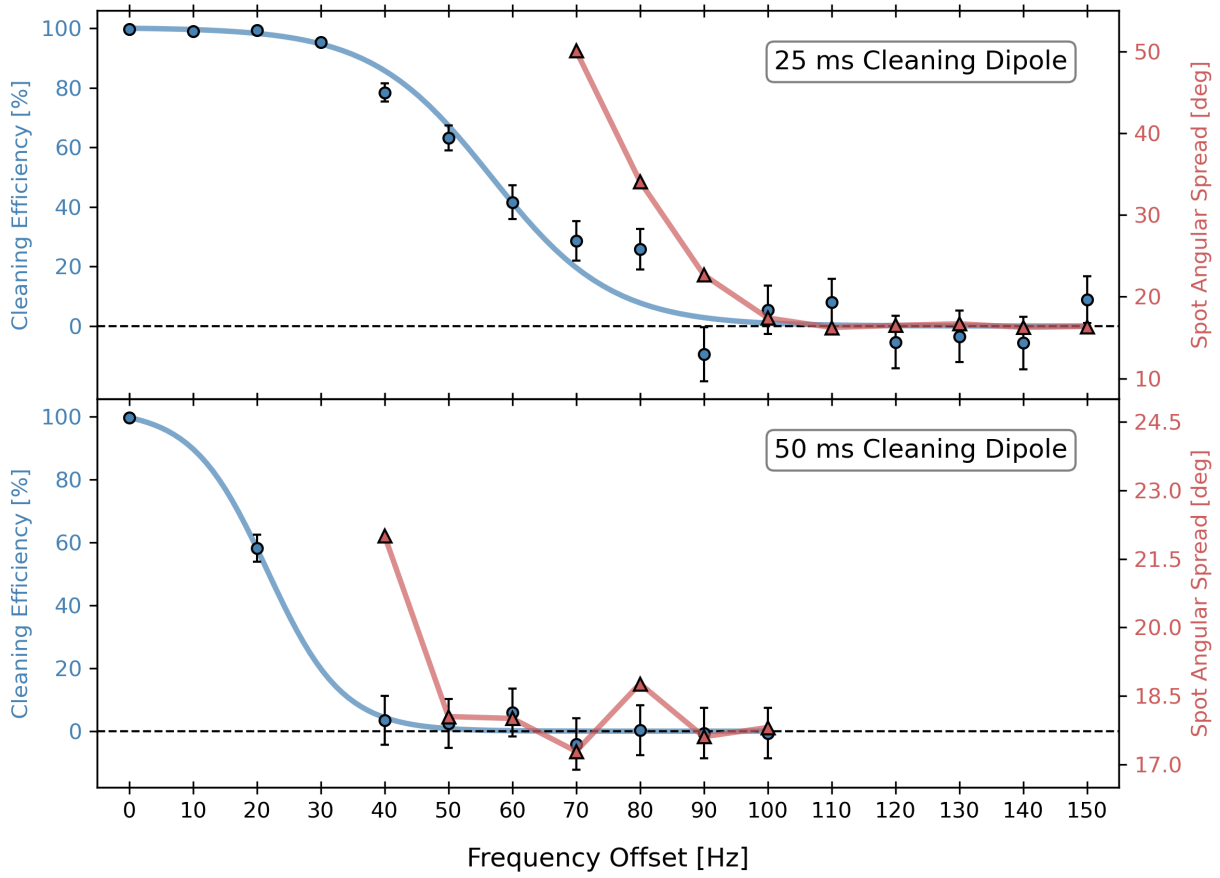

Figure 5.19 Impact of a 25 ms (top) and 50 ms (bottom) targeted dipole cleaning on PI-ICR spot quality for different separations between the ion and cleaning frequencies. A sigmoid function is fit to the cleaning efficiency data.

tations are quite distorted and easy to identify. The point of interest then is during an experimental campaign where the ion of interest has a large frequency uncertainty and one must decide where to clean a nearby contaminant or not. Figure 5.19 provides limits for selecting cleaning times and frequencies to ensure they are outside the ion of interests uncertainty region.

For a general rule of thumb, regardless of whether SWIFT or a dipole cleaning is used:

$$\nu_{\mathbf{IOI}} \pm \delta\nu \textbf{ should be outside of } \nu_{\mathbf{clean}} \pm 3/t_{\mathbf{excit}}$$

5.8 Impact of the Trap Excitations

The two excitations used during a typical PI-ICR cycle impact the final phase of the ions. The description for the ion phase evolution in Eq. 4.3 assumes the excitations are resonant with the ion frequencies. In the case where the excitations are only partially resonant or off-resonant (e.g. the expected frequency differs significantly from the actual) then the final phase and calculated frequency will be offset from the actual ion frequency. In practice, a rf excitation will have a broadened frequency spread with a FWHM = $1/t_{\text{excit}}$ such that long excitation times have a narrower frequency acceptance.

This feature can be leveraged for PI-ICR where nearby contaminants remain in the trap. A long drive time can be used to selectively drive the ions of interest while leaving the contaminants well separated on trap center. However, in some cases the ion of interest may have a relatively large frequency uncertainty relative to the excitation FWHM. For instance, at $A/q = 50$ a typical mass uncertainty of 400 keV/c^2 would correspond to $\delta\nu \approx 25$ Hz to 1σ. The case of a 3σ deviation could quickly enter the regime of a partial excitation for typical excitation times of 2 ms.

Figure 5.20 demonstrates the impact on PI-ICR spots for three different excitation times across different frequency offsets from the known ion frequency for $^{39}K^+$ ions. For the 100 ms reduced cyclotron accumulation time, a visible perturbation to the spot can be observed when the frequency offset is $\sim 5 - 10\%$ of the excitation FWHM. Naturally, the spot deviations will be amplified for longer phase accumulation times. During an experiment, one should use the initial low precision measurement to assess how off-resonant the excitations are and adjust accordingly.

Clearly, the shorter excitation times can better handle a larger frequency offset for the drive and conversion pulses. However, there are two dominant limitations to further shortening the excitation time. The first is the number of periods needed for the excitation to retain the desired effect. While no exact number has been determined, a minimum of few hundred cycles are thought to be necessary ($\sim$100 μs for common frequencies at LEBIT). The second restriction is the voltage limitations of the arbitrary function generators as shorter excitations require higher rf amplitudes. For the industry standard of $V_{pp} = 10$ V, LEBIT cannot go below a 0.5 ms drive and a 2 ms conversion. External

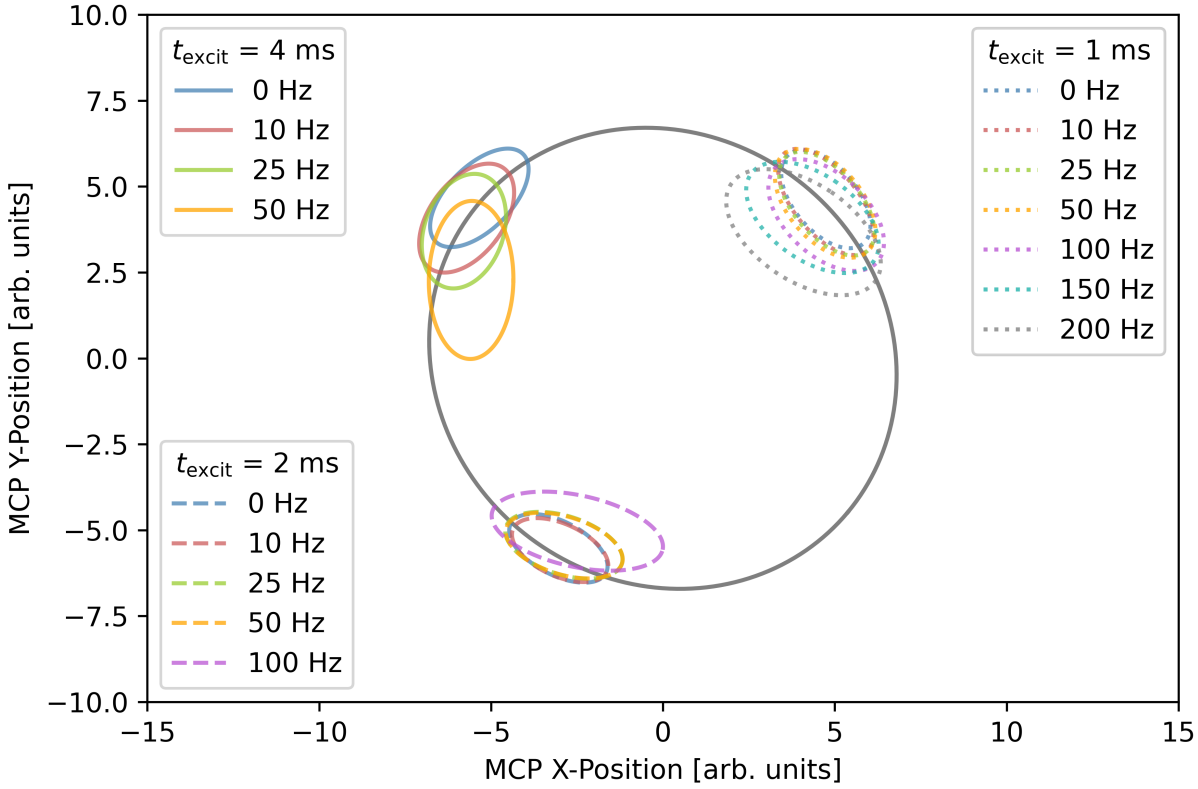

Figure 5.20 Comparison of three different excitation amplitudes/times for the PI-ICR conversion pulse across a range of frequency offsets from the true ion cyclotron frequency. Shorter excitation times have a broader Fourier frequency width and are expected to be less sensitive to off-center frequencies. Each spot was allowed to accumulate 100 ms of reduced cyclotron phase, and is represented on the plot by a fitted Gaussian in cartesian coordinates.

rf amplifiers can be used, though caution should be taken to consider the voltage ratings of all rf filtering and switching electronics. Additionally, most commercial rf amplifiers do not have uniform gain across a wide range of frequencies. This would require an additional calibration to properly calibrate the excitation amplitude for each frequency of interest.

There are a few additional related systematic considerations related to the trap excitations which will be addressed here. First, if the drive time is shorter than the conversion time, there is a risk that contaminant ions may be driven out, but not receive a full conversion pulse. These ions would smear out across a wide range of phases and potentially interfere with the ion of interest

spot. Similarly, if there happen to be contaminant ions in the partial excitation regime of the drive and/or conversion the resulting 'spot' can potentially overlap with the ion of interest. In both cases, care should be taken to identify contaminant species and adjust the drive and conversion pulses as necessary to ensure they remain separable from the ion of interest.

A final consideration comes from Eq. 4.3, where we see that the drive time accumulates reduced cyclotron phase and the conversion accumulates magnetron phase for the PI-ICR cycle. In the case of low-lying isomers, it may be beneficial to reduce the drive time to minimize the phase separation for the 'start' spot. Assuming a 500 μs drive time, every $\approx$5 Hz separation would result in a $\approx$1 degree difference in the final phase for a start spot. The conversion time is irrelevant in this context as the magnetron frequency is very weakly mass dependent ($\approx$ 0.02 Hz/amu at LEBIT).

CHAPTER 6

MASS OF ^{22}Al AND IMPLICATIONS OF AN UNLIKELY HALO

The results presented in this chapter were first published in Physical Review Letters [45]. Recent insights, measurements, and additional discussion are included as well.

6.1 Motivation for ^{22}Al Mass Measurement

Aluminum-22 is the last aluminum isotope stable to spontaneous proton decay, and defines the proton drip-line. Radioactive nuclei at and near the proton-drip line are of particular importance for nuclear models as their exotic nature is challenging to accurately predict [5, 13, 16]. These nuclei have also been observed to exhibit unusual structural properties and decay modes [14, 15]. One such possible feature is the presence of a 'proton halo': one or more of the protons extends far beyond the compact core. Recent efforts to identify and study these nuclei have provided invaluable information for our understanding of nuclear forces [19,20]. See Sec. 1.1 for additional discussion.

Studies of nuclei at the proton drip-line are often challenging: these nuclei are not easily produced at most radioactive beam facilities, and the confining nature of the Coulomb barrier typically suppresses proton halos. Precision mass information of these nuclei are of particular importance, as it reveals the binding energy of the nucleus [5, 6]. A proton halo requires a very small amount of energy holding the proton to the nucleus, aka 'proton separation energy', S_p. Precise mass information is also necessary to calculate nuclear charge radii from isotope shift measurements [22], which can directly probe the size of a halo structure.

Initial evidence for a proton halo in ^{22}Al was extrapolated from an exceptionally small proton separation energy determined from nuclear mass models with nearby nuclei [26]. Recent excitement for a halo structure has come from isospin-symmetry breaking effects in nuclei with similar properties [113]. Specifically, an observed isospin asymmetry of $\delta_\beta = 2.09(96)$ in the Gamow-Teller β^+ transition from the first excited 1^+ state of ^{22}Si and with its mirror ^{22}O β^- transition [114] suggested that the first 1^+ excited state of ^{22}Al could exhibit a halo structure. Given that this state is expected to be proton-unbound, information on the longer-lived ground-state of ^{22}Al is

critical to resolving this case. Predictions and extrapolations are limited by the available mass precision, providing a strong motivation for a precise mass measurement of the ^{22}Al ground-state to be performed.

6.2 Experimental Procedure

A detailed description of the experimental facilities used to produce and prepare the rare isotope beam for mass measurements at LEBIT can be found in Chapter 3. A brief discussion is included here with specifics regarding the measurement of ^{22}Al.

The radioactive ^{22}Al isotopes were produced at the facility for rare isotope beams (FRIB) via projectile fragmentation of a primary ^{36}Ar beam impinging upon a ~8 mm thick ^{12}C target with an energy of ~200 MeV/u. The cocktail beam was then sent through the advanced rare isotope separator (ARIS) [74] to provide an initial purification of the beam. The beam then passed through two aluminum degraders, 3287 and 1015 μm thicknesses respectively, and then through a 1003 μm 2.67 mrad aluminum wedge to prepare the beam for stopping inside the advanced cryogenic gas stopper (ACGS) [76]. Following stopping, the ions were extracted from ACGS as a low energy (30 keV/Q) continuous beam, which was then purified further with a magnetic dipole separator, with a mass resolving power of $m/\Delta m \approx 1500$. During gas stopping, rare isotopes may split into a wide range of molecular forms from residual impurities in the helium buffer gas. The optimal A/Q, with the highest rate of the rare isotope, was determined with a silicon detector following the mass separator. A scan over a wide range of A/Q revealed the highest activity at $A \approx 22$, corresponding to bare ^{22}Al^{+} ions. No other significant molecular splitting was observed. The $A/Q \approx 22$ beam was then sent to the stopped beam area.

Upon entering the LEBIT facility, the beam was first sent to the radio-frequency quadrupole cooler-buncher [78] which converts the high-emittance continuous beam into short ~100 ns low-emittance pulses optimized for efficient capture in the LEBIT 9.4 T Penning trap [115]. The known half-life of ≈ 85 ms [116] for ^{22}Al limited the cooler-buncher accumulation time to ~$3t_{1/2}$ to balance decay loses with the available rare-isotope rate. Prior to entering the Penning trap, the ion pulses

were again purified with a coarse time-of-flight filter to only allow ions of a specific mass-to-charge ratio through. Once captured in the trap, ions were precisely purified using the stored waveform inverse Fourier transform (SWIFT) technique [70]. To calibrate the magnetic field, a stable isotope is used, whose mass is very well known, such as those detailed in the AME2020 [26]. Stable $^{23}Na^{+}$ was also delivered with the $^{22}Al^{+}$ beam as a contaminant, and was also readily produced by the LEBIT offline plasma ion source. Ideally, an isobaric contaminant would be used, however, no contamination at $A/Q = 22$ was observed with sufficient rates to perform the magnetic field calibrations.

Both the time-of-flight ion cyclotron resonance (TOF-ICR) and phase-imaging ion cyclotron resonance (PI-ICR) measurement techniques were employed to determine the cyclotron frequency and ultimately the ion mass, as described in Chapter 2. At the time of the experiment, ^{22}Al remained unmeasured with a suggested 400 keV mass uncertainty based on extrapolations of the nearby mass surface [26]. Additionally, the relatively short half-life limited the possible excitation times in TOF-ICR and phase accumulation times in PI-ICR to $50 - 75$ ms. The $^{23}Na^{+}$ calibrations were not limited by rate or half-life, and 500 ms excitations times for TOF-ICR, and 150 ms phase accumulation times for PI-ICR were used. Each measurement of the ion of interest, ν_c was interleaved by measurements of the reference ion, $\nu_{c,\mathrm{calib}}$. The mass ratio of the ion of interest was then recovered with Eq. 2.11, and the average ratio $\bar{R}$ was weighted by each measurements uncertainty.

A number of systematic effects for Penning trap mass spectrometry are introduced in Chapter 5. Considerations for TOF-ICR measurements are well studied, and the main considerations for this experiment include magnetic field drifts, mass-dependent shifts between calibrant and ion-of-interest, and space charge effects. Non-linear temporal magnetic field instabilities have been shown to contribute no more than 1×10^{-9} [99] to $\bar{R}$ over the course of one hour, which exceeds the duration and precision of any measurement performed in this experiment. The 1 u mass difference between $^{22}Al^{+}$ and the $^{23}Na^{+}$ calibrant is expected to contribute $\delta\bar{R} \approx 2 \times 10^{-10}$ [98], which is negligible compared to the statistical uncertainty of $\gtrsim 10^{-8}$ for this measurement. Lastly, space

charge and isobaric contamination effects [42, 117] were minimized by maintaining less than five simultaneously trapped ions following beam purification with dipole cleanings and SWIFT.

Many of the detailed studies relevant to PI-ICR were not yet finalized at the time of this measurement. While extensive studies have been performed at other Penning trap facilities [85, 100–102], many effects have been shown to be system dependent. To capture any potentially unknown effects specific to LEBIT, additional systematic studies were performed offline immediately following the experiment. Both $^{23}Na^{+}$ and $^{22}Ne^{+}$ were produced with the LEBIT plasma ion source, where the stable ^{22}Ne acted as an isobaric stand-in for ^{22}Al. Care was taken to retain experimental conditions as exactly as possible, and all trapping times remained unchanged.

6.3 Mass Measurement Results

A total of seven independent mass measurements of ^{22}Al were completed over the experimental time of 16 hours: four using the TOF-ICR technique, and three with the PI-ICR technique. Examples of these measurements can be seen in Fig. 6.1 This experiment marks the commissioning of the PI-ICR technique at LEBIT. The cyclotron frequency ratio $\bar{R}$ of Eq. 2.11 was determined by the average of each measurement, weighted by the statistical uncertainty. For TOF-ICR, $\bar{R}_{\mathrm{TOF}} = 1.044\,068\,76(6)$, and PI-ICR, $\bar{R}_{\mathrm{PI}} = 1.044\,068\,841(14)$. The combined experimental result yields $\bar{R} = 1.044\,068\,837(14)$, corresponding to a mass excess of 18 092.5(3) keV and a proton separation energy of 100.4(8) keV. Figure 6.2 illustrates each of the measurements and their combined results.

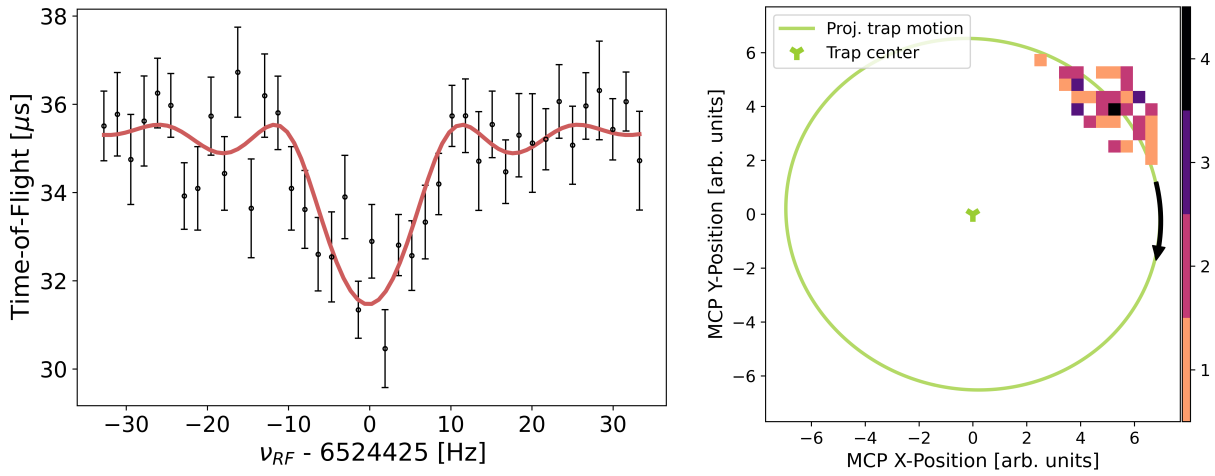

Figure 6.1 (Left) Sample $^{22}Al^{+}$ TOF-ICR resonance and fit. A 75 ms quadrupolar excitation and ≈350 ions resolved the frequency to $\delta\nu/\nu \sim 1 \times 10^{-7}$. (Right) An example of a PI-ICR phase measurement for $^{22}Al^{+}$. A 50 ms reduced cyclotron phase accumulation time and ≈50 ions resolved the frequency to $\delta\nu/\nu \sim 1 \times 10^{-8}$.

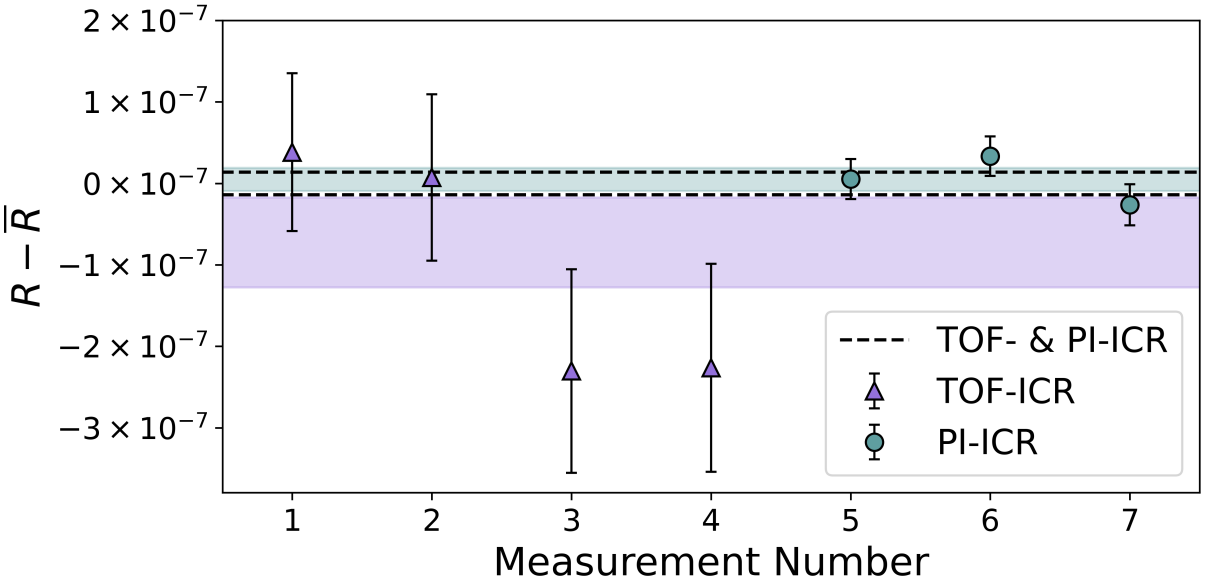

Figure 6.2 Difference between the frequency ratios $\nu_c(^{23}Na^{+})/\nu_c(^{22}Al^{+})$ from AME2020 [26] (R) and this experiment ($\bar{R}$). Measurements using the TOF-ICR are shown as the blue triangles and blue uncertainty region, and PI-ICR measurements as the red circles and red uncertainty region. The combined weighted uncertainty band of all results is shown between the dashed lines. All uncertainties are to 1σ.

6.4 Discussion and Predictions from Theory

With the success of the experimental mass measurement, we can turn to nuclear theory to evaluate the predictive power of different models and extrapolate additional properties of ^{22}Al. This section provides a detailed description of two independent nuclear models, how they compare to the newly measured mass, and importantly their predictions regarding the possibility of a halo structure present in ^{22}Al. In short, both models are in good agreement with our experimentally determined observables, and suggest that a ground-state halo structure is not likely to exist for ^{22}Al.

6.4.1 Universal *sd*-shell (USD) Model

The shell model remains a workhorse for nuclear theory: the protons and neutrons are modeled independently as occupying hierarchical energy levels, analogous to atomic shell theory where electrons occupy orbitals in a predictable manner. For nuclei such as ^{22}Al, which have nucleons in the $s-$ and $d-$shells, the 'Universal SD-shell' (USD) model is an ideal tool. The USD model is capable of predicting properties of interest for these nuclei based on empirical fits to experimental data from well-studied nuclei. Relevant to ^{22}Al and the possibility of a halo structure is the ability to predict the matter radius (how large the nucleus is), and whether the valence proton occupies the $1s_{1/2}$ shell (which is characteristic of halo structures). Additionally, we can compare our experimental binding energy and compare to the model prediction to gauge the general reliability of the USD model for ^{22}Al. The following discussion introduces the model, assumptions, and findings. Ultimately, there is little evidence of a likely halo structure, despite the model accurately replicating other experimental observables.

The low-lying structure for the nuclei around ^{22}Al can be described within the *sd* ($0d_{5/2}$, $0d_{3/2}$, $1s_{1/2}$) model space. Several "universal" *sd*-shell (USD) Hamiltonians have been developed over the last 40 years. They are all obtained by starting with a set of two-body matrix element (TBME) obtained with nucleon-nucleon potentials re-normalized to the *sd* model space. The singular-valued decomposition (SVD) method is then used to constrain linear-combinations of TBME to obtain lower uncertainties for binding energies and excitation energies. The total number of parameters

which describe the sd model space is $p = 66$, which consists of three single-particle energies with an additional 63 TBMEs. There are $n_v < p$ linear combinations of the TBMEs that are considered to well-determine the data for the SVD method. The remaining $p - n_v$ linear combinations which do not replicate the data are then set to the 'starting' Hamiltonian, and used to obtain an improved set of the TBMEs.

The first types of USD Hamiltonians [118] in 1984 was obtained from nuclei with $Z = 8 - 20$ and $N - Z \geq 0$ in the isospin-formalism: the TBMEs are labeled by the quantum numbers (J, T). To account for the Coulomb interaction, a constant shift was applied to the binding energy data for each isotope. This original USD Hamiltonian was updated in 2006 using a larger dataset for 608 states in 77 nuclei, resulting in the USDA ($n_v = 30$) and USDB ($n_v = 56$) Hamiltonians [119]. The starting interactions was based on the Bonn-A potential re-normalized to the sd-model space using the TBMEs in Table 20 of [119]. These models produced an RMS deviation of 0.15 MeV for USD, USDA, and USDB between experiment and the calculated energies.

In 2020, the latest SVD fit including the Coulomb and isospin-dependent strong interactions, treated explicitly, with an expanded dataset including proton-rich nuclei ($Z = 8-20$ and $N = 8-20$) resulted in the USDC Hamiltonian [120]. The total set consisted of 854 states in 117 nuclei, where the USDC is based on $n_v = 56$ linear combinations starting with the Bonn-A interaction for the strong-interaction part (the same as USDB). Additionally, the USDI Hamiltonian was obtained using an initial set of TBMEs obtained from the valence-space in-medium similarity renormalization group (VS-IMSRG) approach [121, 122]. The VS-IMSRG TBMEs contains contributions from three-body interactions between the valence space and the ^{16}O core nucleons. The RMS deviation between the experimental and calculated energies for both USDC and USDI was 140 keV. Ground-state binding energies predicted by USDC and USDI are relative to ^{16}O: absolute energies are obtained by adding the experimental energy of -127.619 MeV for ^{16}O. These two Hamiltonians are used to predict the properties for proton-rich ^{22}Al.

From the experimental results in Sec. 6.3, $S_{p,\mathrm{exp}}(^{22}\mathrm{Al}) = 100.4(8)$ keV. The USD shell model predictions are in good agreement within the 140 keV RMS deviation: $S_p(^{22}\mathrm{Al})$ are 40 keV (USDC)

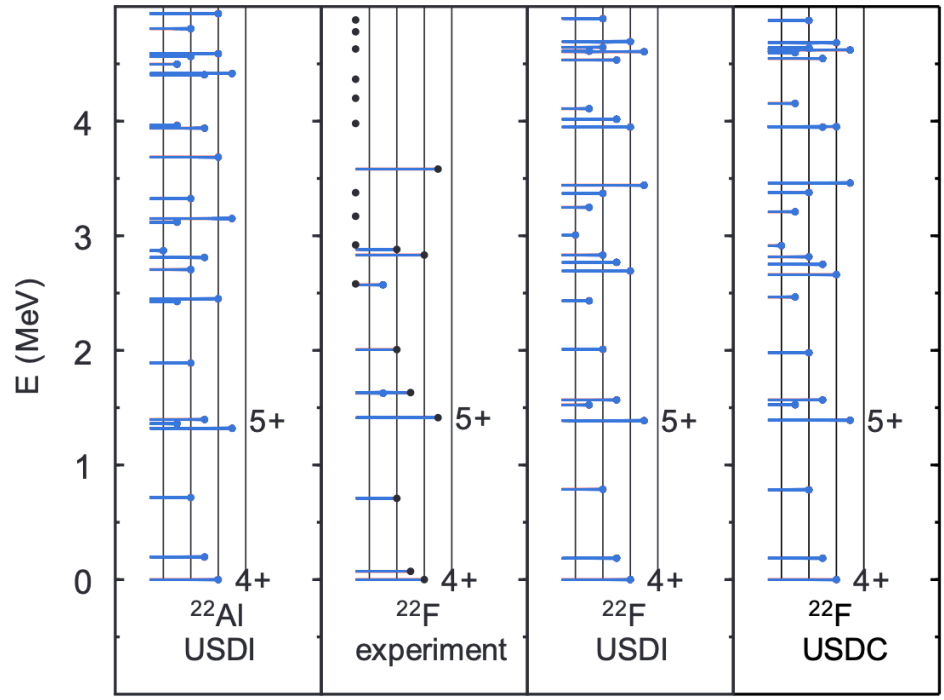

Figure 6.3 (Left Panel) Predicted energy states for the ^{22}Al spectrum obtained from the USDI Hamiltonian. (Right Panels) Experimental levels of ^{22}F (up to 5 MeV) compared to the results obtained from the USDI and USDC Hamiltonians. The horizontal lines in the figure are proportional to the J. value for positive parity states. For the ^{22}F experimental data, levels with unknown J are shown by black dots, and levels with uncertain J are indicated by the red lines ending with a black dot.

and 30 keV (USDI). Additionally, the calculated energy spectra for the mirror nucleus ^{22}F in Fig. 6.3 is in excellent agreement with experiment. Mirror nuclei pairs (where the proton in one nuclei is swapped for a neutron in the other) share very similar properties and energy level spectra. As such, the spectra for ^{22}F should closely mirror that for ^{22}Al. Importantly, USDI predicts a 4^+ ground-state for ^{22}Al.

A special consideration for proton-rich nuclei is the Thomas-Erhman shift, as discussed in Sec. V of [120]. Loosely bounded single-particle states with low-ℓ values are known to be lowered in energy relative to those with high-ℓ values. This results from the extended size of the low-ℓ states where the kinetic energy of the newly-extended wavefunction decreases. The TES depends of the specific state and the related spectroscopic factors [120], and cannot be corrected by modifying the single-particle energies in the Hamiltonian as it is a many-body effect. This shift can be quite

dramatic: for example, the $1/2^+$ excited state in ^{17}F is shifted down by 0.376 MeV compared to its energy in the mirror nucleus ^{17}O. In the ^{22}Al mass region there are excited states which have a significant $\ell = 0$ spectroscopic factor with a TES has high as -0.75 MeV for (see Fig. 12 of [120]). Predictions from USDI suggest that the 4^+ ground-state for ^{22}Al has a minimal $0s_{1/2}$ ($\ell = 0$) proton occupation of 0.29, and 0.38 for the low-lying excited states. As these are relatively minimal, the corresponding ℓ=0 TES for the ^{22}Al ground state is small.

The low-lying 3^+ excited state in ^{22}F is only 0.072 MeV above the 4^+ ground state. Despite the isospin symmetry between the pair, the TES from the larger $1s_{1/2}$ occupation of the 3^+ state in ^{22}F could result in a 3^+ ground state for ^{22}Al, as suggested by [123, 124]. The calculated β^+ decay properties of ^{22}Al, however, are more consistent with the generally accepted 4^+ ground-state assignment. It remains important for an experimental measurement of the spin-parity and moments for the ^{22}Al ground-state to better describe its structure.

6.4.2 Particle-Plus-Rotor Model

The intent of the particle-plus-rotor model for the case of ^{22}Al is to probe the relationship of a deformed (i.e. non-spherical) nucleus with a weakened binding of a proton. With sufficiently weak binding of the proton, a halo structure would be enhanced. In principle, the ^{22}Al nucleus (13 protons, 9 neutrons) is modeled by the well-studied ^{21}Mg nucleus (12 protons, 9 neutrons) acting as a 'compact core' with an additional valence nucleon attached. The interaction between the core and valence proton is modeled by a simple function which contains a term controlling the nuclear deformation. The experimental binding energy for ^{22}Al is used to appropriate set the interaction strength. Ultimately, the model suggests sufficient deformation allows for a halo structure to develop, but said deformation has yet to be experimentally verified. The following discussion goes into further detail regarding the model and interpretation of the findings.

From the experimental results in Sec. 6.3, the exceptionally small proton separation energy of ~0.1 MeV allows for the investigation of a ground-state halo structure with the particle-plus-rotor model (PRM) including couplings to continuum states. This model allows one to probe the

effects of deformation via the $s_{1/2}$—$d_{5/2}$ quadrupole coupling, which can enhance the occupation of s-waves. In effect, this acts to lower the proton $1s_{1/2}$ shell which is a key requirement for the formation of a halo structure.

The binding of the last unpaired proton in ^{22}Al is described by modeling the interaction of a core/rotor nucleus, ^{21}Mg, with an additional proton. For the purpose of this model, we assume only coupling between the rotor angular momentum, j_r, with that for the weakly-bound valence proton, j, play a role in the particle-plus-rotor dynamic:

$$\vec{j}_{\mathrm{PRM}} = \vec{j}_r + \vec{j}. \tag{6.1}$$

The angular momentum from the structure of ^{21}Mg, J_i, can be ignored for our purpose as all nucleons in ^{21}Mg are expected to be paired and coupled to 0^+, except for one well-bound neutron in $0d_{5/2}$. The low-lying multiplets $(1, 2, 3, 4, 5)^+$ and $(2, 3)^+$ of ^{22}Al are associated with $j^{\pi}_{\mathrm{PRM}} = 5/2^+$ and $1/2^+$, respectively, and the states within each multiplet are degenerate.

As in a previous application of the PRM in [125], the interaction between the rotor and valence proton is represented by a Woods-Saxon potential, with an added quadrupole deformation parameter β_2. The wave function can then be expanded by the channel wave functions described by the usual quantum numbers (n, l, j) for the valence proton, in addition to j_r for the rotor. Each channel wave function is expanded using the Berggren basis which accounts for couplings to the continuum. The coupled-channel equations can then be solved exactly through direct diagonalization.

With the model in place, the parameters are initially tuned to expected and experimental values. The results of the shell model calculations in Sec. 6.4.1 are not indicative of any significant deformation in ^{22}Al. As such, spherical symmetry for ^{21}Mg is assumed ($\beta_2 = 0$). The Woods-Saxon potential is then adjusted to reproduce the experimental binding energy for ^{22}Al described in Sec. 6.3. Additionally, the energy spectra for ^{21}Mg was used to fix the $1s_{1/2}$ shell at about 200 keV above the $0d_{5/2}$ shell which are understood as the Nilsson orbits for $\beta_2 \neq 0$. These s.p. energies differ from those in magic nuclei to account for the absence of residual interaction in the PRM. Under these assumptions, the following parameters were obtained: a diffuseness $d = 0.67$ fm,

a radius $R_0 = 3.2$ fm, a depth $V_0 = 54.8$ MeV, a spin-orbit coupling $V_{so} = 3.62$ MeV, and a Woods-Saxon Coulomb potential radius $R_c = 3.0$ fm.

The results of interest are obtained by varying the deformation parameter β_2 and calculating the ground-state energy and channel wave function norms for ^{22}Al. Figure 6.4 shows both prolate ($\beta_2 > 0$) and oblate ($\beta_2 < 0$) deformations act to lower the ground-state energy, suggesting the deformed system is characterized by a weakly bound valence proton.

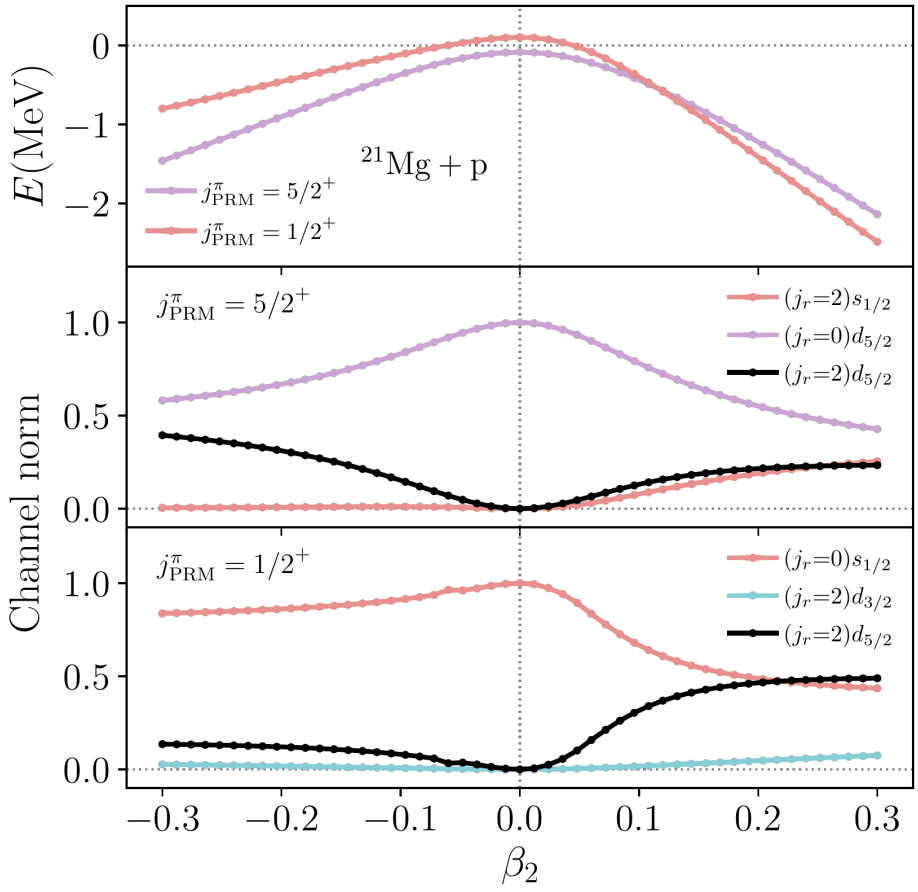

Figure 6.4 Energy of the ^{21}Mg+p system (top panel), and norms of channel wave functions for $j_{\rm PRM} = 5/2^+$ (middle panel) and $1/2^+$ (lower panel) as a function of the quadrupole deformation parameter β_2.

From the shell model calculations in Sec. 6.4.1, one expects predicts minimal deformation $|\beta_2| < 0.1$ for the ground state of ^{22}Al in the $0d_{5/2}$ state. As a result, the middle panel of Fig. 6.4 shows a small $(j_r = 2)1s_{1/2}$ channel wave function weight. This suppression of the $s_{1/2}$ state for the

valence proton does not allow the formation of a halo structure, in good agreement with the shell model predictions. Conversely, for $\beta_2 > 0.1$, one can see that the $1/2^+$ PRM state associated with the $(2,3)^+$ multiplet in ^{22}Al does lowers in energy, becoming the ground state. Since this state is dominated by the s-wave channel (bottom panel in Fig. 6.4, a halo structure would be likely to form. The necessary quadrupole deformation to achieve $\beta_2 > 0.1$ is not supported by the shell model, however, relativistic mean-field calculations [126] and data evaluation [127] predict $\beta_2 = 0.284$ and 0.226, respectively. Results are not affected significantly if one readjusts the core-proton potential to match the experimental binding energy with the latter deformation estimate as a guess.

6.5 Perspectives for the Possible Halo Nature of ^{22}Al

The mass measurement of aluminum-22 revealed a very weakly bound valence proton, which is one of the key indicators for a halo structure to form. Despite this finding, theoretical calculations of the nuclear structure suggest the valence proton does not lie in the s-shell as expected for a halo nucleus. Rather, the occupation is predicted to lie in the p-shell, which limits the spatial extent of the valence proton and restricts the formation of a halo. Additional investigations suggest that a sufficiently deformed ground state of ^{22}Al would allow for the valence proton to occupy the s-shell. However, there is no current experimental justification for a deformed structure.

Around the same time our results were published, an additional mass measurement of ^{22}Al was published by the cooler storage ring in Lanzhou [34] using the the $B\rho$-defined isochronous mass spectrometry method. Their independent measurement determined the mass to 10 keV, which remains in good agreement (1σ) with our results at a precision of 0.3 keV. Of interest in their results were *ab initio* calculations using the valence-space in-medium similarity renormalization group (VS-IMSRG) approach. Ultimately, their findings for a ground state halo in ^{22}Al are similar to those presented in Sec. 6.4: there is insufficient probability for the valence proton to occupy the $s_{1/2}$ state necessary for a halo structure to exist. However, their results do suggest that there is an increased likelihood for a halo structure to emerge in one of the excited nuclear states, see Fig. 5 in their results.

An additional *ab initio* study was conducted in [128] to better understand the signatures for a proton halo in ^{22}Al. Their results well reproduced experimental mirror energy differences, Gamow-Teller strengths, and mirror asymmetry parameters. Ultimately, they found that the ground state could not support a halo structure, though a halo-like structure was possible in the first 1^+ excited state. The work of [129] used a Gamow shell model which also posits a more pronounced halo-like structure in the excited 1^+ state in ^{22}Al but not the ground state. However, as with the theory results of [34], the excited states of ^{22}Al are expected to be proton unbound and cannot support a halo structure.

A recent study of the initial evidence for a halo structure was undertaken in [130]. The authors suggest that the findings in [113] are unconvincing, as it can be explained by the expected asymmetry due to the likely unbound nucleus ^{22}Si relative to the exceptionally stable doubly-magic ^{22}O. Furthermore, the results involve the excited states in ^{22}Al, which cannot be be considered a halo state since these excited states are proton-unbound. As such, the original conclusions based on an unexpectedly large observed asymmetry are likely in error.

The authors in [130] conducted an additional study with a deformed and triaxial relativistic Hartree-Bogoliubov in continuum model to further probe the possibility that a deformed ground state could support a halo structure. The results suggest that triaxial deformation would be required, and even then only a very minor likelihood of a halo structure. Yet another study in [131] using a relativistic density functional accounting for parity, deformation, and the continuum found predominant p-wave occupation, which acts to strongly inhibit a halo structure. A study using a deformed Skyrme-Hartree-Fock method also concluded that there is little room for a halo structure as the least-bound proton valence state is $1d_{1/2}$, through results are strongly correlated to deformation effects [132].

Two recent experimental results for ^{22}Al shed additional light on the uncertain case for a proton halo. A recent decay experiment at FRIB made the first observation of the weak β-delayed α transition from the isobaric analog state in ^{22}Mg to the ^{18}Ne ground state [133]. This uniquely fixes the ^{22}Al ground state at 4^+. Similar to the results presented here with the shell model, the 4^+ ground

state strongly restricts the formation of a halo structure as the valence proton is not dominated by an *s*-wave centrifugal barrier. Furthermore, a differential mean square charge radius measurement of the ^{22}Al ground state was recently completed by the beam cooler and laser spectroscopy (BECOLA) facility at FRIB [134]. This directly addresses the proton distribution of a nucleus, and revealed no statistically significant increase in the charge radius compared to ^{23}Al.

In conclusion, despite the exceptionally weak proton separation energy of ^{22}Al, there is no theoretical or experimental indications of a halo structure in the ground state. The potential for a halo-like structure in an excited state of aluminum-22 cannot be supported as they are proton unbound.

CHAPTER 7

NEXT PHASE OF PI-ICR AT LEBIT

Over the past decade, the PI-ICR technique has been fully realized and successfully commissioned at the LEBIT facility, enabling many important mass measurements. As the capabilities at FRIB continue to grow, LEBIT is uniquely positioned to provide critical mass information for many exotic nuclei. For these measurements delivered at very low rates, one major limitation of the PI-ICR technique is a reduced detection efficiency for determining ion positions (around 50% compared to ≈100% for TOF-ICR). The sensitivity of PI-ICR still far exceeds that of TOF-ICR with this limitation, yet several recent advances with MCP detectors provide opportunities to further expand towards lower-rate isotopes. This chapter provides an overview for a number of improvements underway for PI-ICR at LEBIT, in addition to novel applications of PI-ICR for the highest-resolution beam purification.

7.1 Upgraded Detectors for Improved Sensitivity

For the PI-ICR mass measurement technique, the high sensitivity and precision are correlated to the angular resolution of the observed spot on the MCP detector. The angular resolution is determined by two factors: the angular spread (i.e. the Gaussian distribution width) and the number of detected counts. Certain factors impacting the spread of the angular distribution may be optimized, but are fundamentally limited by the ion characteristics once trapped. However, recall that the dipole drive at the start of the PI-ICR cycle preserves the initial size of the spot. By driving the ions to larger radii, we reduce the angular spread and thus improve the frequency resolution. Though, this too is limited in practice by the size of the extraction hole in the Penning trap endcap.

Assuming a relatively fixed angular spread for a spot, the uncertainty in the center will largely scale by the square root of the number of counts. Short of delivering more ions in the first place, this is primarily limited by the detection efficiency of the position sensitive MCP detector. For a standard setup, the inherent efficiency for recovering full position information is around 50%. Note that it is not possible to place the MCP detector in the Daly configuration for ≈100% efficiency

if one desires to retain accurate position information. An additional constraint with 2D delay-line anode setups is the detector dead-time and multi-hit overlap: if multiple ions hit the detector near-simultaneously (≈30 ns window) in close spatial proximity, there is a high-likelihood that one or more of the positions will be lost. In the past, LEBIT has mitigated this effect to some degree with an advanced algorithm to dis-entangle the position signals with some success.

Thankfully, recent developments to both MCP detectors and delay-line anodes allow for a significantly higher detection efficiency with effective 'zero' dead-time. The recently improved MCP design with a funneled shape at the entry sections of each hole (where the electron avalanche is produced) allows for a stronger current to form and makes detection easier. From tests performed at Roentdek Handels GmbH, the funneled design improves the detection efficiency for pairs of particles by 160%: at LEBIT we would expect an improvement from 50% to 80% efficiency.

Additionally, Roentdek Handels GmbH provides a 'HexAnode' delay-line anode detector which utilizes three independent delay-lines (all three rotated by 60° relative to the other) compared to the standard two [86]. The added redundancy of a third delay-line allows for unambiguous position determination as long as the relative time or spatial distance/time between any two hits is above the pulse-pair dead-time. In other words, the HexAnode detector is only 'dead' if two particles hit simultaneously in the same position. This is particularly relevant when the rare isotope is delivered with contaminants/isomers which cannot be cleaned and may greatly increase the detected counts at the detector. Combined, these advances are expected to greatly improve the sensitivity of PI-ICR mass measurements, and effort remains active to implement both.

7.2 Advanced Isomer Separation with PI-ICR

LEBIT will also continue to serve an important role for other low-energy experiments, e.g. as an ultra-high resolution mass separator for the lowest-lying isomers. There are several cases where low lying isomeric states are particularly relevant for nuclear astrophysics (also referred to as 'astromers') as they can impact the flow of material during the r-process and rp-process. Typical approaches for beam purification use magnetic separation ($\delta m/m \gtrsim 10^{-4}$) or using multi-reflection

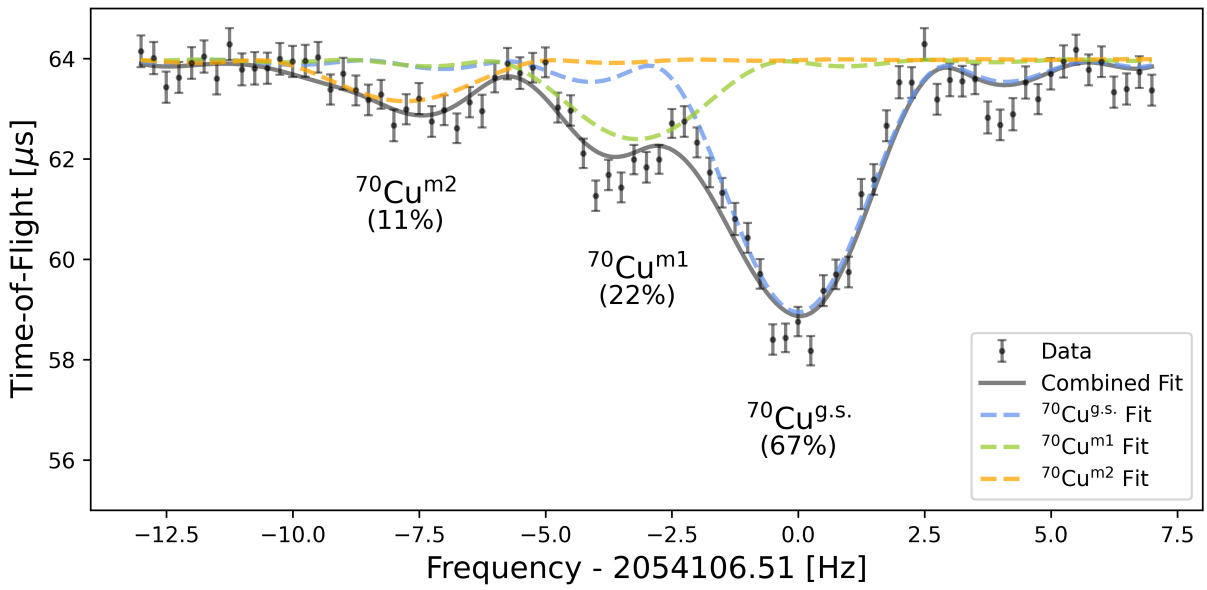

Figure 7.1 A TOF-ICR measurement of $^{70}Cu^{+}$, which has two known isomers with excited energies of 101.1 keV and 242.3 keV [135]. A 350 ms excitation time resolves all three states in ^{70}Cu. Percent composition was determined by the relative resonance strength for each component.

time-of-flight (MR-TOF) mass spectrometers ($\delta m/m \gtrsim 10^{-6}$). However, there are many interesting cases which exceed these limits, particularly for heavy masses.

^{70}Cu is one such case, where the ground state is separated from two low-lying isomers at 101.1 keV and 242.3 keV [135] which would require $\delta m/m < 1.5 \times 10^{-6}$—right at the upper limit for the existing purification techniques. In a recent experiment, the LEBIT 9.4 T Penning trap was used to isolate each state and deliver the separated beam to the SuN++ total absorption gamma ray spectrometer [136]. Figure 7.1 shows the TOF-ICR resonance containing the three states in ^{70}Cu observed at LEBIT. The classic dipole cleaning approach was used to separate each state. However, this approach is limited by the Fourier width of the cleaning pulse compounded by the initial energy spread of the trapped ions. The main bottleneck was then the efficient isolation of each state while delivering rates needed by the SuN++ detector.

The ^{70}Cu experiment operated near the limits where dipole cleaning with a Penning trap would be effective, yet there exist many interesting science cases with heavy elements and/or lower lying isomers. The PI-ICR mass measurement technique offers a unique opportunity to isolate even

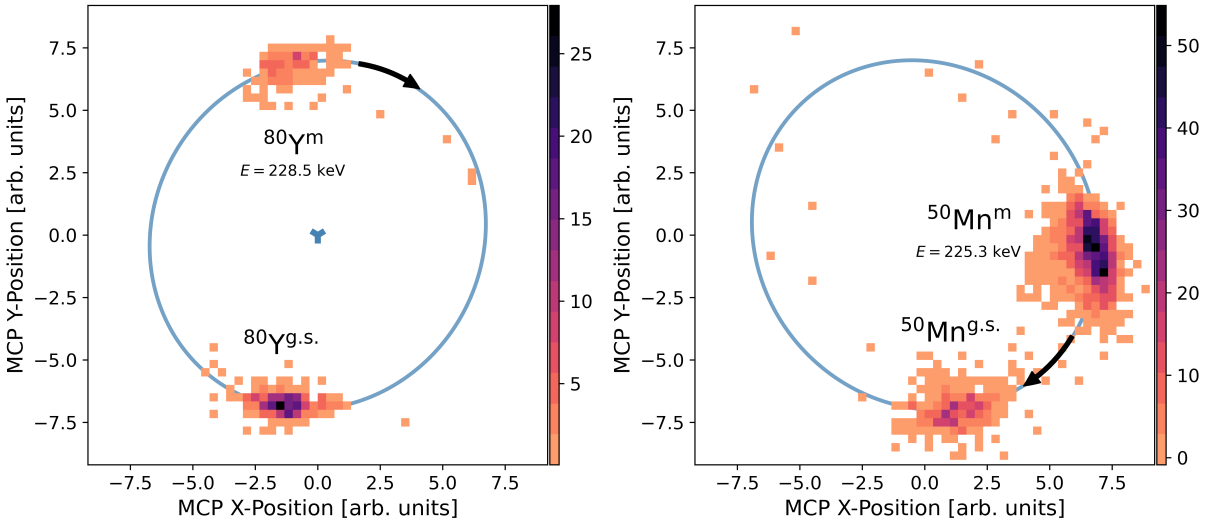

Figure 7.2 (Left) A PI-ICR phase measurement of $^{80}Y^{2+}$, which has a known isomer with an excited energy of 228.5 keV and half-life of 4.8 s compared to the g.s. half-life of 30 s. A 50 ms reduced cyclotron phase accumulation time separates the two masses by $\approx 180^{\circ}$. (Right) A PI-ICR phase measurement of $^{50}Mn^{2+}$, which has a known isomer with an excited energy of 225.3 keV and a half-life of 1.75 min compared to the g.s. half-life of 283 ms. A 5 ms reduced cyclotron phase accumulation separates the two masses by $\approx 60^{\circ}$.

the lowest-lying isomers thanks to its spatial separation capabilities. Figure 7.2 shows example PI-ICR spectra where both the ^{80}Y and ^{50}Mn ground states are separated from their respective low-lying isomer. A number of planned upgrades to the PI-ICR detection system will allow LEBIT to precisely separate an isomer without partial contamination of the other states or compromising on the beam rate to downstream experiments. The following discussion highlights the key concepts which will enable these experiments in the very-near future.

The basic isomer separation scheme with PI-ICR would simply require a spatial separation of the desired state from the others. For instance, a reduced cyclotron accumulation time of $t_{\text{sep}} = 1/(2\Delta\nu_+)$ will separate two ion species by π radians. For $\nu_+ \sim 3$ MHz and $A/q \sim 50$, a 100 keV isomeric state would require 75 ms to separate fully in the trap. Similarly, for $A/q \sim 100$, a 100 keV isomer would require 350 ms to separate. In practice, a significantly shorter separation time may be used as long as the angular distributions remain sufficiently separated. After identification and confirmation of separation, a set of adjustable slits in front of the MCP can then be used to isolate the desired state. Retracting the MCP out of the main beamline would then allow for delivery

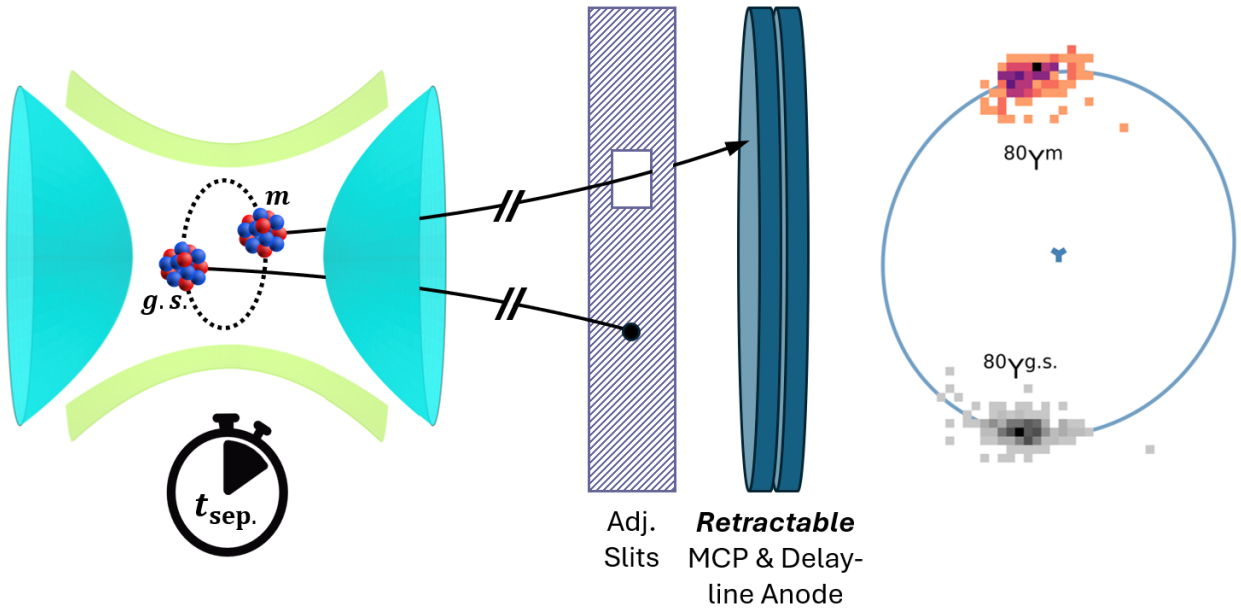

Figure 7.3 Schematic of the proposed isomer separation setup. A retractable position sensitive MCP detector is used to identify and separate the ground state (*g.s.*) and isomer(s) (*m*) in space by adjusting the reduced cyclotron phase accumulation time. Adjustable slits can then be set to isolate the separated ion species. Lastly, the MCP detector can be retracted and the separated pulsed beam can be delivered to downstream experimental endpoints.

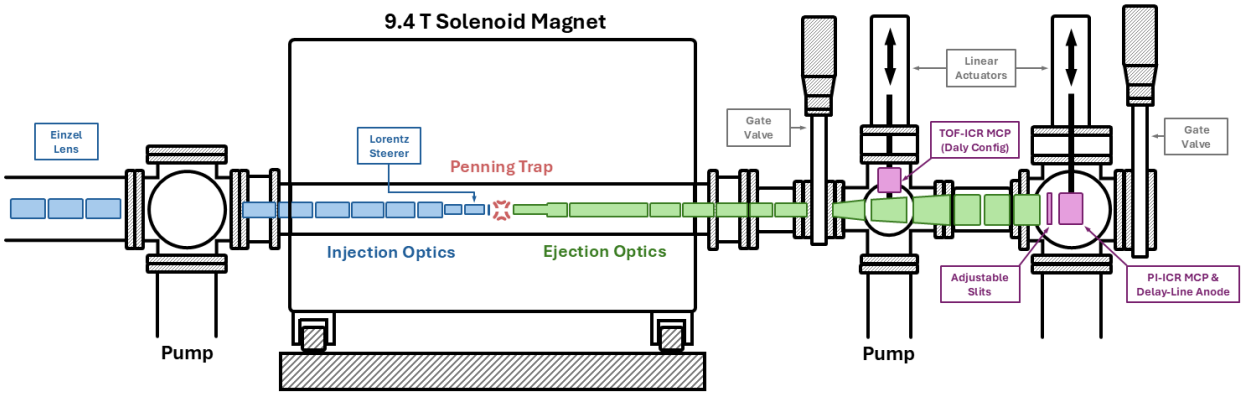

Figure 7.4 Illustration of a possible beamline extension for the upgraded PI-ICR setup with isomer separation and delivery components. Dimensions not necessarily to scale.

of the purified state to a downstream experiment. Figure 7.3 shows an illustration of the detection setup, and Fig. 7.4 shows a proposed beamline expansion to accommodate the new configuration.

SIMION simulations for an expanded beamline simulation have been conducted to study the impact on PI-ICR spot quality. In particular, optimal potentials for each drift tube element were found to optimally magnify the ion motion while maintaining maximal radial separation between the

unexcited (contaminant) ions at trap center from the excited ions. Optimal performance follows two general rules: (1) faster time-of-flights to the MCP, and (2) smoothly varying potential gradients. The drift tube elements are designed to gradually increase in radius to accommodate the radial magnification of the ions. Three drift tube elements at the end of the beamline can be configured as an Einzel lens to maintain an appropriate radius before the MCP detector if needed.

CHAPTER 8

CONCLUSIONS AND PERSPECTIVES

The Low Energy Beam and Ion Trap (LEBIT) facility has well utilized the advances to rare isotope research with the recently commissioned Facility for Rare Isotope Beams (FRIB). As FRIB continues to ramp up operations to push further from stability, LEBIT is well poised to provide critical mass information for many nuclei of high scientific interest. However, despite the incredible advances of FRIB, many of these isotopes will remain challenging to access due to low production rate. With the recent implementation of the Phase Imaging Ion Cyclotron Resonance (PI-ICR) mass measurement technique at LEBIT, many of these challenging measurements are now well within reach.

Extensive work was taken to streamline the PI-ICR measurement procedure and characterize the systematics of the technique over the past five years. As a result, LEBIT has completed numerous rare isotope measurements. In particular, the PI-ICR technique was demonstrated to provide superior mass precision with a fraction of the detected ions compared to the standard Time-of-Flight Ion Cyclotron Resonance (TOF-ICR) previously in use at LEBIT. The enhanced capabilities of PI-ICR has also enabled LEBIT to develop new methods to further reduce the detected ion threshold and push towards isotopes significantly further from stability. Custom data acquisition and analysis codes were also developed to provide quick feedback during an experiment allowing for effective tuning, delivery, and purification of the beam delivered to LEBIT.

The first precision mass measurement of the proton-rich proton-halo candidate ^{22}Al was performed as the commissioning run of the PI-ICR technique at LEBIT. The exceptionally small proton separation energy that resulted from the observed mass supported the case for a proton halo. However, both a 'universal *sd*-shell (USD)' model and a 'particle-plus-rotor' model suggested inadequate conditions for a ground state halo to exist ^{22}Al while replicating the observed proton separation energy. Since the time of publishing, many additional theoretical studies investigating ^{22}Al were conducted and spanned a wide range of model approaches. Ultimately, the case for a ground state halo was ruled out, except in the case of sufficient deformation according to sev-

eral models. Recent measurements of the ground state spin-parity and charge radius for ^{22}Al has conclusively determined that a proton halo does not exist in the ground state.

Lastly, there are a number of planned upgrades for PI-ICR at LEBIT to further enhance the capabilities of the mass measurement program. A larger detector with improved position sensitivity will soon be installed. To accommodate the new detector, an expanded beamline is being designed. Additionally, LEBIT is designing a novel approach to provide purified beams of the lowest isomeric states for downstream experiments. The concept was demonstrated with the SuN++ total absorption gamma ray spectrometer and the two isomeric states in ^{70}Cu. The planned upgrades to the beamline are expected to dramatically improve both the rate and resolution of the purified beam for future collaborations.

BIBLIOGRAPHY

[1] European Commission, "Living guidelines on the responsible use of generative ai in research." https://research-and-innovation.ec.europa.eu/document/2b6cf7e5-36ac-41cb-aab5-0d32050143dc_en. Second Edition, April 2025.

[2] J. Lilley, *Nuclear physics: principles and applications*. John Wiley & Sons, 2013.

[3] R. Casten, *Nuclear structure from a simple perspective*, vol. 23. Oxford university press, 2000.

[4] W. D. Myers and W. J. Swiatecki, "Nuclear masses and deformations," *Nuclear Physics*, vol. 81, no. 1, pp. 1–60, 1966.

[5] T. Yamaguchi, H. Koura, Y. Litvinov, and M. Wang, "Masses of exotic nuclei," *Progress in Particle and Nuclear Physics*, vol. 120, p. 103882, 2021.

[6] D. Lunney, J. M. Pearson, and C. Thibault, "Recent trends in the determination of nuclear masses," *Rev. Mod. Phys.*, vol. 75, pp. 1021–1082, Aug 2003.

[7] J. Erler, N. Birge, M. Kortelainen, W. Nazarewicz, E. Olsen, A. M. Perhac, and M. Stoitsov, "The limits of the nuclear landscape," *Nature*, vol. 486, no. 7404, pp. 509–512, 2012.

[8] P. Hansen, "Nuclear structure at the drip lines," *Nuclear Physics A*, vol. 553, pp. 89–106, 1993.

[9] T. Baumann, A. Spyrou, and M. Thoennessen, "Nuclear structure experiments along the neutron drip line," *Reports on Progress in Physics*, vol. 75, no. 3, p. 036301, 2012.

[10] M. Stoitsov, J. Dobaczewski, W. Nazarewicz, S. Pittel, and D. Dean, "Systematic study of deformed nuclei at the drip lines and beyond," *Physical Review C*, vol. 68, no. 5, p. 054312, 2003.

[11] N. Schunck and J. Egido, "Nuclear halos and drip lines in symmetry-conserving continuum hartree-fock-bogoliubov theory," *Physical Review C*, vol. 78, no. 6, p. 064305, 2008.

[12] M. Matsuo and T. Nakatsukasa, "Open problems in nuclear structure near drip lines," *Journal of Physics G: Nuclear and Particle Physics*, vol. 37, no. 6, p. 064017, 2010.

[13] T. Otsuka, A. Gade, O. Sorlin, T. Suzuki, and Y. Utsuno, "Evolution of shell structure in exotic nuclei," *Reviews of modern physics*, vol. 92, no. 1, p. 015002, 2020.

[14] B. Blank and M. Borge, "Nuclear structure at the proton drip line: Advances with nuclear decay studies," *Progress in Particle and Nuclear Physics*, vol. 60, no. 2, pp. 403–483, 2008.

[15] M. Pfützner and C. Mazzocchi, "Nuclei near and at the proton dripline," in *Handbook of Nuclear Physics*, pp. 1–41, Springer, 2022.

[16] D. Vretenar, "Nuclear structure far from stability," *Nuclear Physics A*, vol. 751, pp. 264–281, 2005.

[17] M. Pfützner, M. Karny, L. Grigorenko, and K. Riisager, "Radioactive decays at limits of nuclear stability," *Reviews of modern physics*, vol. 84, no. 2, pp. 567–619, 2012.

[18] Y. Ye, X. Yang, H. Sakurai, and B. Hu, "Physics of exotic nuclei," *Nature Reviews Physics*, vol. 7, no. 1, pp. 21–37, 2025.

[19] I. Tanihata, H. Savajols, and R. Kanungo, "Recent experimental progress in nuclear halo structure studies," *Progress in Particle and Nuclear Physics*, vol. 68, pp. 215–313, 2013.

[20] H.-W. Hammer, S. König, and U. Van Kolck, "Nuclear effective field theory: status and perspectives," *Reviews of Modern Physics*, vol. 92, no. 2, p. 025004, 2020.

[21] I. Tanihata and B. Jonson, *Halo Nuclei*, pp. 985–1026. Singapore: Springer Nature Singapore, 2023.

[22] W. H. King, *Isotope shifts in atomic spectra*. Springer Science & Business Media, 2013.

[23] A. Einstein, "Does the inertia of a body depend upon its energy-content," *Annalen der physik*, vol. 18, no. 13, pp. 639–641, 1905.

[24] F. Heiße, F. Köhler-Langes, S. Rau, J. Hou, S. Junck, A. Kracke, A. Mooser, W. Quint, S. Ulmer, G. Werth, K. Blaum, and S. Sturm, "High-precision measurement of the proton's atomic mass," *Phys. Rev. Lett.*, vol. 119, p. 033001, Jul 2017.

[25] P. J. Mohr, E. Tiesinga, D. B. Newell, and B. N. Taylor, "Codata internationally reconmmended 2022 values of the fundamental physical constants," 2024-05-08 16:05:01 2024.

[26] M. Wang, W. J. Huang, F. G. Kondev, G. Audi, and S. Naimi, "The ame 2020 atomic mass evaluation (ii). tables, graphs and references," *Chinese Physics C*, vol. 45, no. 3, p. 030003, 2021.

[27] G. Audi, "The history of nuclidic masses and of their evaluation," *International Journal of Mass Spectrometry*, vol. 251, no. 2-3, pp. 85–94, 2006.

[28] M. A. Famiano, "Nuclear mass measurements with radioactive ion beams," *International Journal of Modern Physics E*, vol. 28, no. 04, p. 1930005, 2019.

[29] M. Matoš, A. Estradé, H. Schatz, D. Bazin, M. Famiano, A. Gade, S. George, W. Lynch, Z. Meisel, M. Portillo, *et al.*, "Time-of-flight mass measurements of exotic nuclei," *Nuclear Instruments and Methods in Physics Research Section A: Accelerators, Spectrometers, Detectors and Associated Equipment*, vol. 696, pp. 171–179, 2012.

[30] D. Bazin, J. Caggiano, B. Sherrill, J. Yurkon, and A. Zeller, "The s800 spectrograph," *Nuclear Instruments and Methods in Physics Research Section B: Beam Interactions with Materials and Atoms*, vol. 204, pp. 629–633, 2003.

[31] L. Bianchi, B. Fernandez, J. Gastebois, A. Gillibert, W. Mittig, and J. Barrette, "Speg: An energy loss spectrometer for ganil," *Nuclear Instruments and Methods in Physics Research Section A: Accelerators, Spectrometers, Detectors and Associated Equipment*, vol. 276, no. 3, pp. 509–520, 1989.

[32] B. Franzke, "The heavy ion storage and cooler ring project esr at gsi," *Nuclear Instruments and Methods in Physics Research Section B: Beam Interactions with Materials and Atoms*, vol. 24-25, pp. 18–25, 1987.

[33] J. Xia, W. Zhan, B. Wei, Y. Yuan, M. Song, W. Zhang, X. Yang, P. Yuan, D. Gao, H. Zhao, X. Yang, G. Xiao, K. Man, J. Dang, X. Cai, Y. Wang, J. Tang, W. Qiao, Y. Rao, Y. He, L. Mao, and Z. Zhou, "The heavy ion cooler-storage-ring project (hirfl-csr) at lanzhou," *Nuclear Instruments and Methods in Physics Research Section A: Accelerators, Spectrometers, Detectors and Associated Equipment*, vol. 488, no. 1, pp. 11–25, 2002.

[34] M.-Z. Sun, Y. Yu, X. Wang, M. Wang, J. Li, Y.-H. Zhang, K. Blaum, Z. Chen, R.-J. Chen, H.-Y. Deng, *et al.*, "Ground-state mass of ^{22}Al and test of state-of-the-art ab initio calculations," *Chinese Physics C*, 2024.

[35] A. Verenchikov, V. Makarov, A. Vorobyev, and S. Kirillov, "A perspective of multi-reflecting tof ms," *Mass Spectrometry Reviews*, 2024.

[36] W. R. Plaß, T. Dickel, and C. Scheidenberger, "Multiple-reflection time-of-flight mass spectrometry," *International Journal of Mass Spectrometry*, vol. 349, pp. 134–144, 2013.

[37] F. Maier, F. Buchinger, L. Croquette, P. Fischer, H. Heylen, F. Hummer, C. Kanitz, A. Kwiatkowski, V. Lagaki, S. Lechner, *et al.*, "Increased beam energy as a pathway towards a highly selective and high-flux mr-tof mass separator," *Nuclear Instruments and Methods in Physics Research Section A: Accelerators, Spectrometers, Detectors and Associated Equipment*, vol. 1056, p. 168545, 2023.

[38] T. Dickel, W. Plaß, A. Becker, U. Czok, H. Geissel, E. Haettner, C. Jesch, W. Kinsel, M. Petrick, C. Scheidenberger, *et al.*, "A high-performance multiple-reflection time-of-flight mass spectrometer and isobar separator for the research with exotic nuclei," *Nuclear Instruments and Methods in Physics Research Section A: Accelerators, Spectrometers, Detectors and Associated Equipment*, vol. 777, pp. 172–188, 2015.

[39] R. Wolf, F. Wienholtz, D. Atanasov, D. Beck, K. Blaum, C. Borgmann, F. Herfurth, M. Kowalska, S. Kreim, Y. A. Litvinov, *et al.*, "Isoltrap's multi-reflection time-of-flight mass separator/spectrometer," *International Journal of Mass Spectrometry*, vol. 349, pp. 123–133, 2013.

[40] P. Schury, T. Niwase, M. Wada, P. Brionnet, S. Chen, T. Hashimoto, H. Haba, Y. Hirayama, D. Hou, S. Iimura, *et al.*, "First high-precision direct determination of the atomic mass of a superheavy nuclide," *Physical Review C*, vol. 104, no. 2, p. L021304, 2021.

[41] M. Mougeot, D. Atanasov, J. Karthein, R. Wolf, P. Ascher, K. Blaum, K. Chrysalidis, G. Hagen, J. Holt, W. Huang, *et al.*, "Mass measurements of $^{99-101}$In challenge ab initio nuclear theory of the nuclide ^{100}Sn," *Nature Physics*, vol. 17, no. 10, pp. 1099–1103, 2021.

[42] G. Bollen, R. B. Moore, G. Savard, and H. Stolenzberg, "The accuracy of heavy-ion mass measurements using time of flight-ion cyclotron resonance in a penning trap," *J. Appl. Phys.*, vol. 68:4355, 1990.

[43] K. Kromer, C. Lyu, M. Door, P. Filianin, Z. Harman, J. Herkenhoff, W. Huang, C. H. Keitel, D. Lange, Y. N. Novikov, *et al.*, "High-precision mass measurement of doubly magic ^{208}Pb," *The European Physical Journal A*, vol. 58, no. 10, p. 202, 2022.

[44] O. Bezrodnova, S. Sasidharan, W. Quint, S. Sturm, and K. Blaum, "Penning-trap mass measurement of ^{3}He," *Physical Review A*, vol. 111, no. 4, p. L040801, 2025.

[45] S. Campbell, G. Bollen, B. Brown, A. Dockery, C. Ireland, K. Minamisono, D. Puentes, B. Rickey, R. Ringle, I. Yandow, *et al.*, "Precision mass measurement of the proton dripline halo candidate ^{22}Al," *Physical Review Letters*, vol. 132, no. 15, p. 152501, 2024.

[46] M. Smith, M. Brodeur, T. Brunner, S. Ettenauer, A. Lapierre, R. Ringle, V. Ryjkov, F. Ames, P. Bricault, G. Drake, *et al.*, "First penning-trap mass measurement of the exotic halo nucleus ^{11}Li," *Physical Review Letters*, vol. 101, no. 20, p. 202501, 2008.

[47] M. Mukherjee, D. Beck, K. Blaum, G. Bollen, J. Dilling, S. George, F. Herfurth, A. Herlert, A. Kellerbauer, H. J. Kluge, *et al.*, "Isoltrap: An on-line penning trap for mass spectrometry on short-lived nuclides," *The European Physical Journal A*, vol. 35, pp. 1–29, 2008.

[48] T. Eronen, V. Kolhinen, V.-V. Elomaa, D. Gorelov, U. Hager, J. Hakala, A. Jokinen, A. Kankainen, P. Karvonen, S. Kopecky, *et al.*, "Jyfltrap: a penning trap for precision mass spectroscopy and isobaric purification," *Three decades of research using IGISOL technique at the University of Jyväskylä: A Portrait of the Ion Guide Isotope Separator On-Line Facility in Jyväskylä*, pp. 61–81, 2014.

[49] J. Dilling, D. Ackermann, J. Bernard, F. Hessberger, S. Hofmann, W. Hornung, H. Kluge, E. Lamour, M. Maier, R. Mann, *et al.*, "The shiptrap project: A capture and storage facility at gsi for heavy radionuclides from ship," *Hyperfine Interactions*, vol. 127, pp. 491–496, 2000.

[50] G. Savard, J. Wang, K. Sharma, H. Sharma, J. Clark, C. Boudreau, F. Buchinger, J. Crawford, J. Greene, S. Gulick, *et al.*, "Studies of neutron-rich isotopes with the cpt mass spectrometer and the caribu project," *International Journal of Mass Spectrometry*, vol. 251, no. 2-3, pp. 252–259, 2006.

[51] A. A. Kwiatkowski, J. Dilling, S. Malbrunot-Ettenauer, and M. P. Reiter, "15 years of precision mass measurements at titan," *The European Physical Journal A*, vol. 60, no. 4, p. 87, 2024.

[52] R. Ringle, G. Bollen, A. Prinke, J. Savory, P. Schury, S. Schwarz, and T. Sun, "The lebit 9.4 t penning trap mass spectrometer," *Nuclear Instruments and Methods in Physics Research Section A: Accelerators, Spectrometers, Detectors and Associated Equipment*, vol. 604, no. 3, pp. 536–547, 2009.

[53] A. Valverde, G. Bollen, M. Brodeur, R. Bryce, K. Cooper, M. Eibach, K. Gulyuz, C. Izzo, D. Morrissey, M. Redshaw, *et al.*, "First direct determination of the superallowed β-decay qec value for ^{14}O," *Physical Review Letters*, vol. 114, no. 23, p. 232502, 2015.

[54] A. Valverde, M. Brodeur, G. Bollen, M. Eibach, K. Gulyuz, A. Hamaker, C. Izzo, W.-J. Ong, D. Puentes, M. Redshaw, *et al.*, "High-precision mass measurement of ^{56}Cu and the redirection of the rp-process flow," *Physical Review Letters*, vol. 120, no. 3, p. 032701, 2018.

[55] F. Maier, G. Bollen, B. Brown, S. Campbell, X. Chen, H. Erington, N. Gamage, C. Ireland, R. Ringle, S. Schwarz, *et al.*, "Exploring isospin symmetry breaking in exotic nuclei: High-precision mass measurement of ^{23}Si and shell-model calculations of $t = 5/2$ nuclei," *Physical Review C*, vol. 112, no. 1, p. 014329, 2025.

[56] F. Maier, C. Ireland, G. Bollen, E. Dhayal, T. Fowler-Davis, E. Leistenschneider, M. Reiter, R. Ringle, S. Schwarz, and A. Sjaarda, "A high-voltage mr-tof mass spectrometer and separator for the study of exotic isotopes at frib," *Nuclear Instruments and Methods in Physics Research Section A: Accelerators, Spectrometers, Detectors and Associated Equipment*, vol. 1084, p. 171220, 2026.

[57] A. Marshall, C. Hendrickson, and G. Jackson, "Fourier transform ion cyclotron resonance mass spectrometry: a primer," *Mass Spectrom. Rev.*, vol. 17, Jan-Feb 1998.

[58] A. Hamaker, G. Bollen, M. Eibach, C. Izzo, D. Puentes, M. Redshaw, R. Ringle, R. Sandler, S. Schwarz, and I. Yandow, "Sipt - an ultrasensitive mass spectrometer for rare isotopes," *Hyperfine Interactions*, vol. 240, p. 34, apr 2019.

[59] S. E. Campbell, G. Bollen, A. Hamaker, W. Kretzer, R. Ringle, and S. Schwarz, "Applications of machine learning and neural networks for ft-icr mass measurements with sipt," *Atoms*, vol. 11, no. 10, p. 126, 2023.

[60] S. Eliseev, K. Blaum, M. Block, A. Dörr, C. Droese, T. Eronen, M. Goncharov, M. Höcker, J. Ketter, E. M. Ramirez, *et al.*, "A phase-imaging technique for cyclotron-frequency measurements," *Applied Physics B*, vol. 114, pp. 107–128, 2014.

[61] I. T. Yandow, *Mass Measurement of ^{27}P to Improve Type-I X-Ray Burst Models and Implementation of Phase Imaging Ion Cyclotron Resonance Mass Measurement Technique*. PhD thesis, Michigan State University, 2023.

[62] C. M. I. *et al.*, "Mass of ^{101}Sn and bayesian extrapolations to the proton drip line," *Phys. Rev. C*, vol. 113, p. L021302, Feb 2026.

[63] L. S. Brown and G. Gabrielse, "Geonium theory: Physics of a single electron or ion in a penning trap," *Reviews of Modern Physics*, vol. 58, no. 1, p. 233, 1986.

[64] L. S. Brown and G. Gabrielse, "Precision spectroscopy of a charged particle in an imperfect penning trap," *Physical Review A*, vol. 25, no. 4, p. 2423, 1982.

[65] G. Gabrielse, L. Haarsma, and S. Rolston, "Open-endcap penning traps for high precision experiments," *International Journal of Mass Spectrometry and Ion Processes*, vol. 88, no. 2-3, pp. 319–332, 1989.

[66] G. Gabrielse, "Why is sideband mass spectrometry possible with ions in a penning trap?," *Physical Review Letters*, vol. 102, no. 17, p. 172501, 2009.

[67] D. Nesterenko, T. Eronen, Z. Ge, A. Kankainen, and M. Vilen, "Study of radial motion phase advance during motion excitations in a penning trap and accuracy of jyfltrap mass spectrometer," *The European Physical Journal A*, vol. 57, no. 11, p. 302, 2021.

[68] M. König, G. Bollen, H.-J. Kluge, T. Otto, and J. Szerypo, "Quadrupole excitation of stored ion motion at the true cyclotron frequency," *International Journal of Mass Spectrometry and Ion Processes*, vol. 142, no. 1-2, pp. 95–116, 1995.

[69] K. Blaum, D. Beck, G. Bollen, P. Delahaye, C. Guénaut, F. Herfurth, A. Kellerbauer, H.-J. Kluge, D. Lunney, S. Schwarz, *et al.*, "Population inversion of nuclear states by a penning trap mass spectrometer," *Europhysics Letters*, vol. 67, no. 4, p. 586, 2004.

[70] A. A. Kwiatkowski, G. Bollen, M. Redshaw, R. Ringle, and S. Schwarz, "Isobaric beam purification for high precision penning trap mass spectrometry of radioactive isotope beams with swift," *International Journal of Mass Spectrometry*, vol. 379, pp. 9–15, 2015.

[71] G. Savard, S. Becker, G. Bollen, H.-J. Kluge, R. Moore, T. Otto, L. Schweikhard, H. Stolzenberg, and U. Wiess, "A new cooling technique for heavy ions in a penning trap," *Physics Letters A*, vol. 158, no. 5, pp. 247–252, 1991.

[72] S. Eliseev, K. Blaum, M. Block, C. Droese, M. Goncharov, E. M. Ramirez, D. Nesterenko, Y. N. Novikov, and L. Schweikhard, "Phase-imaging ion-cyclotron-resonance measurements for short-lived nuclides," *Physical Review Letters*, vol. 110, no. 8, p. 082501, 2013.

[73] C.-W. Ma, H.-L. Wei, X.-Q. Liu, J. Su, H. Zheng, W.-P. Lin, and Y.-X. Zhang, "Nuclear fragments in projectile fragmentation reactions," *Progress in Particle and Nuclear Physics*, vol. 121, p. 103911, 2021.

[74] M. Hausmann, A. Aaron, A. Amthor, M. Avilov, L. Bandura, R. Bennett, G. Bollen, T. Borden, T. Burgess, S. Chouhan, *et al.*, "Design of the advanced rare isotope separator aris at frib," *Nuclear Instruments and Methods in Physics Research Section B: Beam Interactions with Materials and Atoms*, vol. 317, pp. 349–353, 2013.

[75] C. Sumithrarachchi, D. Morrissey, S. Schwarz, K. Lund, G. Bollen, R. Ringle, G. Savard, and A. Villari, "Beam thermalization in a large gas catcher," *Nuclear Instruments and Methods in Physics Research Section B: Beam Interactions with Materials and Atoms*, vol. 463, pp. 305–309, 2020.

[76] K. Lund, G. Bollen, D. Lawton, D. Morrissey, J. Ottarson, R. Ringle, S. Schwarz, C. Sumithrarachchi, A. Villari, and J. Yurkon, "Online tests of the advanced cryogenic gas stopper at nscl," *Nuclear Instruments and Methods in Physics Research Section B: Beam Interactions with Materials and Atoms*, vol. 463, pp. 378–381, 2020.

[77] C. Izzo, G. Bollen, S. Bustabad, M. Eibach, K. Gulyuz, D. Morrissey, M. Redshaw, R. Ringle, R. Sandler, S. Schwarz, *et al.*, "A laser ablation source for offline ion production at lebit," *Nuclear Instruments and Methods in Physics Research Section B: Beam Interactions with Materials and Atoms*, vol. 376, pp. 60–63, 2016.

[78] S. Schwarz, G. Bollen, R. Ringle, J. Savory, and P. Schury, "The lebit ion cooler and buncher," *Nuclear Instruments and Methods in Physics Research Section A: Accelerators, Spectrometers, Detectors and Associated Equipment*, vol. 816, pp. 131–141, 2016.

[79] R. Ringle, G. Bollen, A. Prinke, J. Savory, P. Schury, S. Schwarz, and T. Sun, "A 'lorentz' steerer for ion injection into a penning trap," *International Journal of Mass Spectrometry*, vol. 263, no. 1, pp. 38–44, 2007.

[80] N. Daly, "Scintillation type mass spectrometer ion detector," *Review of Scientific Instruments*, vol. 31, no. 3, pp. 264–267, 1960.

[81] A. S. Hamaker, *Mass Measurement of the Lightweight Self-Conjugate Nucleus Zirconium-80 and the Development of the Single Ion Penning Trap*. Michigan State University, 2021.

[82] G. Savard, G. Bollen, H.-J. Kluge, R. Moore, T. Otto, L. Schweikhard, H. Stolzenberg, U. Wiess, *et al.*, "A new cooling technique for heavy ions in a penning trap," *Physics Letters A*, vol. 158, no. 5, pp. 247–252, 1991.

[83] O. Jagutzki, V. Mergel, K. Ullmann-Pfleger, L. Spielberger, U. Spillmann, R. Dörner, and H. Schmidt-Böcking, "A broad-application microchannel-plate detector system for advanced particle or photon detection tasks: large area imaging, precise multi-hit timing information and high detection rate," *Nuclear Instruments and Methods in Physics Research Section A: Accelerators, Spectrometers, Detectors and Associated Equipment*, vol. 477, no. 1-3, pp. 244–249, 2002.

[84] R. Orford, *Precision mass measurements of neutron-rich rare isotopes approaching the r-process path with the Canadian Penning Trap mass spectrometer*. McGill University (Canada), 2014.

[85] J. Karthein, D. Atanasov, K. Blaum, D. Lunney, V. Manea, and M. Mougeot, "Analysis methods and code for very high-precision mass measurements of unstable isotopes," *Computer Physics Communications*, vol. 267, p. 108070, 2021.

[86] O. Jagutzki, A. Cerezo, A. Czasch, R. Dorner, M. Hattas, M. Huang, V. Mergel, U. Spillmann, K. Ullmann-Pfleger, T. Weber, *et al.*, "Multiple hit readout of a microchannel plate detector with a three-layer delay-line anode," *IEEE Transactions on Nuclear Science*, vol. 49, no. 5, pp. 2477–2483, 2002.

[87] D. Freedman and P. Diaconis, "On the histogram as a density estimator: L 2 theory," *Zeitschrift für Wahrscheinlichkeitstheorie und verwandte Gebiete*, vol. 57, no. 4, pp. 453–476, 1981.

[88] A. K. Jain, M. N. Murty, and P. J. Flynn, "Data clustering: a review," *ACM computing surveys (CSUR)*, vol. 31, no. 3, pp. 264–323, 1999.

[89] D. Xu and Y. Tian, "A comprehensive survey of clustering algorithms," *Annals of data science*, vol. 2, no. 2, pp. 165–193, 2015.

[90] A. Likas, N. Vlassis, and J. J. Verbeek, "The global k-means clustering algorithm," *Pattern recognition*, vol. 36, no. 2, pp. 451–461, 2003.

[91] M. Ester, H.-P. Kriegel, J. Sander, X. Xu, *et al.*, "A density-based algorithm for discovering clusters in large spatial databases with noise," in *kdd*, vol. 96, pp. 226–231, 1996.

[92] M. Ankerst, M. M. Breunig, H.-P. Kriegel, and J. Sander, "Optics: Ordering points to identify the clustering structure," *ACM Sigmod record*, vol. 28, no. 2, pp. 49–60, 1999.

[93] A. Kataria and M. Singh, "A review of data classification using k-nearest neighbour algorithm," *International Journal of Emerging Technology and Advanced Engineering*, vol. 3, no. 6, pp. 354–360, 2013.

[94] I. Wickramasinghe and H. Kalutarage, "Naive bayes: applications, variations and vulnerabilities: a review of literature with code snippets for implementation," *Soft Computing*, vol. 25, no. 3, pp. 2277–2293, 2021.

[95] M. Abadi, A. Agarwal, P. Barham, E. Brevdo, Z. Chen, C. Citro, G. S. Corrado, A. Davis, J. Dean, M. Devin, S. Ghemawat, I. Goodfellow, A. Harp, G. Irving, M. Isard, Y. Jia, R. Jozefowicz, L. Kaiser, M. Kudlur, J. Levenberg, D. Mané, R. Monga, S. Moore, D. Murray, C. Olah, M. Schuster, J. Shlens, B. Steiner, I. Sutskever, K. Talwar, P. Tucker, V. Vanhoucke, V. Vasudevan, F. Viégas, O. Vinyals, P. Warden, M. Wattenberg, M. Wicke, Y. Yu, and X. Zheng, "TensorFlow: Large-scale machine learning on heterogeneous systems," 2015. Software available from tensorflow.org.

[96] F. Chollet *et al.*, "Keras." `https://keras.io`, 2015.

[97] D. Kingma and J. Ba, "Adam: A method for stochastic optimization," *International Conference on Learning Representations*, 12 2014.

[98] K. Gulyuz, J. Ariche, G. Bollen, S. Bustabad, M. Eibach, C. Izzo, S. Novario, M. Redshaw, R. Ringle, R. Sandler, *et al.*, "Determination of the direct double-β-decay q value of ^{96}Zr and atomic masses of $^{90-92,94,96}$Zr and $^{92,94-98,100}$Mo," *Physical Review C*, vol. 91, no. 5, p. 055501, 2015.

[99] R. Ringle, T. Sun, G. Bollen, D. Davies, M. Facina, J. Huikari, E. Kwan, D. Morrissey, A. Prinke, J. Savory, *et al.*, "High-precision penning trap mass measurements of ^{37,38}Ca and their contributions to conserved vector current and isobaric mass multiplet equation," *Physical Review C*, vol. 75, no. 5, p. 055503, 2007.

[100] R. Orford, J. Clark, G. Savard, A. Aprahamian, F. Buchinger, M. Burkey, D. Gorelov, J. Klimes, G. Morgan, A. Nystrom, *et al.*, "Improving the measurement sensitivity of the canadian penning trap mass spectrometer through pi-icr," *Nuclear Instruments and Methods in Physics Research Section B: Beam Interactions with Materials and Atoms*, vol. 463, pp. 491–495, 2020.

[101] D. Nesterenko, T. Eronen, Z. Ge, A. Kankainen, and M. Vilen, "Study of radial motion phase advance during motion excitations in a penning trap and accuracy of jyfltrap mass spectrometer," *The European Physical Journal A*, vol. 57, no. 11, p. 302, 2021.

[102] D. Ray, A. Valverde, M. Brodeur, F. Buchinger, J. Clark, B. Liu, G. Morgan, R. Orford, W. Porter, G. Savard, *et al.*, "Phase-imaging ion-cyclotron-resonance mass spectrometry with the canadian penning trap at caribu," *Nuclear Instruments and Methods in Physics Research Section A: Accelerators, Spectrometers, Detectors and Associated Equipment*, vol. 1076, p. 170433, 2025.

[103] S. Chenmarev, S. Nagy, J. van de Laar, K. Blaum, M. Block, and C. E. Düllmann, "First application of the phase-imaging ion-cyclotron resonance technique at triga-trap," *The European Physical Journal A*, vol. 59, no. 2, p. 29, 2023.

[104] J. Ketter, T. Eronen, M. Höcker, S. Streubel, and K. Blaum, "First-order perturbative calculation of the frequency-shifts caused by static cylindrically-symmetric electric and magnetic imperfections of a penning trap," *International Journal of Mass Spectrometry*, vol. 358, pp. 1–16, 2014.

[105] R. Ringle, *High-precision mass measurement of ^{38}Ca and development of the LEBIT 9.4-T Penning trap system*. PhD thesis, Michigan State University, 2006.

[106] M. Brodeur, V. Ryjkov, T. Brunner, S. Ettenauer, A. Gallant, V. Simon, M. Smith, A. Lapierre, R. Ringle, P. Delheij, *et al.*, "Verifying the accuracy of the titan penning-trap mass spectrometer," *International journal of mass spectrometry*, vol. 310, pp. 20–31, 2012.

[107] D. Beck, K. Blaum, G. Bollen, P. Delahaye, S. George, C. Guénaut, F. Herfurth, A. Herlert, D. Lunney, L. Schweikhard, *et al.*, "Electric and magnetic field optimization procedure for penning trap mass spectrometers," *Nuclear Instruments and Methods in Physics Research Section A: Accelerators, Spectrometers, Detectors and Associated Equipment*, vol. 598, no. 2, pp. 635–641, 2009.

[108] C. Baker, W. Bertsche, A. Capra, C. Cesar, M. Charlton, A. Christensen, R. Collister, A. Cridland Mathad, S. Eriksson, A. Evans, *et al.*, "Measurements of penning-malmberg trap patch potentials and associated performance degradation," *Physical Review Research*, vol. 6, no. 1, p. L012008, 2024.

[109] F. Heiße, S. Rau, F. Köhler-Langes, W. Quint, G. Werth, S. Sturm, and K. Blaum, "High-precision mass spectrometer for light ions," *Physical Review A*, vol. 100, no. 2, p. 022518, 2019.

[110] D. Wineland and H. Dehmelt, "Principles of the stored ion calorimeter," *Journal of Applied Physics*, vol. 46, no. 2, pp. 919–930, 1975.

[111] T. Porobić, M. Beck, M. Breitenfeldt, C. Couratin, P. Finlay, A. Knecht, X. Fabian, P. Friedag, X. Fléchard, E. Liénard, *et al.*, "Space-charge effects in penning ion traps," *Nuclear Instruments and Methods in Physics Research Section A: Accelerators, Spectrometers, Detectors and Associated Equipment*, vol. 785, pp. 153–162, 2015.

[112] W. R. Plaß, T. Dickel, U. Czok, H. Geissel, M. Petrick, K. Reinheimer, C. Scheidenberger, and M. I. Yavor, "Isobar separation by time-of-flight mass spectrometry for low-energy radioactive ion beam facilities," *Nuclear Instruments and Methods in Physics Research*

Section B: Beam Interactions with Materials and Atoms, vol. 266, no. 19-20, pp. 4560–4564, 2008.

[113] K. Kaneko, Y. Sun, T. Mizusaki, S. Tazaki, and S. Ghorui, "Isospin-symmetry breaking in superallowed fermi β-decay due to isospin-nonconserving forces," *Physics Letters B*, vol. 773, pp. 521–526, 2017.

[114] J. Lee, X. Xu, K. Kaneko, Y. Sun, C. Lin, L. Sun, P. Liang, Z. Li, J. Li, H. Wu, *et al.*, "Large isospin asymmetry in ^{22}Si/^{22}O mirror gamow-teller transitions reveals the halo structure of ^{22}Al," *Physical Review Letters*, vol. 125, no. 19, p. 192503, 2020.

[115] R. Ringle, S. Schwarz, and G. Bollen, "Penning trap mass spectrometry of rare isotopes produced via projectile fragmentation at the lebit facility," *International Journal of Mass Spectrometry*, vol. 349, pp. 87–93, 2013.

[116] C. Wu, H. Wu, J. Li, D. Luo, Z. Li, H. Hua, X. Xu, C. Lin, J. Lee, L. Sun, *et al.*, "β-decay spectroscopy of the proton drip-line nucleus ^{22}Al," *Physical Review C*, vol. 104, no. 4, p. 044311, 2021.

[117] G. Bollen, H.-J. Kluge, M. König, T. Otto, G. Savard, H. Stolzenberg, R. Moore, G. Rouleau, G. Audi, I. Collaboration, *et al.*, "Resolution of nuclear ground and isomeric states by a penning trap mass spectrometer," *Physical Review C*, vol. 46, no. 6, p. R2140, 1992.

[118] B. Wildenthal, "Empirical strengths of spin operators in nuclei," *Progress in particle and nuclear physics*, vol. 11, pp. 5–51, 1984.

[119] R. Machleidt, "The meson theory of nuclear forces and nuclear structure," in *Advances in nuclear physics*, pp. 189–376, Springer, 1989.

[120] A. Magilligan and B. Brown, "New isospin-breaking 'usd' hamiltonians for the *sd* shell," *Physical Review C*, vol. 101, no. 6, p. 064312, 2020.

[121] S. Stroberg, A. Calci, H. Hergert, J. Holt, S. Bogner, R. Roth, and A. Schwenk, "Nucleus-dependent valence-space approach to nuclear structure," *Physical Review Letters*, vol. 118, no. 3, p. 032502, 2017.

[122] S. R. Stroberg, H. Hergert, S. K. Bogner, and J. D. Holt, "Nonempirical interactions for the nuclear shell model: an update," *Annual Review of Nuclear and Particle Science*, vol. 69, pp. 307–362, 2019.

[123] B. Blank, F. Boué, S. Andriamonje, S. Czajkowski, R. Del Moral, J. Dufour, A. Fleury, P. Pourre, M. Pravikoff, N. Orr, *et al.*, "The spectroscopy of ^{22}Al: a βp, β2p and $\beta\alpha$ emitter," *Nuclear Physics A*, vol. 615, no. 1, pp. 52–68, 1997.

[124] S. Czajkowski, S. Andriamonje, B. Blank, F. Boué, R. Del Moral, J. Dufour, A. Fleury, E. Hanelt, N. Orr, P. Pourre, *et al.*, "β-p,-2p,-alpha spectroscopy of ^{22,23,24}Si and ^{22}Al," *Nuclear Physics A*, vol. 616, no. 1-2, pp. 278–285, 1997.

[125] K. Fossez, W. Nazarewicz, Y. Jaganathen, N. Michel, and M. Płoszajczak, "Nuclear rotation in the continuum," *Phys. Rev. C*, vol. 93, p. 011305(R), 2016.

[126] R. Panda, M. Panigrahi, M. K. Sharma, and S. Patra, "Evidence of a proton halo in ^{23}Al: A mean field analysis," *Physics of Atomic Nuclei*, vol. 81, pp. 417–428, 2018.

[127] P. Möller, A. J. Sierk, T. Ichikawa, and H. Sagawa, "Nuclear ground-state masses and deformations: Frdm (2012)," *Atomic Data and Nuclear Data Tables*, vol. 109, pp. 1–204, 2016.

[128] L. Shen, M. Xie, Q. Yuan, and J. Li, "Disentangling proton-halo signatures in al 22 via mirror-symmetry breaking: An ab initio study," *Physical Review C*, vol. 113, no. 3, p. 034306, 2026.

[129] Z. C. Xu, H. Y. Shang, S. M. Wang, and Y. G. Ma, "Structure evolution of ground and excited states in the exotic nucleus ^{22}Al," *Phys. Rev. C*, vol. 113, p. L031301, Mar 2026.

[130] K. Zhang, C. Pan, and S. Wang, "Examination of the evidence for a proton halo in ^{22}Al," *Physical Review C*, vol. 110, no. 1, p. 014320, 2024.

[131] P. Papakonstantinou, M. Mun, C. Pan, and K. Zhang, "Proton halo structures and ^{22}Al," *Physical Review C*, vol. 112, no. 4, p. 044301, 2025.

[132] Y.-X. Liu, H.-T. Xue, Q. B. Chen, X.-R. Zhou, and H.-J. Schulze, "Proton-halo phenomenon of ^{22}Al and $^{23}_{\Lambda}$Al based on the deformed skyrme-hartree-fock method," *Phys. Rev. C*, vol. 113, p. 034319, Mar 2026.

[133] E. A. M. Jensen, J. S. Nielsen, B. S. O. Johansson, A. Adams, J. Dopfer, C. S. Sumithrarachchi, L. J. Sun, L. E. Weghorn, T. Wheeler, C. Wrede, M. J. G. Borge, O. Tengblad, M. Madurga, B. Jonson, K. Riisager, and H. O. U. Fynbo, "Measurement of the ground state spin and parity of ^{22}Al disfavors halo formation," *Phys. Rev. Lett.*, vol. 136, p. 202503, May 2026.

[134] B. J. Rickey, *Investigating the Possible Halo Structure in ^{22}Al and ^{23}Al*. PhD thesis, Michigan State University, 2025.

[135] J. Van Roosbroeck, C. Guénaut, G. Audi, D. Beck, K. Blaum, G. Bollen, J. Cederkall, P. Delahaye, A. De Maesschalck, H. De Witte, *et al.*, "Unambiguous identification of three β-decaying isomers in ^{70}Cu," *Physical Review Letters*, vol. 92, no. 11, p. 112501, 2004.

[136] E. Ronning, S. Uthayakumaar, A. Spyrou, A. Richard, S. Liddick, A. Tsantiri, R. Ringle, H. Arora, H. Berg, J. Berkman, *et al.*, "The upgraded summing nai (tl)(sun++) absorption spectrometer," *Nuclear Instruments and Methods in Physics Research Section A: Accelerators, Spectrometers, Detectors and Associated Equipment*, p. 170930, 2025.